The development of an ionospheric storm-time index for the South African region

A thesis submitted in fulfillment of the
requirements for the degree of

DOCTOR OF PHILOSOPHY

of

Rhodes University

by

Mpho Tshisaphungo (08T6610)

December 2020

Abstract

This thesis presents the development of a regional ionospheric storm-time model which forms the foundation of an index to provide a quick view of the ionospheric storm effects over South African mid-latitude region. The model is based on the $foF2$ measurements from four South African ionosonde stations. The data coverage for the model development over Grahamstown $(33.3°S, 26.5°E)$, Hermanus $(34.42°S, 19.22°E)$, Louisvale $(28.50°S, 21.20°E)$, and Madimbo $(22.39°S, 30.88°E)$ is 1996-2016, 2009-2016, 2000-2016, and 2000-2016 respectively. Data from the Global Positioning System (GPS) and radio occultation (RO) technique were used during validation. As the measure of either positive or negative storm effect, the variation of the critical frequency of the F2 layer $(foF2)$ from the monthly median values (denoted as $\Delta foF2$) is modeled. The modeling of $\Delta foF2$ is based on only storm time data with the criteria of Dst $\leqslant$ -50 nT and Kp $\geqslant$ 4. The modeling methods used in the study were artificial neural network (ANN), linear regression (LR) and polynomial functions. The approach taken was to first test the modeling techniques on a single station before expanding the study to cover the regional aspect. The single station modeling was developed based on ionosonde data over Grahamstown.

The inputs for the model which related to seasonal variation, diurnal variation, geomagnetic activity and solar activity were considered. For the geomagnetic activity, three indices namely; the symmetric disturbance in the horizontal component of the Earth's magnetic field $(SYM - H)$, the Auroral Electrojet (AE) index and local geomagnetic index A, were included as inputs. The performance of a single station model revealed that, of the three geomagnetic indices, $SYM - H$ index has the largest contribution of 41% and 54% based on ANN and LR techniques respectively. The average correlation coefficients (R) for both ANN and LR models was 0.8, when validated during the selected storms falling within the period of model development. When validated using storms that fall outside the period of model development, the model gave R values of 0.6 and 0.5 for ANN and LR respectively.

In addition, the GPS total electron content (TEC) derived measurements were used to estimate $foF2$ data. This is because there are more GPS receivers than ionosonde locations and the utilisation of this data increases the spatial coverage of the regional model. The estimation of $foF2$ from GPS TEC was done at GPS-ionosonde co-locations using polynomial functions. The average R values of 0.69 and 0.65 were obtained between actual and derived $\Delta foF2$ over the co-locations and other GPS stations respectively. Validation of GPS TEC derived $foF2$ with RO data over regions out of ionospheric pierce points coverage with respect to ionosonde locations gave R greater than 0.9 for the selected storm period of 4-8 August 2011. The regional storm-time model was then developed based on the ANN technique using the four South African ionosonde stations. The maximum and minimum R values of 0.6 and 0.5 were obtained over ionosonde and GPS locations respectively. This model forms the basis towards the regional ionospheric storm-time index.

Publication from this thesis

The relevant section for this publication is in chapter 4 of the thesis.

1. Tshisaphungo, M., Habarulema, J. B., and McKinnell, L. A. (2018). Modeling ionospheric foF2 response during geomagnetic storms using neural network and linear regression techniques. Advances in Space Research, 61(12), 2891-2903. `https://doi.org/10.1016/j.asr.2018.03.025`

Acknowledgement

Contents

List of Tables

List of Figures

Chapter 1

Introduction

The ionosphere is an important region of the Earth's upper atmosphere with regards to radio wave propagation and radio communications in general. This region has a large concentration of free ions and electrons mainly formed by solar X-rays and extreme ultraviolet (EUV) radiation and can affect radio wave propagation (Rishbeth and Garriott, 1969; Hargreaves, 1979, 1992). It is well known to be an ionized medium that supports strong electric currents (Hargreaves, 1992). The ionospheric properties govern the way in which radio communications, particularly in the high frequency (HF) band, take place. Although today, satellites are widely used, HF radio communications using the ionosphere still play a major role in providing worldwide radio coverage (Davies, 1990; Tooley and Wyatt, 2017; Cander, 2019). During periods of high solar activity an interaction between coronal mass ejections and the Earth's magnetic field can result in large geomagnetic disturbances. Such disturbances can lead to substantial perturbation of the ionosphere such that there are huge fluctuations of electron density in the ionosphere. The ionospheric responses to these geomagnetic disturbances at different latitudes have been extensively studied (e.g. Prölss *et al.*, 1991; Prölss, 1993a,b, 1995; Mannucci *et al.*, 2005; Tsurutani *et al.*, 2004, 2005, 2006, 2008b; Vijaya Lekshmi *et al.*, 2011; Habarulema *et al.*, 2013, 2017; Matamba *et al.*, 2015, 2016). The ionospheric perturbations have significant impact on technological systems such as satellite navigation applications, surveillance, communication etc. (Davies, 1990; McNamara, 1991). For practical applications, ionospheric modeling is an important part of "space weather" research in the field of space physics and it's accuracy especially during disturbed geomagnetic conditions is crucial.

Space weather refers to conditions on the Sun and in the solar wind, magnetosphere, ionosphere, and thermosphere that can influence the performance and reliability of space-borne and ground-based technological systems and can endanger human health (Schwenn, 2006; Pulkkinen, 2007; Moldwin, 2008). Space weather is influenced by phenomena such as solar flares, coronal mass ejections, corotating interaction regions (CIRs), coronal hole high speed stream (CH HSS), solar energetic particles which originate from the Sun's activity. These phenomena are known as space weather events. It is important to understand these events because they can cause

significant disruptions on radio communications, satellite navigation and power grids (Moldwin, 2008; Schrijver *et al.*, 2015). The large perturbations in the ionosphere are mainly as a result of these space weather events (e.g. Tsurutani *et al.*, 2005; Jakowski *et al.*, 2005; Gopalswamy *et al.*, 2005a; Maruyama and Nakamura, 2007). This thesis focuses on the modeling of the ionospheric $foF2$ response to geomagnetic storm activity over the South African region. A database of $foF2$ measurements during geomagnetic storm occurrences (Dst $\leqslant$ -50 nT & Kp $\leqslant$ 4) has been created for model development. Different techniques/models for the reconstruction of the $foF2$ response to geomagnetic storm activity were investigated for a single station (Grahamstown, $33.3^o S, 26.5^o E$) and then expanded to a regional scale. The measurements of $foF2$ from four ionosonde locations (Grahamstown, Hermanus, Louisvale, Madimbo) to achieve regional coverage were used along with Total Electron Content (TEC) measurements from Global Navigation Satellite System (GNSS) receiver stations such as, for example, dual frequency Global Positioning System (GPS) receivers. In this study, the neural network and linear regression techniques were used for model development. The performance of these models were presented and compared with other existing models such as the International Reference Ionosphere (IRI) which is a standard empirical model of the ionosphere (Rawer *et al.*, 1978; Bilitza *et al.*, 1990). The modeling undertaken in this thesis will lead to a regional development of an ionospheric storm-time index.

Studies have been conducted with regard to the development of ionospheric activity indices (e.g. Turner, 1968; Belehaki *et al.*, 2000; Ortikov *et al.*, 2003; Gulyaeva and Stanislawska, 2008; Jakowski *et al.*, 2006, 2012). Jakowski *et al.* (2012) developed a disturbance ionospheric index (DIX) which gives a measure of ionospheric disturbance during a period of adverse space weather. It is important for practical applications such as precise positioning and navigation by different GNSS techniques. This index (DIX) was developed for the European mid-latitude region using GNSS TEC data. Another study was done by Gulyaeva and Stanislawska (2008) who developed the planetary ionospheric storm index, Wp, crucial for identifying ionospheric storms occurring under magnetically quiet time conditions. This index is deduced from numerical global ionospheric GPS-IONospheric map EXchange (GPS-IONEX) maps of the vertical total electron content (VTEC). Another study regarding ionospheric index was conducted by Turner (1968) and dealt with the development of a global ionospheric T index derived from critical frequency of the F2 layer ($foF2$) values. Its speciality lies within characterizing the radio wave propagation through the ionosphere. However, none of these indices are best suited for the South African region mainly because they were developed specifically for other regions. For global indices, the representation of regional ionospheric changes is not well defined because of data sparsity in the model development especially over the African region.

In South Africa there exists a space weather centre which provides operational services such as forecasting and warning of ionospheric conditions to HF communication users. This study will

contribute to the application of space weather services in an operational environment within the region. The ionospheric storm index is important because it provides an immediate and practical form of support to users of radio communications systems affected by the ionosphere (Stamper *et al.*, 2004; Jakowski *et al.*, 2012). Short-term forecasting of the ionospheric response during storm conditions is important for reliable performance of advanced technological systems.

1.1   Project motivation and objectives

Space weather is a threat to various operating systems such as high frequency (HF) propagation, navigation, survey as well as satellite communications on a daily basis. Most of these systems are highly affected by ionospheric variability. A number of studies concerning ionospheric response to geomagnetic storms over the South African region have been well documented (e.g. Habarulema *et al.*, 2010, 2013, 2017; Ngwira *et al.*, 2012; Amabayo *et al.*, 2012; Matamba *et al.*, 2015). During geomagnetic storms, different processes and changes of the electron density lead to large variability in the ionosphere. The electron density can either increase or decrease with respect to the quiet ionosphere during disturbed conditions and such changes are denoted as a positive or negative ionospheric storm (Prölss, 1993a,b; Pietrella and Perrone, 2008). In the operational environment, a quick evaluation and measure of the complex ionospheric propagation conditions is of utmost essential to the users (Stankov *et al.*, 2002; Jakowski *et al.*, 2006, 2012), hence the need for the development of an ionospheric index. Due to the localized ionospheric changes (Prölss, 1993b), the need for regional models of the ionospheric response during geomagnetic storms remains vital.

The aim of this study is to develop an ionospheric storm-time index suitable for the South African region based on ionosonde $foF2$ measurements. The main objectives of this research included:

i) Create storm-time $foF2$ database with ionosonde and GNSS measurements using a criteria of Dst $\leqslant$ -50 nT & Kp $\leqslant$ 4.

ii) Develop mathematical expressions to estimate $foF2$ from GNSS TEC for periods of geomagnetic storm occurrences.

iii) Develop a single station modeling of ionospheric $foF2$ response during geomagnetic storms.

v) Build on objective (iii) to progress towards the development of a regional ionospheric storm-time index based on ionosonde measured and GPS derived $foF2$ data.

1.2   Outline of the thesis

This thesis consists of seven chapters. The introduction to ionospheric modeling for radio wave propagation application is discussed in Chapter 1. The importance of regional modeling especially during geomagnetic storm time is also presented together with project motivation and objectives. Chapter 2 provides review background of the ionosphere, geomagnetic and ionospheric storms as well as storm-time modeling of the ionosphere. The data sources and modeling techniques used in the study are then described in Chapter 3. Chapter 4 covers the single station modeling of ionospheric $foF2$ response to geomagnetic storms using neural network and linear regression techniques. For the purpose of spatial data coverage over the region, data from four ionosonde stations were supplemented by 36 GNSS receiver stations. This was done by establishing an expression to estimate $foF2$ from GNSS TEC measurements and is presented in Chapter 5. In Chapter 6, a development of the regional ionospheric storm-time index model is presented and the results of the model's performance are discussed. Finally, Chapter 7 outlines the main conclusions, identifies limitations and suggestions for improvement and recommendations for further research.

Chapter 2

Background Theory

This chapter presents the background information regarding the structure and basic formation of the ionosphere. Description of the ionospheric variability as well as different ionospheric layers is provided. An overview of geomagnetic and ionospheric storms driven by different mechanisms and also the importance of ionospheric modeling are also presented.

2.1 Introduction to the ionosphere

The ionosphere is a region of the upper Earth's atmosphere where a number of electrically charged particles known as ions and electrons are present in large quantities (Rishbeth and Garriott, 1969; Davies, 1990; McNamara, 1991). The ionosphere exists mainly because of the interaction of the solar extreme ultraviolet (EUV) and X-ray radiations with the neutral atmosphere. The rate of ionization in the ionosphere varies significantly with the amount of radiation received from the Sun. The study of ionosphere dates back to 1926 when the term "ionosphere" was first introduced by Watson-Watt (Rishbeth and Garriott, 1969). In 1925, Appleton confirmed the existence of the ionosphere by receiving echoes from continuous radio wave signals (Appleton, 1932). Since then, ionospheric studies have been extensively documented and the role of the ionosphere as an ionized layer for radio wave propagation application remains an important area of research (e.g. Rishbeth and Garriott, 1969; Davies, 1990; McNamara, 1991). The ionospheric dynamics and variability could be significantly enhanced during severe space weather storms and it is coupled with other systems such as the solar wind and the magnetosphere, hence the need for continuous improvements on ionospheric modeling and a better understanding of the physical drivers. The ionosphere forms part of the mesosphere, thermosphere and exosphere as illustrated in Figure 2.1. The ionosphere has three main regions known as the D, E, and F layers which are discussed in detail in section 2.1.2.
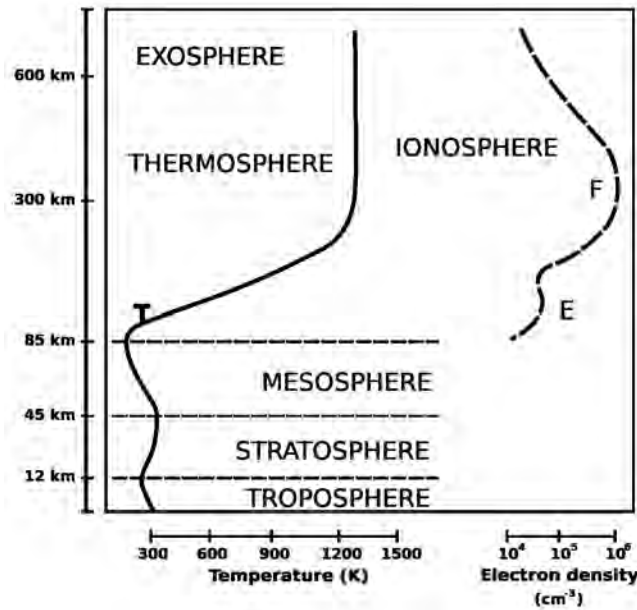
Figure 2.1: A schematic representation of the ionosphere as part of Earth's atmospheric region. Source:Bhamer (2007)

As electromagnetic waves (radio signals) travel, they interact with objects and the medium (ionosphere) in which they propagate. During propagation, these radio signals can either be reflected, refracted or diffracted. These interactions cause radio signals to change direction, and to reach areas which would not be possible if the radio signals traveled in a direct line. The ionosphere is a particularly important region with regards to radio signal propagation and radio communications in general. Its properties govern the way in which radio communications, particularly in the high frequency (HF) radio communication bands take place. While the ions give the ionosphere its name due to large concentrations of free ions and electrons, it is the free electrons that affect the radio waves and radio communication. In particular the ionosphere is widely known for affecting signals within the short wave radio bands where it reflects signals enabling these radio communication signals to be heard over great distances. Radio stations use the properties of the ionosphere to enable them to provide worldwide radio communications coverage (McNamara, 1991). Although today, satellites are widely used, HF radio communications using the ionosphere still play a major role in providing worldwide radio coverage.

2.1.1   Formation of the ionosphere

The charged particles within the ionosphere are created when the Sun's EUV light strips off electrons from the neutral atoms of the Earth's atmosphere. When EUV photons hit neutral atoms such as oxygen, some electrons can move freely, causing neutral atoms to become positively charged ions. This process is known as photoionization (McNamara, 1991) and is

illustrated in Equation 2.1 below:

$$O \underset{Atom}{} \longrightarrow O^+ \underset{ION}{} + e^- \underset{Electron}{} \tag{2.1}$$
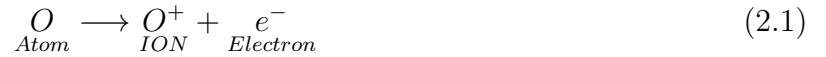
where O is the oxygen neutral atom, O^+ is the positively charged oxygen ion, and e^- is the free electron. The free electrons within the ionosphere are the ones responsible for reflecting radio waves because they are lighter than positive ions, hence the quick response to rapid oscillations of the radio wave (McNamara, 1991). During the day there are more ions and electrons created than destroyed due to the presence of EUV light from the Sun. At night, a process called recombination (a reverse of photoionization) occurs within the ionosphere where negatively charged electrons and positively charged ions combine again to produce neutral atoms. In the lower level of the ionosphere (D region) electrons are lost in a way that they attach themselves to neutral atoms to form negatively charged ions during a process known as attachment (McNamara, 1991). There are two types of recombination: radiative and dissociative recombination. Radiative recombination is when electrons interact directly with positively charged ions concurrently forming neutral atoms and radiating energy (McNamara, 1991) as shown in Equation 2.2.

$$O^+ + e^- \longrightarrow O + Radiative\ energy \tag{2.2}$$

Two stage processes occur during dissociative recombination. In the first stage, positive ions interact with several neutral molecules, replacing one of the atoms in the molecule:

$$O^+ + N_2 \longrightarrow NO^+ + N \tag{2.3}$$

The second stage process occurs when electrons combine with a positively charged molecule to produce two neutral atoms,

$$NO^+ + e^- \longrightarrow N + O \tag{2.4}$$

An important aspect to note about recombination and attachment is that they can occur anytime of the day and at all levels of the ionosphere. Contrary, photoionization happens only during the day when the Sun is above the horizon (McNamara, 1991). The electron density is greater during midday when photoionization is at its highest. The ionospheric plasma is considered a cold weakly ionized gas composed of electrons (lighter species) and positive ions (heavy species) in equal number (McNamara, 1991).

2.1.2 Ionospheric regions

The ionosphere is composed of distinct layers that are identified by the layers D, E, and F. The F layer is further divided into two separate layers during the day time known as the F1 and

F2 layers. In early radio probing of the ionosphere, the experimental proof of the existence of the Kennelly-Heaviside layer now known as the E layer was provided (Appleton, 1932). The symbol E was used to describe the electric field of the wave reflected from the first layer of the ionosphere. The experimental results also indicated a height of 90 - 100 km for the Kennelly-Heaviside (E) layer (Appleton, 1932). Later a second layer at higher altitude known as the F layer was found to be more intensely ionized than the E layer. Suspecting a layer at lower altitude, the additional symbol D was adopted. It is now known that electron density increases with altitude from the D layer, reaching a maximum in the F2 layer. Though the nomenclature used to describe the different layers of the ionosphere continues in wide use, the definitions have evolved to reflect the improved understanding of the underlying physics at different altitudes.

The D layer is the lowest region of the ionosphere at an altitude of ~ 50 to ~ 90 km. The section from 50 to 70 km is sometimes referred to as the C layer which is produced mainly by cosmic rays (Rishbeth and Garriott, 1969). There is a high recombination rate in the D layer which suggests less ionized layer that disappears during night time (Rishbeth and Garriott, 1969; Davies, 1990; McNamara, 1991; Zolesi and Cander, 2014). The typical value of the maximum electron density in the D layer at noon is about 1.5 x 10^{10} electrons per cubic meter (el/m^3) in the mid-latitude region. Solar X-rays ionize all the gases present within the ionosphere to some extent. The X-rays concerned in this layer are the high energy portion of the solar spectrum, penetrating below the E layer. During the day some reflection can be obtained from the D layer, but the strength of radio waves is reduced. This layer is responsible for absorption of radio wave signals. At its upper boundary the D layer merges with the E layer.

The E layer of the ionosphere lies within an altitude of 90 km to about 160 km. Ionization in the E layer is mainly caused by soft X-rays and EUV solar radiation of molecular oxygen. The E layer is weakly ionized and contains electrons with an average E layer electron density of $\sim 10^{11}$ el/m^3 at around ~ 110 km. After sunset, the levels of ionization drops, and ions and electrons recombine very rapidly causing the E layer to disappear completely during the night time. An anomaly of the E region is the sporadic-E layer. Sporadic-E refers to the anomalous values of ionization within the E region at constant height, whose critical frequency is higher than usual for the E layer (Hargreaves, 1992; Pignalberi *et al.*, 2014).

The F layer is the uppermost part of the ionosphere and is divided into F1 and F2 layers during day time. The altitude range of the F1 layer is about 150 to 200 km. This layer is observed only during the day and is more prominent during summer (than winter), and ionosphere storms (Davies, 1990). The F2 layer has the greatest concentration of free electrons. During the day, the F2 layer reaches the peak at an altitude of ~ 300 km. The maximum electron densities within the F1 and F2 layers at noon are respectively 2.5 x 10^{11} m^3 and 10^{12} m^3 within the

mid-latitude region. At night the F1 and F2 layers merge to become one layer. Due to the continuous presence of the F2 layer, it is considered to be the most important layer for HF communication (Davies, 1990; McNamara, 1991). This layer reflects radio waves with frequencies up to 35 megahertz (MHz) and the exact value depends on the peak electron concentration within the region.

The ionospheric structure is complex at any particular location because it is dependent on the intensity of the Sun's EUV light which is not constant at all wavelengths (McNamara, 1991). The relationship between electron density and frequency is given by Equation 2.5 below:

$$f_c = 9 \times 10^{-6} N_m^{1/2} \tag{2.5}$$

where f_c is the critical frequency of a specific layer in the ionosphere and N_m is the maximum electron density in that layer. The critical frequency for each layer is represented by foE, $foF1$, and $foF2$ in the respective layers E, F1, and F2 (McNamara, 1991) and each layer has a corresponding maximum electron density: NmE, $NmF1$, and $NmF2$.

2.1.3   Ionospheric variations

The ionosphere experiences both short and long term variations. Because the formation of the ionosphere is directly related to EUV radiations from the Sun, this describes some of the factors that govern regular ionospheric variability such as time of day, season, solar cycle, and position on the surface of the Earth (McNamara, 1991). There are also irregular variations in the ionosphere which can occur at anytime with little to no warning of manifestation. They are caused mainly by solar flares, radiation storms as well as geomagnetic storms, which in turn result from disturbances on the Sun.

2.1.3.1   Diurnal variation

The diurnal variation within the ionosphere refers to the 24-hour variations of the electron density as a result of the solar zenith angle. The maximum electron density is expected during local midday when the solar zenith angle is zero. This means that the Sun is overhead and maximum photoionization rate is reached. Figure 2.2 represents, as an example, the diurnal variability of $foF2$ averaged over a month of October 2016 for four South African ionosonde stations: Grahamstown $(33.32°S, 26.51°E)$, Hermanus $(34.42°S, 19.22°E)$, Louisvale $(28.50°S, 21.20°E)$, and Madimbo $(22.39°S, 30.88°E)$ in the mid-latitude region. These four ionosonde stations are respectively denoted as GR13L, HE13N, LV12P, and MU12K. The $foF2$ values peak are around 10:00 Universal Time (UT) which is equivalent to midday, 12:00 South African local time (LT) due to the Sun being overhead, hence the maximum EUV radiation is received with

photoionization at its greatest. After sunset, recombination and attachment dominate leading to observed low values of $foF2$.
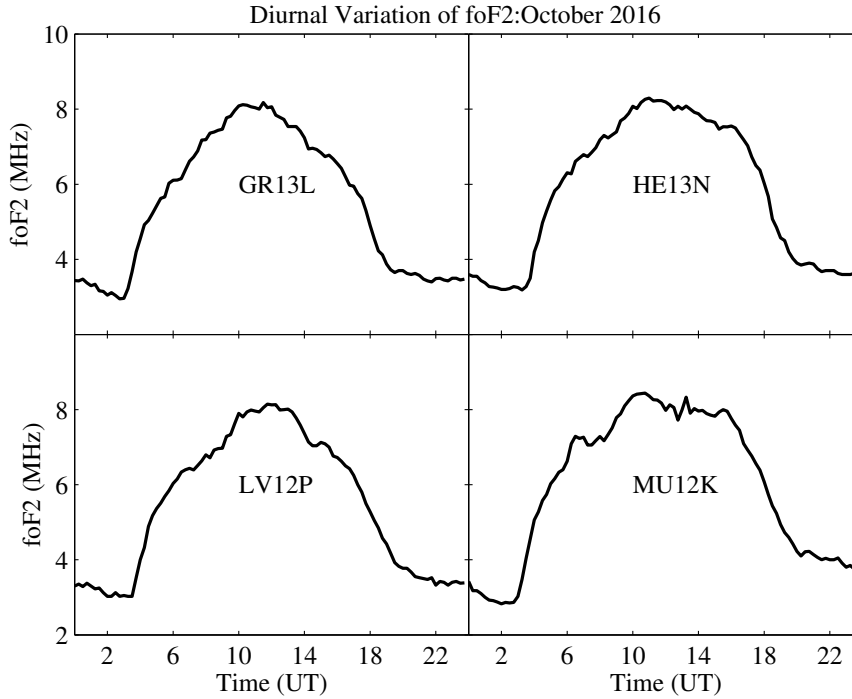
Figure 2.2: Diurnal variation of averaged $foF2$ values for the month of October 2016 over four mid-latitude South African ionosonde stations: Grahamstown (GR13L), Hermanus (HE13N), Louisvale (LV12P), and Madimbo (MU12K).

2.1.3.2   Seasonal variation

The seasonal variation of the ionosphere is also partly due to the solar zenith angle which varies throughout the year. In both northern and southern hemispheres, electron density in the ionosphere is greater in summer than in winter. This is not always the case as composition changes in the neutral atmosphere can somewhat reveal the seasonal variation (McNamara, 1991). Figure 2.3 (a) shows, as an example, the variation of $foF2$ values for the year 2011 at 10:00 UT (South African local noon time) over Grahamstown. The southern hemisphere winter and summer solstice are presented in Figure 2.3 (b) over the mid-latitude station. The $foF2$ values are clearly higher in the summer month (December) than in the winter month (June) which is depended on the noon solar zenith angle which is always greater in winter than in summer (McNamara, 1991). This is contrary to the observations made by McNamara (1991), where a mid-latitude station in Canberra was considered. The results showed that $foF2$ values were much greater during the day in winter than in summer and this is known as the mid-latitude seasonal anomaly (McNamara, 1991).
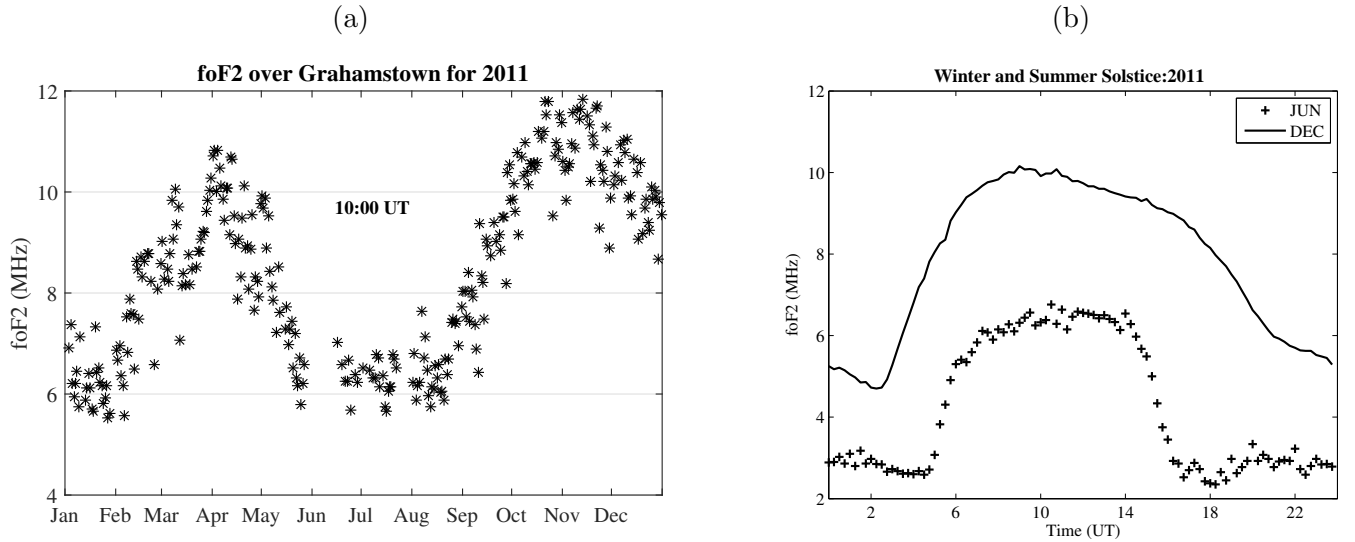
Figure 2.3: represent (a) the annual variation of $foF2$ values at 10:00 UT over a mid-latitude Grahamstown (GR13L) station during 2011 and (b) shows the hourly variation of $foF2$ for December (summer month) and June (winter month) 2011, denoted on the graph by DEC and JUN respectively.

2.1.3.3   Latitudinal variation

The ionosphere also varies with position on the Earth, especially with latitude, due to the geomagnetic field line orientation at different latitude regions. For example, the behaviour of the mid-latitude ionosphere is different to that of the low- and high-latitude ionosphere regions. The reaction rates for the mid-latitude F2 region ionosphere are sensitive to temperature and chemical composition changes. The composition change is attributed to the global circulation pattern in the thermosphere (Hargreaves, 1992). The dominant mechanism within the mid-latitude ionosphere is the global thermospheric winds (Kelley, 2009). The mid-latitude region is known as the transition region between low and high latitudes (Kelley, 2009).

There are regions (low-latitude) of high electron concentration at geomagnetic latitudes of about $\pm 20^{o}$. At the magnetic equator, the Earth's magnetic field lines are horizontal, hence solar heating and tidal oscillations in the lower ionosphere move plasma up and across the magnetic field lines. This sets up a sheet of electric current in the E region which, with the horizontal magnetic field, forces ionization up into the F layer. This phenomena is called the fountain effect or the Equatorial Ionization Anomaly (EIA) (Davies, 1990; Hargreaves, 1992). To illustrate the EIA, Figure 2.4 shows the global IONosphere Exchange (IONEX) TEC map at 12:00 UT on 21 August 2019 (geomagnetic quiet day). The IONEX data was obtained from `ftp://cddis.gsfc.nasa.gov/pub/gps/products/ionex/2019/233/`. In Figure 2.4, the minimum TEC is observed over the magnetic equator as well as two maximum TEC levels occurring at about 10° - 20° north and south of the equator due to the fountain effect described

above.
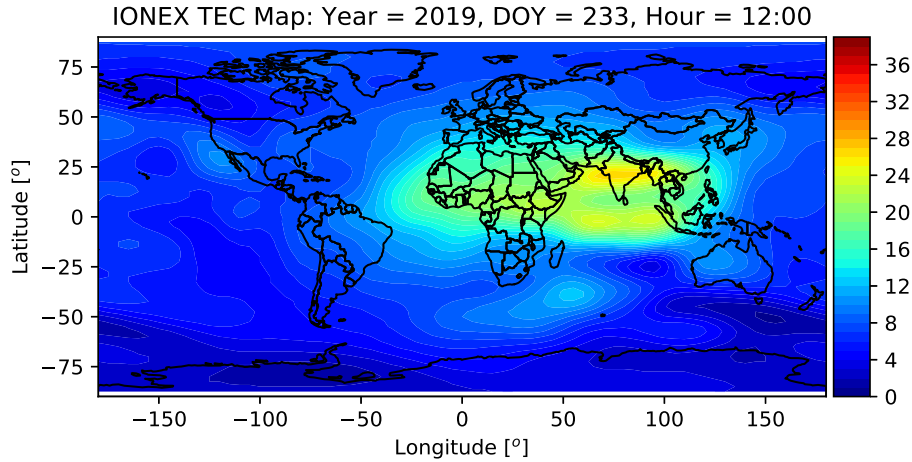
Figure 2.4: A map of global total electron content (TEC) during a quiet day of 21 August 2019 at 12:00 UT.

The disturbance to the global current system can be produced by changes in ionospheric conductivity. Occasionally, a significant increase in solar ionizing radiation especially at X-ray wavelengths, occurs during solar flares. This causes a temporary increase in the ionospheric electron density and conductivity allowing enhanced currents to flow over the dayside of the Earth (Richmond, 2017). These enhanced electric currents represent the equatorial electrojet flowing along the dip-equator (Hargreaves, 1992). The trough which is aligned with the geomagnetic dip equator exists from mid-morning to late evening, where the peak electron density (NmF2) is typically 30% less than at the crests (Rishbeth, 2000). The crests lie between 15°-20° to the north and south of equator.

The high-latitude ionosphere, where the magnetic field lines are vertically orientated, is mainly influenced by the magnetosphere and the solar wind (Hunsucker and Hargreaves, 2007). The electric field generated by the solar wind across the magnetosphere is mapped into the F region (Hargreaves, 1992). The interaction of F region plasma with magnetic field lines, tends to lift the F region towards the magnetic pole from the day side and is depleted on the night side as it drifts towards lower latitude (Hargreaves, 1992). There is more direct influence of energetic particles from the magnetosphere and the solar wind within the high latitude region than at low- and mid-latitude regions (Hunsucker and Hargreaves, 2007). The auroral zone occurs within the high latitude region and is linked to the distorted tail of the magnetosphere. The auroral phenomena includes electrojet and substorms. The other main feature of the high latitude region is the "trough". This is an area of lesser ionization which is formed between the auroral and mid-latitude ionospheres (Hunsucker and Hargreaves, 2007). One fundamental cause of the trough is the difference in circulation pattern between the inner and the outer part

of the magnetosphere (Hunsucker and Hargreaves, 2007).

2.1.3.4   Solar cycle variation

The Sun's magnetic field goes through a cycle for a period of ∼11 years (11-year solar cycle). Within the 11-year cycle, the Sun experiences high/maximum and low/minimum solar activity period which is determined by the number of sunspots observed on the Sun. Since the Sun has direct impact on the ionosphere, the long-term variation in sunspot occurrence will have an immediate effect on the electron density variation within the ionosphere.
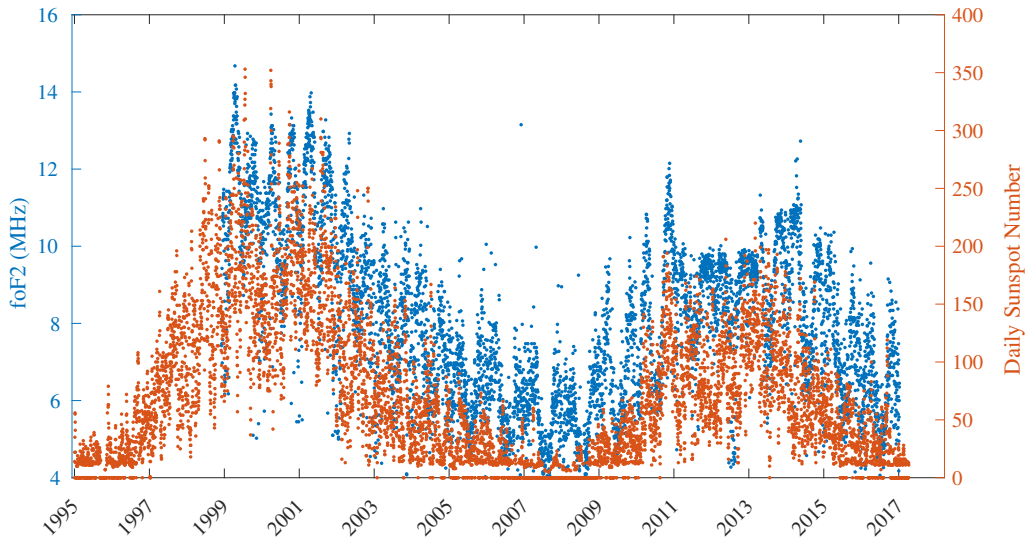
Figure 2.5: Variation of $foF2$ from 1996-2018 over Grahamstown at 10:00 UT presented on the left with daily sunspot numbers plotted on the right side.

Figure 2.5 shows that $foF2$ values are higher and lower during high and low solar activity periods respectively. During solar maximum the levels of solar radiation and the frequency of ejection of solar material such as solar flares and proton fluxes increases the ionization in the ionosphere which results in higher values of $foF2$ as compared to a solar minimum period (Davies, 1990; McNamara, 1991; Zolesi and Cander, 2014).

2.2   Geomagnetic storms

A geomagnetic storm is a temporary disturbance of the Earth's magnetosphere that occurs when there is sufficient exchange of energy from the solar wind into the space environment surrounding the Earth. Geomagnetic storms are caused by solar wind shock waves associated with solar flares, coronal mass ejections (CMEs), or coronal holes. These storms result from variations in the solar wind that produces major changes in the currents, plasmas, and fields in the Earth's magnetosphere. The solar wind conditions that are effective for creating geomagnetic storms

are sustained (for several hours) periods of high-speed solar wind, and most importantly, a southward directed solar wind magnetic field (opposite to the direction of the Earth's field) at the day side of the magnetosphere. The strong dawn-to-dusk electric fields associated with the passage of long lasting southward Earth-directed interplanetary magnetic fields (IMF) are the major causes of geomagnetic storms within the Earth's atmosphere (Gonzalez *et al.*, 1994). The electric fields are composed of two factors which are solar wind velocity and southward IMF. The primary mechanisms which are identified to be responsible for enhanced electric fields that cause geomagnetic storms are interplanetary CMEs (ICMEs) and corotating interaction regions (CIRs) (Kamide *et al.*, 1998a). The main characteristics of a geomagnetic storm is a decrease in the horizontal (H) component of the Earth's magnetic field and can be monitored by the disturbance storm time (Dst) index (Gonzalez *et al.*, 1994; Kamide *et al.*, 1998a). A geomagnetic storm has three phases known as the initial phase (onset of a period of ram pressure), the main phase which is the sustained southward interplanetary fields and the return to normal conditions called the recovery phase (Gonzalez *et al.*, 1994), which will be discussed in detail in the following subsection. The solar wind ram pressure is the pressure produced by a cloud of charged particles (e.g. CME) traveling at a certain speed with a particular density. Figure 2.6 demonstrates the three phases of a geomagnetic storm period during 6 - 10 September 2017 where a CME was the cause of this disturbance.
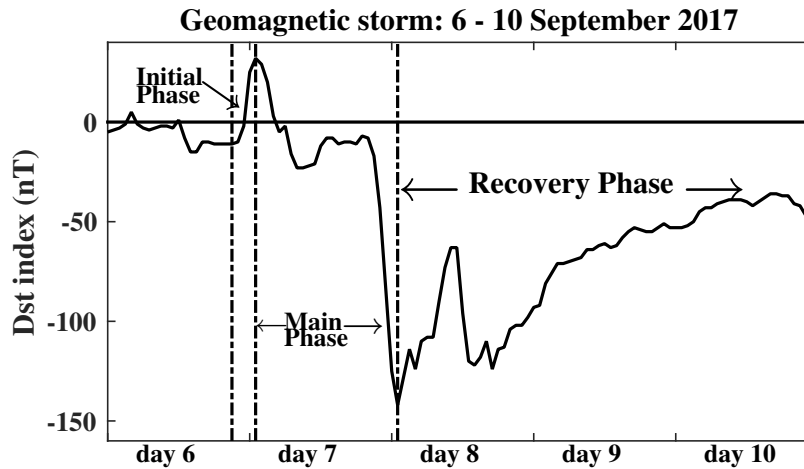
Figure 2.6: Illustration of the three phases of geomagnetic storm period; initial, main and recovery phases. The presented geomagnetic storm occurred during 6 - 10 September 2017 and was associated with a CME event.

2.2.1   Initial phase

The initial phase is also referred to as a storm sudden commencement (SSC). It is caused by the increase in plasma ram pressure associated with the increase in density and speed of the solar wind shock. This increase is accompanied by a sudden impulse (SI) within the Earth's atmospheric environment (Gonzalez *et al.*, 1999). Sudden impulses (SIs) are classified as SSC

if they are followed by a geomagnetic storm with 24 hours (Joselyn and Tsurutani, 1990). However, not all geomagnetic storms have initial phases and not all sudden increases in the Dst index are followed by a geomagnetic storm. Figure 2.6 shows the initial phase of a storm which is characterized by a sudden increase in Dst from $\sim$ -10 nT to $\sim$ 32 nT within a short period of time before declining.

2.2.2   Main phase

The main phase of a geomagnetic storm is defined by a decrease in the Dst index values or the growth of a ring current which is caused by energetic protons trapped within the geomagnetic field (Gonzalez *et al.*, 1994). The transfer of hydromagnetic-wave energy to the protons stresses the geomagnetic field and produces the storm main phase (Dessler *et al.*, 1961; Piddington, 1963; Akasofu *et al.*, 1963). The duration of the main phase is typically 2 - 8 hours or more. The storm main phase is illustrated in Figure 2.6 which started on day 7 September 2017 and lasted for $\sim$ 24 hours. During this period, there are two main storm phases observed, where the minimum Dst index for the second main storm is observed to be $\sim$ -142 nT at $\sim$ 00:00 UT on 8 September 2017.

2.2.3   Recovery phase

The recovery phase is when the Dst index starts increasing from its minimum value during a storm period. The recovery phase can last from 8 hours to several days depending on the magnitude of the storm. An example of a recovery phase is shown in Figure 2.6. In this Figure, the duration of the recovery phase lasted for $\sim$ 3 days; 8-10 September 2017.

2.2.4   Classification of geomagnetic storms

The disturbance storm time (Dst) index is widely used to indicate the levels of geomagnetic storm occurrences. The Dst index was developed to give an indication of the ring current strength (Rostoker, 1972). The Dst index is computed using four geomagnetic observatories which are: Hermanus $(34.42°S, 19.22°E)$, Honolulu $(21.32°N, 201.96°E)$, Kakioka $(36.23°N, 140.18°E)$, and San Juan $(18.01°N, 293.85°E)$. These stations were chosen based on the quality of observations, sufficiently distant from the auroral and equatorial electrojets to inhibit noise from these two sources and are distributed in longitude as evenly as possible (Sugiura and Kamei, 1991). Dst is computed using 1-hour values from the four observatories and for each hour (T), the baseline horizontal field (H_{base}) taking into account the solar quiet day variation is subtracted from the observed H value (H_{obs}) (Sugiura and Kamei, 1991):

$$\Delta H(T) = H_{obs}(T) - H_{base}(T) \tag{2.6}$$

The Dst index is normally expressed in nanotesla (nT) and is a measure of decrease in the H component of the Earth's magnetic field due to an increase in magnetospheric ring current (Gonzalez *et al.*, 1994). The Dst index is generally used to define the geomagnetic storm's occurrence time, duration and intensity. The storm criterion chosen for this work was based on Dst $\leqslant$ -50 nT.

	Dst (nT)	B_z (nT)	ΔT (hours)
Intense	-100	-10	3
Moderate	-50	-5	2
Small	-30	-3	1

(a) Storm classification by Gonzalez *et al.* (1994)

Storm class	Dst_{min} Range (nT)	Dst_{min} (nT)
weak	-30 to -50	-36
moderate	-50 to -100	-68
strong	-100 to -200	-131
severe	-200 to 350	-254
great	< -350	-427

(b) Storm classification by Loewe and Prölss (1997)

Table 2.1: Established thresholds and classification for geomagnetic storms.

The study by Gonzalez *et al.* (1994) details the thresholds of geomagnetic disturbance based on Dst index values which range between $\sim$ +100 nT to -600 nT. As presented in Table 2.1(a), the peak Dst index values for an intense storm is -100 nT, moderate storm ranges from -50 nT to -100 nT, and the weak storms are those with Dst values between -30 nT and -50 nT. Table 2.1(a) shows a general relationship of the IMF Bz and its duration of occurrence (ΔT) with Dst storm intensity. The levels of disturbance was further classified by Loewe and Prölss (1997) as shown in Table 2.1 (b).

2.3   CME- and CIR-driven storms

Geomagnetic storms are mainly driven by solar wind speed and the southward magnetic field through reconnection. In this section, the two primary interplanetary drivers: CMEs and CIRs are discussed. CME- and CIR-driven storms are well documented in the literature (e.g. Tsurutani *et al.*, 1995; Heber *et al.*, 1999; Borovsky and Denton, 2006; Denton *et al.*, 2006; Richardson *et al.*, 2006). CME is a large eruption of magnetized plasma from the Sun's outer atmosphere (corona) that propagates outward into interplanetary space. Most CMEs are associated with solar flares and some with the eruption of prominences. CIR is formed ahead of a high-speed stream emanating from a coronal hole. They are long lasting large-scale plasma structures

initiated by the interaction of a stable fast solar wind stream with the surrounding slow solar wind (Heber *et al.*, 1999; Richardson *et al.*, 2006; Richardson, 2018, and references therein). CME-driven storms generate more issues for Earth-based electrical systems while space-based assets are more vulnerable to CIR-driven storms (Borovsky and Denton, 2006). The differences between CME- and CIR-driven storm are provided in detail within Borovsky and Denton (2006).

2.3.1 CME-driven storms

CME-driven storms refer to storms induced by various components such as solar wind shock, CME sheath, ejecta, and magnetic cloud. CME-driven storms have irregular occurrence and are more frequent during solar maximum (Borovsky and Denton, 2006; Richardson *et al.*, 2006). Most SSCs are associated with strong interplanetary shocks which are normally found ahead of fast CMEs. Borovsky and Denton (2006) revealed that CME-driven storms are mostly accompanied by major solar energetic-particle (SEP) events. SEP events are enhanced fluxes of high-energy relativistic ions that can last for hours to days and are associated with solar flares and strong interplanetary shocks. Large SEP events can sometimes pose a threat to aircraft passengers and electronics (Borovsky and Denton, 2006). ICME events have greater signature in the Dst index (intense geomagnetic storm of Dst < -100 nT), hence stronger ring current is more likely during CME-driven storms (Borovsky and Denton, 2006; Denton *et al.*, 2006).

2.3.2 CIR-driven storms

CIR-driven storms are storms which are caused by either or both high-speed stream and CIR. CIRs are followed in time by high-speed streams (Borovsky and Denton, 2006). These storms are caused by the increased ram pressure associated with the high-density heliospheric current sheet (Tsurutani *et al.*, 1995). CIR-driven storms are most prevalent close to solar minimum and during the declining phase of the cycle (Tsurutani *et al.*, 1995; Denton *et al.*, 2006; Richardson *et al.*, 2006). Since CIRs are related to fast streams from coronal holes they tend to re-occur with a ∼27 day period (Tsurutani *et al.*, 1995; Denton *et al.*, 2006). Most CIR-driven storms lack SSCs and have a longer recovery phase which can last for a few days. It is known that CIR-driven storms are more effective at producing relativistic electrons in the outer radiation belts, therefore pose a more severe impact in the form of spacecraft surface charging.

2.3.3   Ionosphere response to CME- and CIR-driven storms

The large-scale perturbation in the ionosphere, also known as ionospheric storm, can be a result of CME- or CIR-driven storms. During a geomagnetic storm the enhancement in total electron content (TEC) and peak electron density may be observed on the day of SSC followed by a huge decrease on the subsequent days (Mendillo *et al.*, 1970). Ionospheric storms can be observed using ionosonde measurements as either a decrease or an increase in the ionization electron density during geomagnetic storms and are denoted respectively as negative and positive ionospheric storms (e.g. Prölss, 1995; Buonsanto, 1999; Borries *et al.*, 2015). Satellite measurements, such as those provided by Global Navigation Satellite Systems (GNSS) e.g. TEC, can also show negative or positive ionospheric storm effects (e.g. Borries *et al.*, 2015; Matamba and Habarulema, 2018). In this case, the measure of disturbance can be deduced from the deviation of daily ionospheric measurements from the respective monthly medians (or quiet-time references) using the following expression:

$$\Delta\chi = \left(\frac{\chi - \chi_m}{\chi_m}\right) \times 100 \tag{2.7}$$

where χ represents the temporal variation of $foF2$, NmF2, or TEC measurements and χ_m is the monthly median of χ values (Danilov, 2001; Matamba *et al.*, 2015). Ionospheric storms or perturbations of the ionosphere in association with the solar wind energy input into the magnetosphere have been studied in great detail (Matsushita, 1959; Mendillo *et al.*, 1970; Fuller-Rowell *et al.*, 1994; Prölss *et al.*, 1991; Prölss, 1993a,b, 1995; Buonsanto, 1999; Danilov, 2001; Borries *et al.*, 2015, and references therein).

Negative ionospheric storm effects in mid-latitude regions are mainly due to thermospheric composition changes (e.g Prölss *et al.*, 1991; Prölss, 1995; Fuller-Rowell *et al.*, 1994). Thermospheric composition changes have been suggested as the cause for the negative phase for many years (Prölss *et al.*, 1991; Prölss, 1995; Fuller-Rowell *et al.*, 1994; Tsagouri *et al.*, 2000), and this has been demonstrated clearly with satellite data (Prölss, 1997). The dissipation of the solar wind energy input generates a permanent composition disturbance zone at polar/high latitude regions (Tsagouri *et al.*, 2000). During geomagnetic storms, a large amount of energy is injected into the polar/high latitudes of the upper atmosphere which leads to the expansion of this zone towards the mid-latitudes in the post-midnight sector (Prölss, 1980, 1995; Tsagouri *et al.*, 2000). At the recovery phase of the geomagnetic storm, the composition disturbance zone is rotated to the afternoon sector following the Earth's rotation. Although the geomagnetic storm is partially recovered, the perturbations are significant enough to still produce daytime negative ionospheric storm effects at mid-latitudes (Prölss, 1995; Tsagouri *et al.*, 2000). During geomagnetic storms, there is a strong upwelling of the atmosphere around the

auroral oval caused by intense particle and joule heating process. These strong upwelling of the atmosphere transports oxygen-depleted or nitrogen-rich air from lower down in the atmosphere into the F-region (Prölss, 1980, 1995). Studies have shown that electron density of the F-region is correlated with the atomic Oxygen to molecular Nitrogen (O/N_2) ratio (e.g. Prölss, 1980; Habarulema *et al.*, 2013). Habarulema *et al.* (2013) did a comparative study of the ionospheric response during the geomagnetic storm of 7 - 12 November 2004 over the African equatorial and mid-latitude regions. There was a significant decrease in TEC with corresponding $foF2$ depletion over the mid-latitude station due to reduction in Global Ultraviolet Imager (GUVI) O/N_2 ratio as observed from the global maps.
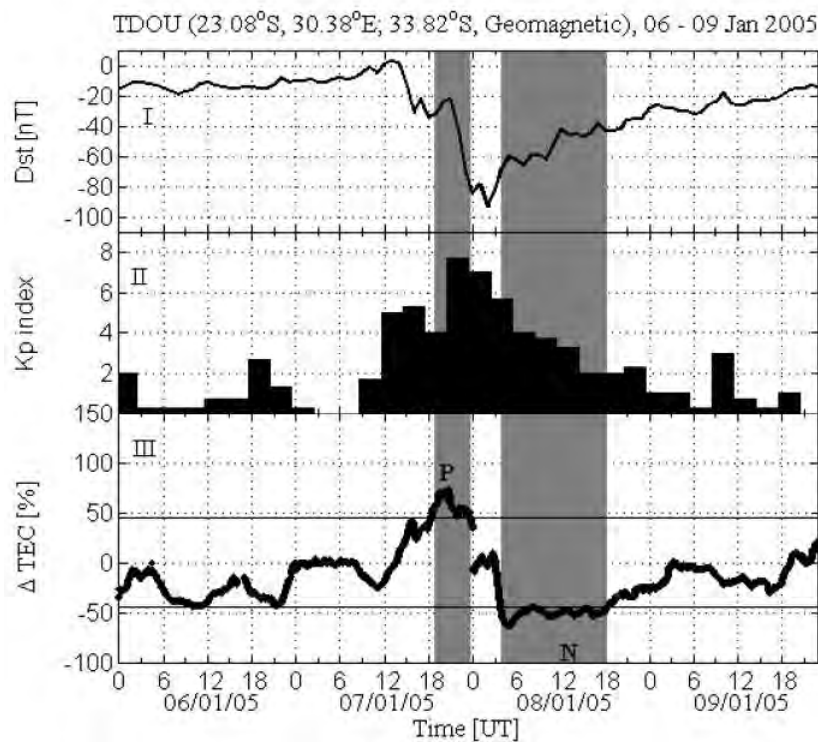
Figure 2.7: Example of positive to negative (PN) ionospheric storm effects over Thohoyandou, TDOU ($23.08°S, 30.38°E$), South Africa, southern hemisphere mid-latitude Global Positioning System (GPS) receiver station (Matamba, 2017). The storm period presented is from 6 - 9 January 2005.

Figure 2.7 is an example to illustrate the positive to negative (PN) ionospheric storm effects over the mid-latitude station,Thohoyandou, TDOU ($23.08°S, 30.38°E$), South Africa (Matamba, 2017). The variation of (I) Dst index, (II) Kp index, and (III) ΔTEC (%), which can be obtained using equation 2.7, for a storm period 6 - 9 January 2005 is presented. The P and N on the figure indicate Positive and Negative ionospheric storm effects with shaded regions showing the period when either P or N ionospheric storm effects were observed (Matamba, 2017). In Figure 2.7, the negative ionospheric storm effect is observed during the recovery phase of the geomagnetic storm.

Some of the predominant causes of positive ionospheric storm effects are traveling atmospheric disturbances (TADs), large-scale thermospheric wind circulation and electric field perturbations (Prölss *et al.*, 1991). TADs are pulse-like perturbations caused by superpositions of atmospheric gravity waves (AGWs). According to theory, such TADs are generated during substorm activities and propagate with high velocities from polar to equatorial latitudes (Prölss *et al.*, 1991; Prölss, 1993a). One of the essential features of TAD is that it carries along the equatorward-directed winds of moderate magnitude (Prölss, 1993a, 1995). At middle latitudes, these meridional winds cause an uplifting of the F2 layer, which in turn leads to an increase in electron density such that positive ionospheric storm effects are observed (Prölss *et al.*, 1991; Prölss, 1993a, 1995). It is necessary to note that this mechanism is relevant only to the daytime ionosphere (Prölss, 1995).

It has been shown that the polar energy dissipation leads to changes in the global wind circulation system (Prölss *et al.*, 1991). The intense joule heating during geomagnetic storms at polar regions lifts the neutral winds and drives them towards low and equatorial latitudes, thereby causing global thermospheric composition changes (Bagiya *et al.*, 2011). Changes in the global wind circulation are initiated by frontal systems which propagate with high velocity towards lower latitudes. This phenomenon is associated with a sudden increase in the meridional wind velocity, causing short-duration positive ionospheric storm effects (Prölss *et al.*, 1991). The large-scale wind system changes arising from these transient perturbations induce long-duration positive ionospheric storm effects (Prölss *et al.*, 1991). The atomic oxygen is lighter and therefore, lifts up first and reaches to lower latitudes earlier, also contributing to positive ionospheric storm effects (Bagiya *et al.*, 2011).

During geomagnetic storms, electric fields of solar wind origin penetrate into the magnetosphere and the dayside equatorial ionosphere. The penetration of these electric fields is very fast and they are known as prompt penetrating electric fields or PPEFs (Tsurutani *et al.*, 2008a). The daytime positive ionospheric storm effects are thought to be attributed to PPEFs (Tsurutani *et al.*, 2004, 2008a; Bagiya *et al.*, 2011). If the electric fields penetrate the ionosphere before shielding builds up, it can modify equatorial ionospheric electrodynamics. Dawn-to-dusk directed electric fields will be eastward in the daytime and westward at night (Tsurutani *et al.*, 2004). The dayside ionospheric response to the PPEF is seen as huge enhancement in electron density (Tsurutani *et al.*, 2004; Maruyama *et al.*, 2004; Bagiya *et al.*, 2011), thus positive ionospheric storm effects. The electric field seems to be modulated by the solar wind ram pressure when such pressure changes become significant. Since this pressure term depends on the solar wind density, it is believed that it plays an essential role in the ring current intensification (Gonzalez *et al.*, 1994).

It is known, however, that the neutral wind and electric field effects on the ionosphere are dependent on the geomagnetic field configuration as the electrons are constrained to the magnetic

field lines. This is why geomagnetic latitude is preferred instead of geographic latitude to represent the distribution of the ionospheric parameters such as electron density (Mukhtarov *et al.*, 2013a) especially in low/equatorial latitude regions. Some of the most pronounced ionospheric effects seen at mid-latitude during storms are the long-lived negative and positive ionospheric phases that are coherent over a sizable geographic region (Fuller-Rowell *et al.*, 2000a). During the equinoxes, negative ionospheric storm effects occurred most frequently in spring, while in autumn positive and negative ionospheric storms have a relatively similar distribution (Matamba *et al.*, 2015).

Ionospheric storms can have significant impact on technological systems such as disruption of satellite communications, increased risk of radiation exposure to humans in space and in high-altitude aircraft, changes in atmospheric drag on satellites, errors in GNSS systems e.g. Global Positioning System (GPS), and loss of HF communications (Mukhtarov *et al.*, 2013a). Hence, the monitoring of the ionosphere, particularly during the geomagnetic storms, and modeling and forecasting the evolution of the ionospheric variability are among the essential undertakings of the ionosphere studies (Mukhtarov *et al.*, 2013a). The great interest in understanding the upper atmosphere response to geomagnetic storms has initiated the need to model and predict the ionospheric response (e.g. Cander, 1998; Fuller-Rowell *et al.*, 1998, 2000a,b; Muhtarov and Kutiev, 1998; Kutiev and Muhratov, 2001; Kutiev and Muhtarov, 2003; Jakowski *et al.*, 2006, 2012; Pietrella and Perrone, 2008; Mukhtarov *et al.*, 2013a,b). The necessity transpires for practical reasons like requirement for ground-to-ground communication via the ionosphere using HF radio propagation and from ground-to-satellite through the ionosphere at higher frequencies (Fuller-Rowell *et al.*, 2000b). The ionospheric parameter of interest is the F region $foF2$, which is related to the maximum usable frequency (MUF) for the oblique propagation of radio waves.

The study by (Gonzalez *et al.*, 1999) detailed the latitudinal variation of the ionospheric electric field during disturbed conditions. The electric field measurements were compared to interplanetary magnetic field component, auroral electrojet current, intensity of the asymmetric ring current as measured by a composite of several mid-latitude ground magnetometer stations. The zonal component of the sub-auroral electric field is found to be more sensitive than the meridional component to disturbances caused by rapid convection decreases. Another important reason is that the geophysical noise caused by neutral wind fluctuations in the zonal component of the E field is less at the magnetic equator than at mid-latitude regions (Gonzalez *et al.*, 1999).

Many recent studies have been conducted over the African region to understand the variation of the ionosphere during storm conditions based on ionospheric TEC maps, $foF2$ and other

ionospheric parameters (Poole and McKinnell, 2000; McKinnell and Poole, 2004b; Habarulema *et al.*, 2010; Adewale *et al.*, 2011; Amabayo *et al.*, 2012; Ngwira *et al.*, 2012, and references therein). Ngwira *et al.* (2012) investigated the ionospheric disturbances during the storm of 15 May 2005 over the South African mid-latitude region. They observed the ionospheric effects which were associated with equatorward neutral winds as well as the passage of traveling ionospheric disturbances (TIDs). In addition to the Ngwira *et al.* (2012) study, Habarulema *et al.* (2010) looked into understanding the ionospheric dynamics during two successive storms of 7-12 November 2004 in both the African equatorial and mid-latitude regions. During the analysis, Habarulema *et al.* (2010) were able to show a significant depletion in TEC and $foF2$ in the mid-latitude region. The studies by Adewale *et al.* (2011) and Amabayo *et al.* (2012) also investigated the ionospheric variations looking at different storm time periods in the African equatorial and mid-latitude regions respectively.

2.4   Ionospheric modeling

Ionospheric modeling began because of the substantial inquisitiveness in understanding the morphology and the physics of magnetic storm associated perturbations of the upper atmosphere as well as practical applications dependent on the ionosphere (Prölss, 1997). Extensive efforts have been made into the development of ionospheric models on a global as well as regional scales (e.g. Bilitza *et al.*, 1990, 2011, 2014; Fuller-Rowell *et al.*, 1998, 2000a; Hochegger *et al.*, 2000; Radicella and Leitinger, 2001; Bilitza and Reinisch, 2008; Radicella, 2009; Nava *et al.*, 2008, 2011). Some of the globally recognized ionospheric models include International Reference Ionosphere (IRI) and NeQuick which have both been widely evaluated (e.g. Coïsson *et al.*, 2006; Bilitza, 2009; Adewale *et al.*, 2012; Nigussie *et al.*, 2013; Habarulema and Ssessanga, 2017; Ahoua *et al.*, 2018; Mengistu *et al.*, 2018; Okoh *et al.*, 2018; Chekole *et al.*, 2019; Tariku, 2019).

The IRI is an empirical standard model that estimates plasma parameters of the ionosphere within an altitude range of 60 - 2000 km (Bilitza *et al.*, 1990; Bilitza and Reinisch, 2008; Bilitza *et al.*, 2011, 2014). This is a climatological model that describes monthly averages of electron density, electron temperature, ion temperature, ion composition, and several other parameters (Bilitza and Reinisch, 2008; Bilitza *et al.*, 2014, 2011). The Committee on Space Research (COSPAR) and the International Union of Radio Science (URSI) initiated the IRI project with the common goal of standardization of ionospheric modeling efforts (Bilitza and Reinisch, 2008; Bilitza *et al.*, 2014). The two groups are responsible for the improvements of the IRI model as new data and models becomes available (Bilitza *et al.*, 2011, 2014). Limitations of the IRI model with regards to the topside electron density profiles have been noted in many studies (e.g. Bilitza *et al.*, 2006; Coïsson *et al.*, 2006). One of the options used in the IRI model to

overcome these shortcomings is the NeQuick topside model (Hochegger *et al.*, 2000; Radicella and Leitinger, 2001).

The NeQuick is a quick-run model that describes ionospheric electron density above 100 km for trans-ionospheric propagation applications (Nava *et al.*, 2008; Radicella, 2009). The NeQuick model uses a profile formulation which includes five semi-Epstein layers with modeled thickness parameters, to describe the electron density of the ionosphere up to the peak of the F2 layer (Radicella, 2009). A semi-Epstein layer represents the electron density distribution in the top-side, with a height dependent thickness parameter empirically determined (Radicella, 2009). NeQuick 2 is the latest version of the model with main features illustrated in Nava *et al.* (2008) and Radicella (2009).

The other model which is incorporated within IRI, for better representation of the ionospheric properties during geomagnetic storm, is the STORM model (Fuller-Rowell *et al.*, 1998, 2000a). The performance of the STORM model has been reported in several studies (e.g. Araujo-Pradere *et al.*, 2002; Araujo-Pradere and Fuller-Rowell, 2002; Amarante *et al.*, 2007). The validation study by Araujo-Pradere *et al.* (2002) indicates that the STORM model provides a significant improvement during equinox and summer, but no quantitative improvement during the winter. The accuracy of the STORM model has been quantified and the results indicate that the model captures more than half of the increase in variability due to geomagnetic storms (Araujo-Pradere and Fuller-Rowell, 2002).

Numerous other modeling studies have been performed in an attempt to understand the iono-spheric responses during both quiet and geomagnetic storms at different geomagnetic latitude regions (e.g., Cander, 1998; Pietrella and Perrone, 2008; Fuller-Rowell *et al.*, 2000a; Kutiev and Muhtarov, 2003; Zhang *et al.*, 2011; Wang *et al.*, 2013; Mukhtarov *et al.*, 2013b), in-cluding physics-based models that analysis the energy dissipation into the ionosphere during solar storms (Burns *et al.*, 1995; Fuller-Rowell *et al.*, 2000a, and references therein). For ex-ample, Cander (1998) reported that artificial neural networks can be applied successfully in the modern development of numerical models for monthly median long-term prediction and daily hourly short-term forecasting. Pietrella and Perrone (2008) developed a local empirical ionospheric model for $foF2$ forecasting using an ionosonde station in Rome ($41.8°N, 12.5°E$). They reported that their model, which was specific to local data used in model development, provided "satisfactory" results for disturbed geomagnetic and ionospheric conditions. Another related study by Liu *et al.* (2004) looked at statistical modeling of ionospheric monthly median $foF2$ over a mid-latitude station Wuhan ($30.6°N, 114.4°E$). The model results provide a good agreement with observations, with standard deviations between 0.26 to 0.58 MHz (Liu *et al.*, 2004). Nishioka *et al.* (2017) recently did a statistical study to introduce the ionospheric storm

scale based on ionospheric $foF2$ and Total Electron Content (TEC) data over four stations in Japan. It is worth mentioning that in the Nishioka *et al.* (2017) study, not all ionospheric storms corresponded to geomagnetic storms. This is because of other factors at mid-latitude regions (such as thermospheric winds and neutral composition changes) influencing ionospheric storms (Prölss, 1995; Nishioka *et al.*, 2017) and not just geomagnetic storms.

Considering efforts made by scientists in developing global and regional ionospheric models, the ionosphere remains a dynamic and most variable region of interest to study especially during geomagnetic storms. The main focus of this thesis is the progress towards developing an ionospheric storm-time index by modeling the ionospheric $foF2$ response to geomagnetic storms over the South African region (southern hemisphere mid-latitude). More effort has been performed regionally with the focus on ionospheric modeling to understand the different physical drivers of the ionospheric changes during both quiet and disturbed conditions (e.g. McKinnell and Poole, 2004a,b; Habarulema *et al.*, 2009, 2011; Okoh *et al.*, 2010; Uwamahoro and Habarulema, 2015). In a recent study, Uwamahoro and Habarulema (2015) presented the modeling of TEC during geomagnetic storm conditions. The study was performed over the Sutherland $(32.38°S, 20.81°E)$ GNSS station. The results show good performance for storms with non-significant ionospheric TEC response as well as storms occurring during low solar activity period. However, storms with significant TEC response are not sufficiently captured by the model for the presented storms (Uwamahoro and Habarulema, 2015). This indicates that the storm-time ionospheric modeling is still a challenge and improvements on the accuracy of models in capturing the ionospheric responses remain crucial.

In addition to the modeling attempts made over the South African region, the current work is the effort towards the development of a regional ionospheric storm-time index based on $foF2$ data, which complements and supplements existing models for the region. The end results of the current work aim at addressing the near-real time operational need for application of HF communication users. Based on $foF2$ data, the modeling effort focuses on the actual responses (i.e. $\Delta foF2$) which is a quick indicator of either positive or negative ionospheric effects.

2.5   Summary

Brief introductory background information about the ionosphere, formation of the ionosphere and the different layers within the ionosphere were discussed. Electron density being one of the most importance parameters in the ionosphere and its relationship to critical frequency has been considered. This chapter also gave a brief overview of CME- and CIR-driven storms

together with responses of the ionosphere. A quick discussion on the importance of ionospheric modeling is also provided as well as highlighting some of the existing models. The aim of this chapter is to provide the foundation for the rest of the thesis, which covers the development of a regional ionospheric storm-time index.

Chapter 3

Data sources and modeling techniques

The critical frequency of the F2 layer, $foF2$, is an ionospheric parameter considered for the development and validation of ionospheric models and is measured using the ionosonde sounding technique in this work. In this chapter, a brief description of basic ionospheric sounding measurements is provided. An overview of TEC derived measurements from Global Navigation Satellite System (GNSS) sensors is provided together with geomagnetic and solar activity indices used in this study. This chapter also presents different modeling approaches explored for the development of ionospheric storm-time index based on $foF2$ data. These models include artificial neural networks (ANNs), regression analysis, and polynomial functions.

3.1   Ionosonde data

Since the experimental proof by Appleton and Barnett (1926) of the existence of the Kennelly-Heaviside (E) layer which also determined its height above the Earth's surface, various wireless methods of measuring the effective height at which the waves are reflected have been proposed (Appleton, 1932). The method class used by Appleton and Barnett (1926) is one in which the group-time is measured for a signal to travel from a sender to a receiver via the upper atmosphere (Appleton, 1932). Since then, sounding the ionosphere with ionospheric sounders or ionosondes has been the most important technique developed for the investigation of the global structure of the ionosphere, its diurnal, seasonal and solar cycle changes, and its response to solar disturbances (Rishbeth and Garriott, 1969; Basu *et al.*, 1985; Zolesi and Cander, 2014, and references therein). There are two possible methods of sounding the ionosphere, which are pulse and chirp sounding techniques (Rishbeth and Garriott, 1969; Basu *et al.*, 1985; Davies, 1990; Hunsucker, 1991, and references therein). The radio signals of a chirp sounder are continuous waves (CW) in which the frequency is modulated (Basu *et al.*, 1985; Davies, 1990). Initially, the chirp sounding technique was developed for oblique incidence and the pulse sounding for vertical incidence (Rishbeth and Garriott, 1969; Basu *et al.*, 1985). The important development of ionosonde instruments includes the transition from analog to digital sounding techniques in

the 1970s (Basu *et al.*, 1985; Reinisch *et al.*, 2008; Zolesi and Cander, 2014). Modern digital ionosondes (digisonde) have robust autoscaling software applications and are highly flexible HF radar systems. The monitoring functions of the ionosonde have enhanced the performance significantly (Reinisch *et al.*, 2008; Zolesi and Cander, 2014). One of the modern ionosondes is the Digisonde-4D also know as Digisonde Portable Sounder (DPS-4D) which is developed by University of Massachusetts Lowell Center for Atmospheric Research (UMLCAR) (`https://www.digisonde.com/index.html`). The "D" in the new model refers to the digital transmitters and receivers in the DPS-4D (Reinisch *et al.*, 2008). The ionosonde data analyzed in this project is measured using the modern ionosonde DPS-4D from four South African stations: Grahamstown $(33.32°S, 26.51°E)$, Hermanus $(34.42°S, 19.22°E)$, Louisvale $(28.50°S, 21.20°E)$, and Madimbo $(22.39°S, 30.88°E)$ as shown in Figure 3.1.
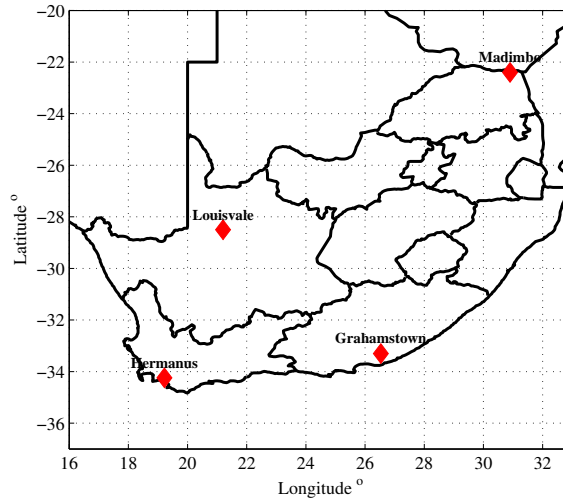
Figure 3.1: The South African network of ionosondes.

3.1.1 Basic ionospheric sounding principles

The concept of ionospheric sounding goes back to the early 1920s with experimental proof of the existence of an ionized layer (Breit and Tuve, 1926; Appleton, 1932). A digisonde is a type of radar capable of obtaining echoes from the ionosphere over a wide range of operating frequencies (Rishbeth and Garriott, 1969). There are many ways of probing the ionosphere using both ground- and space-based techniques. One of the techniques is the digisonde which probes the ionosphere for vertical and oblique incidence sounding. For a radio wave propagating through the ionosphere, a signal will encounter a medium with the following refractive index (Rishbeth and Garriott, 1969; Basu *et al.*, 1985; Zolesi and Cander, 2014):

$$n^2 = 1 - \left(\frac{f_N}{f}\right)^2 \tag{3.1}$$

27

where n is the refractive index which is dependent on the plasma frequency f_N given by

$$f_N = \sqrt{\frac{N_e e^2}{4\pi^2 \epsilon_0 m}} \qquad (3.2)$$

where N_e is the electron density measured in electrons/m^3, e is the electron charge, m is the mass of electron, ϵ_0 is the dielectric constant in a vacuum, and f is the radio wave frequency. Therefore substituting f_N into equation 3.1 results into:

$$n^2 = 1 - \frac{N_e e^2}{4\pi^2 \epsilon_0 m f^2} \qquad (3.3)$$

which shows that the refractive index is related to electron density within the ionosphere. The reflection in the ionosphere occurs when the radio wave frequency f is equal to the plasma frequency f_N (Zolesi and Cander, 2014).

Figure 3.2 is a simple demonstration of the propagation of a radio wave signal through the ionosphere along the path Tx-PQRT-Rx. A transmitter Tx, sends out a radio wave signal which enters the ionosphere at point P and is refracted by the electron density at a higher altitude. In this figure, θ and α are the angles of incidence at point P and refraction at point Q. The refraction angle at point R is 90°. Point R is the actual reflection height of the radio wave signal and point S is the virtual height. The signal exits the ionosphere at point T and returns back to the receiver, Rx. At higher frequencies, the refraction by electron density may not be sufficient for the signal to return the receiver (White, 1970).
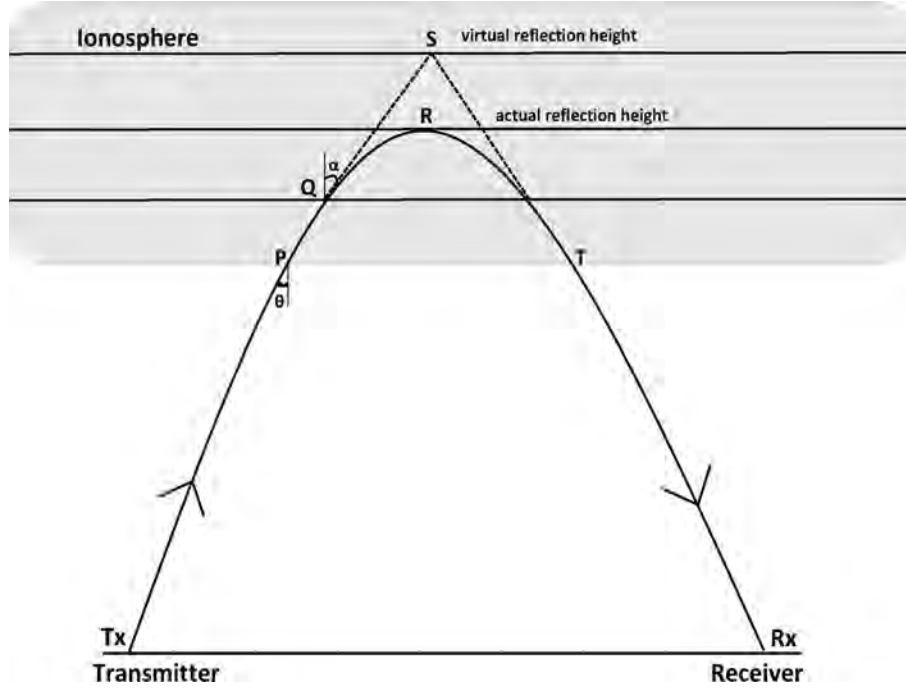
Figure 3.2: An illustrative example of the radio wave signal propagating through the ionosphere along the path Tx-PQRT-Rx. Adopted from White (1970).

The index of refraction outside and inside the ionosphere is respectively n_P and n_Q. As the radio wave penetrates the ionospheric layers, the electron density increases and the normal wave changes according to Snell's law:

$$n_P \; sin \, \theta = n_Q \; sin \, \alpha \tag{3.4}$$

At the top of the trajectory, point R, the angle $\alpha = 90^o$. At point P the index of refraction, n_P, outside the ionosphere is equal to 1. Therefore:

$$n_P \; sin \, \theta = n_R \; sin \, \alpha$$
$$sin \, \theta = n_R \; sin \, 90^o \tag{3.5}$$
$$n_R = sin \, \theta$$

For the case where the wave is nearly vertical within the ionosphere, the angle $\theta = 0$, hence $n_R = sin \, 0 = 0$. For the vertical sounding of the ionosphere $n^2 = 0$ in equation 3.3 and then:

$$f_c = \sqrt{\frac{N_e e^2}{4\pi^2 \epsilon_0 m}} \tag{3.6}$$

which is the maximum reflected incidence frequency, called the critical frequency, f_c. Frequencies less than f_c are reflected and will finally return to Earth. The critical frequency is reflected at a maximum height within the ionosphere. Hence, the maximum electron density with respect

to f_c is given by:

$$N_e(max) = \frac{4\pi^2 \epsilon_0 m f_c^2}{e^2} = 1.24 \times 10^{10} f_c^2 \; electrons/m^3 \tag{3.7}$$

which leads to the direct proportionality relationship between electron density N_e and the square of the critical frequency f_c. N_e and f_c are expressed in electrons/m^3 and in MHz respectively (Rishbeth and Garriott, 1969; White, 1970; Basu *et al.*, 1985; Davies, 1990; Zolesi and Cander, 2014).

The height at the point where the incidence frequency is reflected is called the virtual height (h'). The virtual height, also known as group height, is obtained from the time (t) it takes for the electromagnetic pulse to travel through the ionosphere and back as follows:

$$h' = \frac{ct}{2} = \int_0^h n' dh \tag{3.8}$$

where c is the velocity of the electromagnetic pulse in free space and n is the refractive index which is a function of electron density, N_e and critical frequency, f_c (Davies, 1990; Zolesi and Cander, 2014). It is important to note that n' varies along the propagation path which is the reason for integration over the whole path (McNamara, 1991). The simultaneous measurements of observable parameters of the radio wave signals reflected through the ionosphere are frequency, height for vertical incidence measurements, wave polarization, amplitude, phase and doppler shift & doppler spread. The way in which radio wave signals are reflected through the ionosphere is affected by the physical parameters of the ionospheric plasma. Therefore, it is possible to measure all of these observable parameters at a number of discrete heights and discrete frequencies to map out and characterize the structure of the ionosphere. Both the height and frequency dimensions of this measurement require several individual measurements to approximate the underlying continuous functions (LDI, 2015). The resulting measurement is called an ionogram, which is the graph of the virtual height, h', against the radio wave frequency.

3.1.2　Ionogram interpretation

Ionospheric sounding takes advantage of the refractive properties of the ionosphere. The frequencies of the propagating wave in the absence of the Earth's magnetic field and the inclusion of the magnetic field (magnetized plasma) are respectively known as plasma and gyro frequen-

cies. This is for the case of no collisions between electrons and the neutral atmosphere.

$$\text{Plasma frequency} : \omega_N^2 = (2\pi f_N)^2 = \frac{Ne^2}{m\epsilon_0} \tag{3.9}$$

$$\text{Gyro frequency} : \omega_H = 2\pi f_H = Be/m \tag{3.10}$$

where f_H is the gyro frequency and B is the geomagnetic flux density. Plasma frequency represents the frequency of free oscillation of the electrons. Gyro frequency is the frequency at which free electrons move in a circular motion around the magnetic field lines (Basu *et al.*, 1985; Zolesi and Cander, 2014). Consider the magnetic field vector B lying in the xy plane such that B_T is its component along the y axis, perpendicular to the direction of propagation of the wave, and B_L its component along the x axis in the same direction of propagation as shown in Figure 3.3.
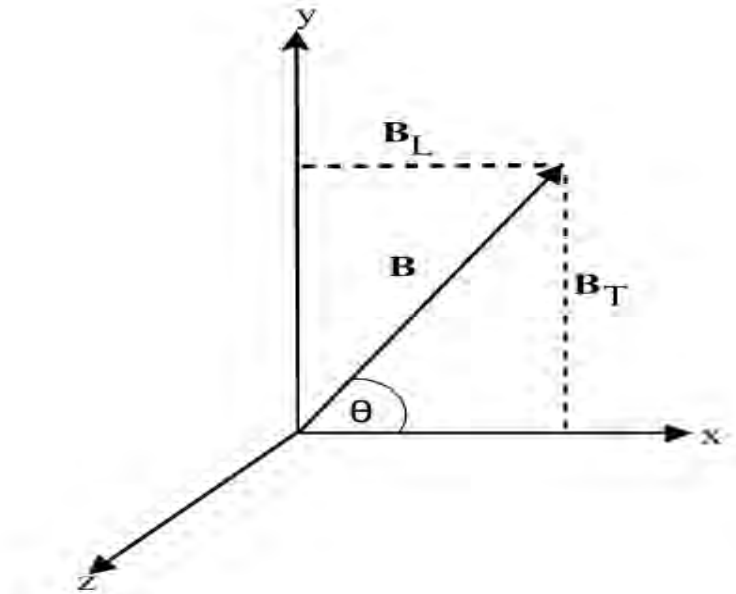
Figure 3.3: A diagram illustrating the system of orthogonal axes (Matamba, 2017, as adopted from Davies (1990)).

The dimensionless quantities X, Y and Z can be expressed as follows:

$$X = \frac{\omega_N^2}{\omega^2}; \quad Y = \frac{\omega_H}{\omega}; \quad Z = \frac{\nu}{\omega} \tag{3.11}$$

If θ is the angle between the direction of the wave normal and the magnetic field, then $Y_T = Y\sin\theta$ and $Y_L = Y\cos\theta$.

The Appleton-Hartree equation (Rishbeth and Garriott, 1969; Davies, 1990) for the complex index of refraction n is given by:

$$n^2 = 1 - \cfrac{X}{1 - iZ - \cfrac{Y_T^2}{2\left(1 - X - iZ\right)} \pm \sqrt{\left(\cfrac{Y_T^4}{4\left(1 - X - iZ\right)^2} + Y_L^2\right)}} \tag{3.12}$$

Assuming that the frequency of collisions within the ionosphere (at higher altitudes e.g., F2 region) is negligible in comparison with the frequency of the wave, so that $Z = 0$, then the real part of the Appleton-Hartree equation is:

$$n^2 = 1 - \cfrac{X}{1 - \cfrac{Y_T^2}{2\left(1 - X\right)} \pm \sqrt{\left(\cfrac{Y_T^4}{4\left(1 - X\right)^2} + Y_L^2\right)}} \tag{3.13}$$

$$= 1 - \cfrac{2X(1 - X)}{2(1 - X) - Y_T^2 \pm \sqrt{Y_T^4 + 4\left(1 - X\right)^2 Y_L^2}}$$

where the positive (+) and negative (-) signs refer to the ordinary and extraordinary waves respectively. In the absence of an external magnetic field, $Y_T = Y_L = 0$, Equation 3.13 of the Appleton-Hartree equation for the phase refractive index can be written in its simplest form as:

$$n^2 = 1 - X \tag{3.14}$$

Other approximations can be made to simplify the Appleton Hartree equation (Zolesi and Cander, 2014). If the propagation is almost perpendicular to the direction of the magnetic field, then:

$$Y_T^4 \gg 4(1 - X - iZ)^2 Y_L^2, \tag{3.15}$$

and if the propagation is almost parallel to the direction of the magnetic field, thus:

$$Y_T^4 \ll 4(1 - X - iZ)^2 Y_L^2 \tag{3.16}$$

Therefore, the refractive index is given by:

$$n^2 = 1 - \cfrac{X}{1 \pm Y_L} \tag{3.17}$$

The ordinary (O) and extraordinary (X) wave modes are circularly polarized in different directions. Consequently a plane polarized wave propagating through the ionosphere can be considered as the sum of ordinary and extraordinary components. The plane of polarization

continues to rotate alongside the wave path because of the different phase velocities for both ordinary and extraordinary components.

At the peak of an ionospheric layer, where the electron density N_e is greatest, the conditions $X = 1$ and $X = 1 - Y$ may be applied to find the critical frequencies f_o and f_x for the O and X modes respectively (Rishbeth and Garriott, 1969). That is, the minimum radio frequencies that can normally penetrate the layer in the O and X modes at vertical incidence angle (Rishbeth and Garriott, 1969; Davies, 1990; Basu *et al.*, 1985). The separation of the ordinary and extraordinary critical frequencies, f_o and f_x, can then be found from the definitions of X and Y.

It can be shown that the critical frequencies f_o and f_x, for $f_o \gg f_H$, are related by:

$$f_x - f_o \approx \frac{1}{2} f_H \tag{3.18}$$

$$X = 1 - Y \quad \Longrightarrow \quad \frac{f_o^2}{f_x^2} = 1 - \frac{f_H}{f_x}$$

$$\tag{3.19}$$

$$f_o^2 = f_x^2 - f_x f_H$$

Thus, the O and X modes at vertical incidence are separated by approximately half the gyro frequency f_H (McNamara, 1991). This equation also shows the magneto-ionic splitting due to the presence of the magnetic field in the ionospheric plasma (Basu *et al.*, 1985).
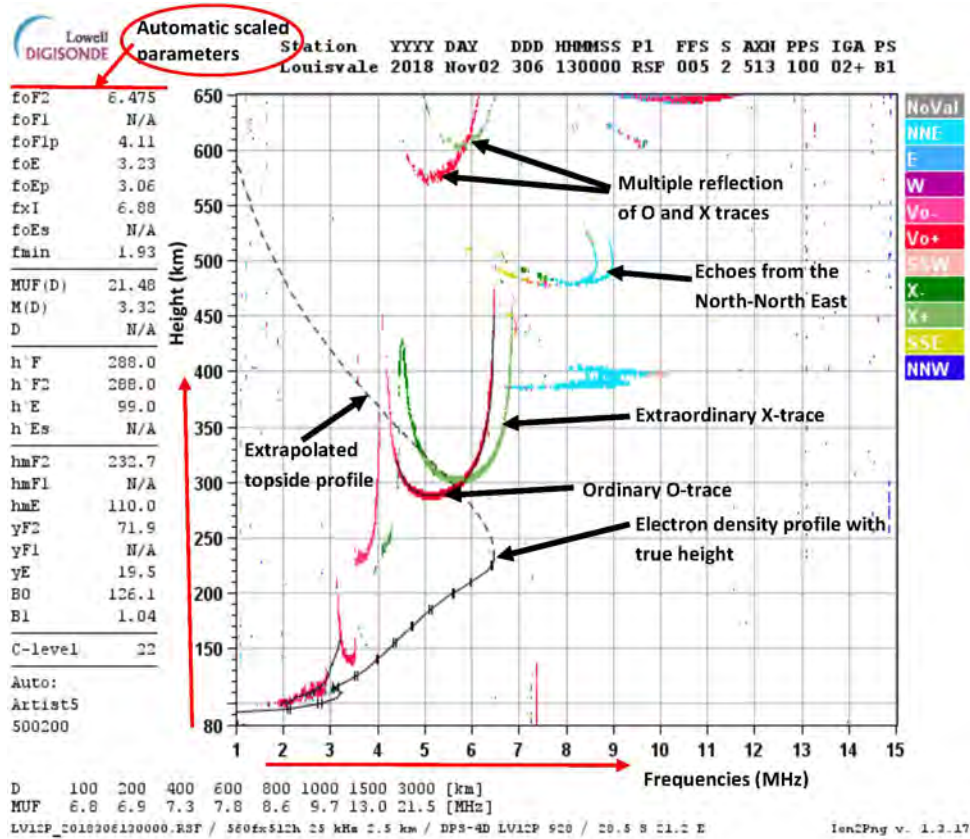
Figure 3.4: Daytime ionogram from Louisvale $(28.50°S, 21.20°E)$ ionosonde station, showing the virtual height in kilometers (km) versus frequency in MHz. The measurements of the ionospheric plasma parameters were recorded at 13:00 UT on 2 November 2018 with autoscaled values on the left.

Figure 3.4 shows an example of the daytime ionogram from a mid-latitude ionosonde station, Louisvale $(28.50°S, 21.20°E)$. The vertical axis show the virtual height from 80 - 650 km and the horizontal axis is the frequency from 1 - 15 MHz. The autoscaled values of the ionospheric parameters are presented on the left side of the ionogram with $foF2$ as the main parameter used in this study. The program that computes the autoscaled data for the South African ionosonde network is called Automatic Real Time Ionogram Scaler with True Height (ARTIST). This system was developed at the University of Massachusetts Lowell Center for Atmospheric Research (UMLCAR). For details on ARTIST and some autoscaled ionograms using this system, readers are referred to (Reinisch and Huang, 1983; Reinisch *et al.*, 1983; McNamara, 2006; Galkin and Reinisch, 2008, and references therein). The O and X waves are clearly seen by the red and the green traces respectively. The electron density profile with true height as well as extrapolated topside profile are also indicated. It is also interesting to know that the South African ionosonde stations are synchronized and can simultaneously record vertical and oblique ionogram traces. Looking at Figure 3.4, clear echoes from North-North East (NNE) is observed by the cyan traces. In this case, looking at the station locations in Figure 3.1 of section 3.1, it is evident that Louisvale is receiving echoes from the Madimbo station. It is presented in the

study by Verhulst *et al.* (2017) that this additional information is important for the study of traveling ionospheric disturbances (TIDs) .

The $foF2$ is one of the most important parameters for HF communication due to the continuous presence of the F2 layer. HF radio relies heavily on variations within the ionospheric F2 layer and remains the primary means of communication over the region of study interest. Therefore, it is important to study the changes within this region especially during storm time. Since the primary purpose of this work is to develop an ionospheric storm time index that can capture ionosphere responses during geomagnetic storms, the deviation $\Delta foF2$ has been calculated using the following expression:

$$\Delta foF2 = \left(\frac{foF2 - foF2_m}{foF2_m} \right) \times 100 \tag{3.20}$$

where $foF2_m$ is the monthly median of $foF2$ values. $\Delta foF2$ is used to define the quiet time ionospheric variability between $\pm 20\%$ as applied in other studies (Danilov, 2001; Gao *et al.*, 2008; Matamba *et al.*, 2015). If the values of $\Delta foF2$ are less than -20% or greater than +20%, then they are known as negative or positive ionospheric storms respectively. HF or satellite communication can be highly affected during geomagnetic disturbed days and correcting for the impacts on these systems requires an extensive network of ionospheric measurement, rapid modeling, and rapid dissemination of correction information (Schrijver *et al.*, 2015). In light of these, measurements from a Global Navigation Satellite System (GNSS) network have been used to supplement the ionosonde network.

3.2   Global Navigation Satellite System (GNSS)

Global navigation satellite system (GNSS) refers to a constellation of satellites providing signals from space that transmit positioning and timing data to GNSS receivers with the main objective as navigation. There are a number of GNSS constellations some of which are either fully operational or in a development process. Such constellations are the United States' Global Positioning System (GPS), the Russian Federations' GLObal NAvigation Satellite System (GLONASS), Europe's European Satellite Navigation System (GALILEO), China's Navigation Satellite System BeiDou, India's Regional Navigation Satellite System (IRNSS) and Japan's Quasi-Zenith Satellite System (QZSS) (Kaplan and Hegarty, 2005; Misra and Enge, 2006). The GNSS constellation which has been in operation for a longer period of time is the GPS network which determines with high accuracy, the position, velocity, and in some cases, the attitude (or object orientation) of an object (or user) in space or on the Earth (Misra and

Enge, 2006). The following description will be limited to GPS satellites because the TEC data used in this study were derived from GPS measurements.

3.2.1   Global Positioning System (GPS) Satellite

Global Positioning System (GPS) is a GNSS constellation with baseline configuration of at least 24 satellites. The satellites within this constellation are positioned in six Earth-centered orbital planes inclined at 55° with respect to the equator with four satellites in each plane (Kaplan and Hegarty, 2005). This satellite constellation enables a 24-hour user navigation and time determination capability worldwide. The GPS constellation was established by the U.S. Department of Defense (DoD) with the primary objective to offer the U.S. military with accurate positioning, velocity, and timing (PVT) information (Misra and Enge, 2006). Nonetheless, civilian use, including scientific research, surveying, precision agriculture, etc, was later granted.

The GPS network provides two main services; Standard Positioning Service (SPS) for civil use and the Precise Positioning Service (PPS) for the DoD and other authorized users (Misra and Enge, 2006; Kaplan and Hegarty, 2005). The GPS sensors consists of three segments known as space, control and user segments. The space and control segments are responsible for the management of the satellite operations whereas the user segment covers the activities related to development of military and civil GPS user equipment/receiver (Misra and Enge, 2006). The GPS space segment consists of a baseline constellation of 24 satellites as illustrated in Figure 3.5, in medium Earth orbit (MEO) at an altitude of $\sim$ 20,200 km (Hofmann-Wellenhof *et al.*, 1992; Misra and Enge, 2006). The MEO was determined to be more preferable for GPS constellation than the Low and Geosynchronous Earth orbits (LEO and GEO) because of the global coverage, dilution of precision characteristics,and cost (Kaplan and Hegarty, 2005). The constellation was designed in such a way that at least four satellites are visible at or near the Earth at any one time. The GPS control segment comprises of a global network of ground facilities which includes master control stations, monitor stations, and ground control stations. The primary operational responsibilities of the control segment includes tracking and monitoring satellite transmission for the orbit and clock determination and prediction, time synchronization, perform analysis, and upload data messages to the satellite constellation (Hofmann-Wellenhof *et al.*, 1992; Misra and Enge, 2006).
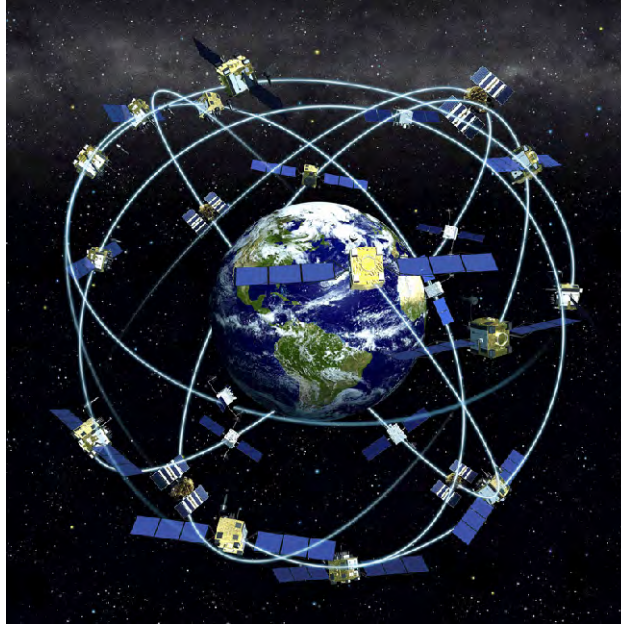
Figure 3.5: Baseline GPS constellation consisting of 24 satellites in orbital planes inclined at about 55° with respect to the Earths equatorial plane. Credit: National Oceanic and Atmospheric Administration (NOAA) (`https://www.space.com/19794-navstar.html`).

The user segment of the satellite constellation has two main user groups, that is military and civilian. The segment includes a receiver and antenna which receives signals from GPS satellites and uses the transmitted information to calculate the user's position, velocity and time (Hofmann-Wellenhof *et al.*, 1992, ; `https://www.gps.gov/systems/gps/`). These signals propagate through different layers of the atmosphere and are attenuated especially in the ionosphere where the electron density is high.

3.2.2   GPS Satellite Observations

The L-band has the operating frequency ranging between 1 - 2 GHz in the radio spectrum and signals transmitted by GPS satellites are within this band. GPS satellite signals are transmitted continuously using two radio frequencies in the L-band commonly known as Link 1 (L_1) and Link 2 (L_2) which are centered respectively at frequencies f_1 (1575.42 MHz) and f_2 (1227.6 MHz). f_1 and f_2 are derived from a fundamental frequency $f_o = 10.23$ MHz such that $f_1 = 154 f_o$ and $f_2 = 120 f_o$ (Hofmann-Wellenhof *et al.*, 1992; Misra and Enge, 2006). The other signal link transmitted by the GPS satellite is the L5, with the allocated frequency band centered at $f_5 = 1176.45$ MHz such that $f_5 = 115 f_o$. Each GPS satellite transmits two Pseudo Random Noise (PRN) codes known as Precise (P) and Coarse/Acquisition (C/A) codes and a navigation message for its identification and position determination respectively. The C/A-code is reserved for civilians and is purposely modulated on L_1 only, whereas the P-code is modulated on both L_1 and L_2 and is for US military and authorized users. The two fundamental observations from GPS Satellite receivers are: (i) pseudorange and (ii) carrier phase measurements.

(i) The pseudorange measurements P_1 and P_2 at L_1 and L_2 are given by (Carrano and Groves, 2009):

$$P_1 = \rho + c(\Delta t_r - \Delta t_s) + I_1 + T + b^r_{P_1} + b^s_{P_1} + m_{P_1} + \varepsilon(P_1) \tag{3.21}$$

$$P_2 = \rho + c(\Delta t_r - \Delta t_s) + I_2 + T + b^r_{P_2} + b^s_{P_2} + m_{P_2} + \varepsilon(P_2) \tag{3.22}$$

where:

P: Pseudorange (m),

ρ: True geometric range (m) between the satellite and the receiver,

Δt_r: Receiver clock errors (s),

Δt_s: Satellite clock errors (s),

I: Pseudorange ionospheric delay (m),

T: Pseudorange tropospheric delay (m),

$b^r_{P_1}$, $b^r_{P_2}$: Instrumental receiver biases,

$b^s_{P_1}$, $b^s_{P_2}$: Instrumental satellite biases,

m_{P_1}, m_{P_2}: Multipath effect (m)

$\varepsilon(P_1)$, $\varepsilon(P_2)$: Thermal noise (m)

Taking the difference of the pseudorange measurements neglecting multipath and thermal noise allows, the geometric range, clock error and tropospheric delay to cancel out.

$$P_2 - P_1 = I + b^s_P + b^r_P \tag{3.23}$$

where

$$I = I_2 - I_1, b^s_P = b^s_{P_2} - b^s_{P_1}, b^r_P = b^r_{P_2} - b^r_{P_1}$$

substituting the ionospheric delay given by:

$$I = \frac{40.3}{f^2}\text{TEC} \tag{3.24}$$

Equation 3.23 becomes:

$$P_2 - P_1 = 40.3\left(\frac{1}{f_2^2} - \frac{1}{f_1^2}\right)\text{TEC} + b^s_P + b^r_P \tag{3.25}$$

Therefore, solving for TEC in terms of pseudorange measurements at frequencies f_1 and f_2 yields:

$$\text{TEC} = \frac{1}{40.3}\left(\frac{(f_1 f_2)^2}{f_1^2 - f_2^2}\right)\left\{(P_2 - P_1) - (b^s_P + b^r_P)\right\} \tag{3.26}$$

If the bias terms in Equation 3.26 are ignored and the values of f_1=1575.42 and f_2=1227.6 MHz are substituted, the pseudorange TEC can be expressed in units of TECU as follows:

$$\text{TEC} = 9.524(P_2 - P_1) \text{ TECU} \tag{3.27}$$

where 1 TECU is equal to 10^{16} electrons per square meter (el/m^2)

(ii) The carrier-phase observation equations are given by:

$$\Phi_1 = \rho + c(\Delta t_r - \Delta t_s) + I_1 + T + b^r_{\Phi_1} + b^s_{\Phi_1} + \lambda_1 N_1 + m_{\Phi_1} + \varepsilon(\Phi_1) \tag{3.28}$$

$$\Phi_2 = \rho + c(\Delta t_r - \Delta t_s) + I_2 + T + b^r_{\Phi_2} + b^s_{\Phi_2} + \lambda_2 N_2 + m_{\Phi_2} + \varepsilon(\Phi_2) \tag{3.29}$$

where:

Φ: Carrier phase (m),

λ: Carrier signal wavelength (m),

N: Carrier phase cycle-ambiguity,

I: Pseudorange ionospheric delay (m),

$b^r_{\Phi_1}$, $b^r_{\Phi_2}$: Instrumental receiver biases,

$b^s_{\Phi_1}$, $b^s_{\Phi_2}$: Instrumental satellite biases,

m_{Φ_1}, m_{Φ_2}: Multipath effect (m)

$\varepsilon(\Phi_1)$, $\varepsilon(\Phi_2)$: Thermal noise (m)

Similar to the pseudorange case, omitting multipath and thermal noise, the difference between the carrier-phase measurements eliminates the geometric range, clock error and tropospheric delay such that:

$$\Phi_2 - \Phi_1 = \lambda N + I + b^s_\Phi + b^r_\Phi \tag{3.30}$$

where

$$\lambda N = \lambda_2 N_2 - \lambda_1 N_1, b^s_\Phi = b^s_{\Phi_2} - b^s_{\Phi_1}, b^r_\Phi = b^r_{\Phi_2} - b^r_{\Phi_1}$$

Substituting I in Equation 3.30 by Equation 3.24, the above equation can be written as:

$$\Phi_2 - \Phi_1 = 40.3\left(\frac{1}{f_2^2} - \frac{1}{f_1^2}\right)\text{TEC} + (\lambda_1 N_1 - \lambda_2 N_2) + (b^s_\Phi + b^r_\Phi) \tag{3.31}$$

Determining the value of TEC in the absence of ambiguities and biases yields:

$$\text{TEC} = 9.524(\Phi_2 - \Phi_1) \text{ TECU} \tag{3.32}$$

This equation provides precise measurements that are ambiguous due to the presence of the integer ambiguities which is contrary to Equation 3.27 that gives imprecise measurements that

are unambiguous due to the presence of noise (Misra and Enge, 2006; Carrano and Groves, 2009).

3.2.3 Ionospheric effect on GPS signals

The ionosphere is a dispersive medium, which means that the refractive index and the wave propagation speed depend on the signal frequency. The relation of dispersion of the ionosphere as a function of the plasma angular frequency, $\omega_N = 2\pi f_N$ and electromagnetic signal angular frequency, $\omega = 2\pi f$ is given by (e.g. Rishbeth and Garriott, 1969; Davies, 1990):

$$\omega^2 = c^2 k^2 + \omega_N^2 \tag{3.33}$$

The phase and group velocities are given by:

$$v_{ph} = \frac{\omega}{k} = \frac{c}{\sqrt{1 - \left(\frac{\omega_N}{\omega}\right)^2}} \tag{3.34}$$

and

$$v_{gr} = \frac{d\omega}{dk} = c\sqrt{1 - \left(\frac{\omega_N}{\omega}\right)^2} \tag{3.35}$$

The refractive index of a medium, $n = c/v$, being defined as the ratio of the speed of propagation of the signal in a vacuum to the speed of propagation of the signal in that medium, v (Hofmann-Wellenhof *et al.*, 1992). The phase and group refractive index can be expressed by:

$$n_{ph} = \frac{c}{v_{ph}} = \sqrt{1 - \left(\frac{\omega_N}{\omega}\right)^2} \tag{3.36}$$

$$n_{gr} = \frac{c}{v_{gr}} = \frac{1}{\sqrt{1 - \left(\frac{\omega_N}{\omega}\right)^2}} \tag{3.37}$$

substituting ω_N/ω by f_N/f, the phase and group refractive indices are expressed as follows:

$$n_{ph} \approx 1 - \frac{1}{2}\left(\frac{f_N}{f}\right)^2 \tag{3.38}$$

$$n_{gr} \approx 1 + \frac{1}{2}\left(\frac{f_N}{f}\right)^2 \tag{3.39}$$

Replacing the plasma frequency

$$n_{ph} = 1 - \frac{40.3}{f^2}N_e \tag{3.40}$$

$$n_{gr} = 1 + \frac{40.3}{f^2} N_e \tag{3.41}$$

Note the equation above $n_{gr} > n_{ph}$ which means $v_{gr} < v_{ph}$. Equations 3.40 and 3.41 are the first order approximation. Thus, GPS code/group measurements are delayed while carrier phase measurements are advanced by the presence of the ionosphere (Hofmann-Wellenhof *et al.*, 1992; Misra and Enge, 2006).

Due to the non-uniform composition of the ionosphere, the time (τ) it takes a GPS signal to travel from the satellite to receiver is longer than the time (τ_0) it would have taken the same signal through a vacuum (Misra and Enge, 2006). The difference in these times, that is $\Delta\tau = \tau - \tau_0$, is known as ionospheric time delay. The time delay can be expressed in mathematical form as follows:

$$\Delta\tau = \frac{1}{c} \int_s^r \Big(n(l) - 1 \Big) dl \tag{3.42}$$

while the corresponding delay in path length is given by:

$$\Delta\rho = \int_s^r \Big(n(l) - 1 \Big) dl \tag{3.43}$$

substituting equation 3.40 and 3.41 into equations 3.42 and 3.43, it follows that the excess phase delay in seconds and in meters are:

$$\Delta\tau_{ph} = -\frac{40.3}{cf^2}.\text{TEC} \tag{3.44}$$

$$I_\Phi = -\frac{40.3}{f^2}.\text{TEC} \tag{3.45}$$

In a similar way, the group delay in seconds and in meters are expressed respectively as:

$$\Delta\tau_{gr} = \frac{40.3}{cf^2}.\text{TEC} \tag{3.46}$$

$$I_\rho = \frac{40.3}{f^2}.\text{TEC} \tag{3.47}$$

where TEC is the ionospheric total electron content and is defined as the integral of electron density in a unit cross-sectional area along the radio wave paths from a satellite transmitter to a ground-based receiver (Hofmann-Wellenhof *et al.*, 1992):

$$\text{TEC} = \int_s^r N_e dl \tag{3.48}$$

It is clear from the equations above that the GPS signal delay is dependent on the electron density along the propagation path from satellite to a receiver. The magnitude of the error

introduced by the ionosphere can vary depending on the path length. There are large errors when the satellite is near the observers' horizon, that is the signal path is longer that when it is directly overhead.
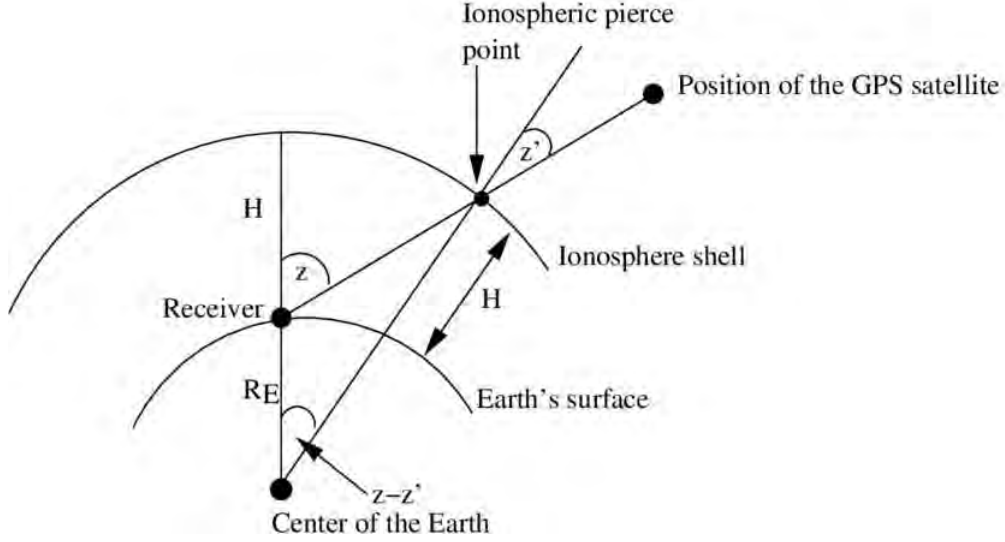
Figure 3.6: A schematic illustration of geometrical mapping of slant TEC (STEC) to vertical TEC (VTEC) (Habarulema, 2010, as adopted from Hofmann-Wellenhof *et al.* (1992)).

TEC measured along the signal path from satellite to receiver is called Slant Total Electron Content (STEC). Vertical TEC (VTEC) refers to TEC encountered along the vertical/zenith direction with respect to the receiver location. To obtain vertical TEC, a suitable mapping function is used which takes into account the satellite zenith distance (Hofmann-Wellenhof *et al.*, 1992). Figure 3.6 is a typical geometric representation of the thin-shell ionosphere. The expression below shows the mapping function used to convert STEC to VTEC with the assumption that the ionosphere is a single thin shell at the mean ionospheric height H.

$$\text{TEC} = \frac{1}{cosz'}\text{VTEC} \tag{3.49}$$

where z' is the zenith angle of the satellite at the ionospheric pierce point (IPP). The IPP is the intersection of the line of sight between GPS receiver and the observed satellite with the thin shell ionosphere. The relationship between the satellite zenith angle z at the receiver position and z' is obtained from the following expression:

$$sinz' = \frac{R_E}{R_E + H}sinz \tag{3.50}$$

where R_E is the radius of Earth which is ~ 6378 km and H is the mean ionospheric height with typical values between 300 km and 400 km (Hofmann-Wellenhof *et al.*, 1992, 2007).

3.2.4   GPS TEC data processing

To obtain GPS TEC data, measurements recorded in the Receiver INdependent EXchange (RINEX) format were downloaded from the South African Chief Directorate: National Geospatial Information TrigNet GPS receiver network (`ftp://ftp.trignet.co.za`). TEC data were derived at 30 seconds using a GPS TEC analysis software developed at Boston College (Seemala and Valladares, 2011) from GPS observables recorded by dual frequency receivers. TEC values are obtained by calculating the average TEC for individual satellites. Figure 3.7 represents an example of such data with TEC for individual PRNs in black lines and red lines showing averaged TEC values for a 24-hour period.
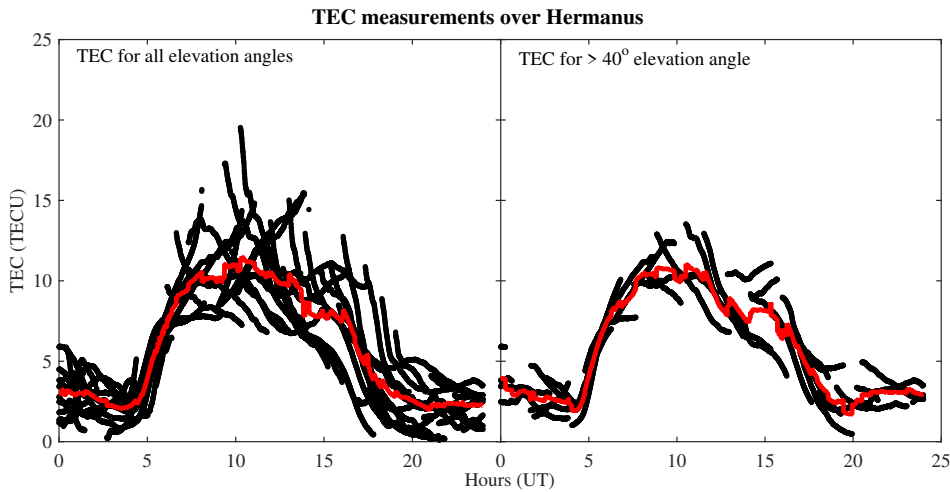
Figure 3.7: TEC data over Hermanus (HNUS) GPS receiver station with no elevation angle selected (left) and with elevation angle of greater than 40° (right) for the 9th September 2017, geomagnetic storm day. The black lines indicate TEC values for individual PRNs with red line showing the averaged TEC values.

It is well known that some errors are introduced during GPS TEC processing with possible sources from instrumental biases, mapping function, and assumptions made during different steps involved in TEC processing (Klobuchar *et al.*, 1995; Parkinson *et al.*, 1996; Ho *et al.*, 1997). The process of TEC derivation reads GPS raw data in RINEX format and computes the relative slant TEC along with the satellite positions. The satellite and receiver biases are then estimated and removed to obtain the absolute slant TEC which is then used together with the position and height of the IPP to calculate the vertical TEC (Burrell *et al.*, 2009; Uwamahoro *et al.*, 2018a). The GPS TEC software used in this study uses the cycle slip correction of the phase TEC by calculating the difference between successive TEC values and comparing with the mean difference of the previous 20 TEC values. The differential satellite bias corrections are used to remove satellite biases and published by University of Bern (ftp://ftp.unibe/aiub/CODE). The detailed steps in estimating the biases are described in Uwamahoro *et al.* (2018a). The GPS TEC analysis software used in this study assumes an IPP height of 350 km. To minimize

multipath effects and concurrently keeping useful amount of data, VTEC values corresponding to elevation angles of greater than 40° were considered when developing the relationship function between VTEC and $foF2$ from ionosonde measurements. In addition, the higher elevation angle 40° was adopted because of the comparison with ionosonde measurements which are obtained from the vertical incidence sounders. Figure 3.7 is a typical example of the VTEC data presented in black curves with no elevation angle (left) and with selected elevation angle of greater than 40° (right) during a day of geomagnetic storm conditions, 9 September 2017. It is important to note that the GPS-TEC software used in this study has been used substantially to derive TEC as reported in different studies (e.g. Adewale *et al.*, 2011; Seemala and Valladares, 2011; Matamba *et al.*, 2015; Uwamahoro *et al.*, 2018a).

3.3 Geomagnetic activity indices

During geomagnetic storm conditions the horizontal component, H, of the Earth's magnetic field is depressed (Sugiura and Kamei, 1991). Studies have shown that the decrease in H during geomagnetic storms at equatorial and mid-latitudes can approximately be represented by a uniform magnetic field parallel to the geomagnetic dipole axis and directed toward south (Sugiura, 1963; Sugiura and Kamei, 1991). The magnitude of this axially symmetric disturbance field varies with storm-time, characterized as the time measured from the storm onset. The global sudden increase in H generally indicates the onset of a geomagnetic storm, referred to as the storm sudden commencement (SSC). It is generally preferable to have some estimate of the level of dissipation of energy within the magnetosphere at any given time as mentioned by Rostoker (1972), hence the development of geomagnetic indices. In this section different geomagnetic indices used in this study will be discussed.

3.3.1 The disturbance storm time (Dst) index

The disturbance storm time (Dst) index is a measure of geomagnetic activity used to assess the severity of magnetic storms. It is expressed in nanoteslas (nT) and is based on the average value of the horizontal (H) component of the Earth's magnetic field measured hourly at four near-equatorial geomagnetic observatories. Use of the Dst as an index of storm strength is possible because the strength of the surface magnetic field at low latitudes is inversely proportional to the energy content of the ring current, which increases during geomagnetic storms (Sugiura and Kamei, 1991; Banerjee *et al.*, 2012). Thus negative values of Dst index indicate that the Earth's magnetic field is weakened which is clearly the case during storm conditions. The decreases in magnetic field are produced mainly by the equatorial current system in the magnetosphere, also known as ring current (Sugiura and Kamei, 1991). More severe storms are expressed with higher negative-values of Dst index.

Table 3.1: Locations of the geomagnetic observatories used to derive disturbance storm time (Dst) (Sugiura and Kamei, 1991), symmetric disturbance field in the H component (SYM-H), and Auroral Electrojet Index (AE) indices.

Station		Geographic		Geomagnetic
Name	Code	Longitude	Latitude	Latitude
Dst index stations				
Hermanus	HER	19.22^o	-34.40^o	-42.33^o
Kakioka	KAK	140.18^o	36.23^o	29.04^o
Honolulu	HON	201.98^o	21.32^o	21.66^o
San Juan	SJG	293.85^o	18.01^o	28.69^o
SYM-H index stations				
Alibag	ABG	72.87^o	18.64^o	9.9^o
Martin De Vivies	AMS	77.57^o	-37.80^o	-46.9^o
Boulder	BOU	254.76^o	40.13^o	48.7^o
Chambon La Foret	CLF	2.26^o	48.03^o	50.1^o
Fredericksburg	FRD	282.63^o	38.2^o	49.1^o
Hermanus	HER	19.22^o	-34.40^o	-42.33^o
Honolulu	HON	201.98^o	21.32^o	21.66^o
Mamembetsu	MMB	144.19^o	43.91^o	34.6^o
San Juan	SJG	293.85^o	18.01^o	28.69^o
Tucson	TUC	249.27^o	32.17^o	40.4^o
Urumqi	WMQ	87.7^o	43.8^o	40.14^o
AE index stations				
Abisko	ABK	18.82^o	68.36^o	66.04^o
Dixon Island	DIK	80.57^o	73.55^o	63.02^o
Cape Chelyuskin	CCS	104.28^o	77.72^o	66.26^o
Tixie Bay	TIK	129°	71.58^o	60.44^o
Cape Wellen	CWE	190.17^o	66.17^o	61.79^o
Barrow	BRW	203.25^o	71.30^o	68.54^o
College	CMO	212.17^o	64.87^o	64.63^o
Yellowknife	YKC	245.6^o	62.4^o	69°
Fort Churchill	FCC	265.9^o	58.8^o	68.7^o
Poste-de-la-Baleine	PBQ	282.22^o	55.57^o	66.58^o
Narsarsuaq	NAQ	314.16^o	61.2^o	71.21^o
Leirvogur	LRV	338.3^o	64.18^o	70.22^o
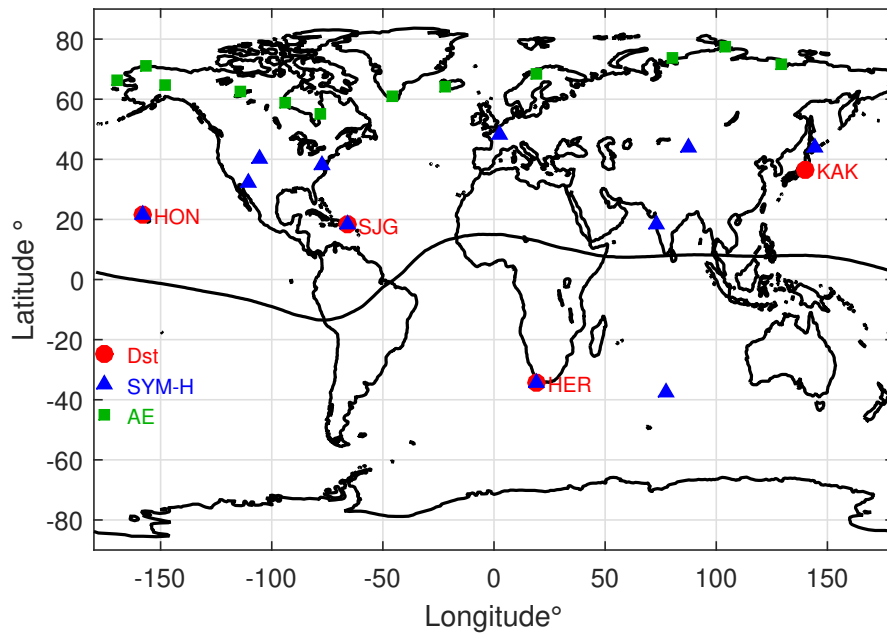
Figure 3.8: Locations of geomagnetic observatories used to compute SYM-H (blue triangles), Dst (red dots), and AE (green squares) indices. The black line represents the geomagnetic equator.

The Dst index data is derived from four global geomagnetic observatories which are Hermanus, Honolulu, Kakioka, and San Juan. Table 3.1 represents these four stations with their geographic longitude and latitude as well as geomagnetic latitude coordinates. These stations were considered based on their location far from equatorial and auroral electrojets, stations that are equally distributed over the longitude sector, their quality and reliable data of hourly H values (Sugiura, 1963). Figure 3.8 displays a map view of these stations plotted in red dots and a clear longitudinal equidistant of the stations is visible. The magnetic equator is plotted as a black line in Figure 3.8 to illustrate that the stations are located far away from the equator. This indicates the absence of external influences to the magnetic measurements which may originate from equatorial electrojet variations. This network of magnetic observatories lie well within the mid-latitude regions and possible auroral zone disturbances are also avoided (Sugiura, 1963).

The World Data Centre (WDC) for Geomagnetism, Kyoto is the home for the geomagnetic equatorial Dst index data. There are three versions of Dst index data known as the final Dst index, provisional Dst index and real-time/quicklook Dst index. Each version is based on the degree of data processing provided by the observatories. The real-time Dst index is provided for monitoring, diagnostics, and forecasting purposes only because of use of unverified raw data may have inaccuracies. The Dst index can be downloaded from `http://wdc.kugi.kyoto-u.ac.jp`. The Dst index data was used in this study as a selection criteria for storm time data.

3.3.2   SYM-H index

Longitudinally symmetric (SYM) and asymmetric (ASY) disturbance indices were introduced to describe the geomagnetic disturbance fields at mid-latitudes. These indices are derived with high-time resolution (1 minute) for both horizontal (H) and declination (D) components. That is, four indices are derived: two for the components in the horizontal (dipole pole) direction H (SYM-H, ASY-H) and another two in the orthogonal (East-West) direction D (SYM-D, ASY-D) (Nosé *et al.*, 2012). The following description will now be limited to SYM-H index because it is one of the modeling input parameters considered in this study.

The symmetric disturbance field in the H component, SYM-H, is essentially the same as hourly Dst index. SYM-H values are derived from different sets of stations with a slightly different coordinate system than Dst values (Wanliss and Showalter, 2006; Nosé *et al.*, 2012). The SYM-H index observatory network is represented by blue triangles in Figure 3.8. It can be seen in Figure 3.8 that the only station used in Dst index derivation which is not included in SYM-H index derivation is Kakioka. These indices also vary because of the distinct methods used for baseline subtraction (Wanliss and Showalter, 2006). SYM-H is used over Dst index because of its advantage of having higher time resolution (1-minute) data as compared to hourly Dst index data (e.g., Wanliss and Showalter, 2006; Li *et al.*, 2011). In addition, the effect of solar wind dynamic pressure variation is more pronounced in SYM-H than hourly Dst-index as reported in the study of Wanliss and Showalter (2006). Furthermore, since SYM-H uses more observatories, more evenly distributed in longitude, it provides a greater description of the longitudinal variations of the disturbance field. For the derivation of each month, only six of the stations are used. Some stations are backed up by others depending on the availability and the condition of the monthly data. The data is processed in units of one month. The essential procedure for the derivation consists of subtraction of the geomagnetic main field and the solar quiet (Sq) field current to calculate the disturbance field component. Coordinate transformation to a dipole coordinate system is important. Thus, the H direction at each observatory is generally different from the dipole pole direction because of the local geomagnetic anomalies. The other step in the derivation procedure is to calculate the longitudinally symmetric component (Nosé *et al.*, 2012). The longitudinal symmetric component is computed by averaging the disturbance component at each minute for the six stations. A latitudinal correction is made on the averaged value for the H components to get the value of SYM-H index. The SYM-H data can be obtained from WDC, Kyoto (`http://wdc.kugi.kyoto-u.ac.jp/aeasy/index.html`).

3.3.3   Auroral electrojet (AE) index

The Auroral Electrojet Index, AE, is designed to provide a global, quantitative measure of auroral zone magnetic activity produced by enhanced ionospheric currents flowing below and

within the auroral oval (e.g., Davis and Sugiura, 1966; Kamide and Akasofu, 1983). AE index is useful in studying the morphology of ionospheric effects during storm/sub-storm activities (Kamide and Akasofu, 1983). There are twelve selected observatories along the auroral zone in the northern hemisphere which are used for deriving the AE index and are shown in Figure 3.8 (green squares). This index is also derived from the horizontal H component observations of the geomagnetic variations. Similar to Dst and SYM-H indices, the base value is subtracted from each value of 1-minute data obtained at the station during that month to normalize the data. Then, within the dataset from all the stations, the largest and smallest values are selected at each given time (UT). The largest and the smallest values correspond respectively to AU and AL indices, which form the upper and lower envelopes of the superposed plots (Nosé *et al.*, 2012). The difference (AU - AL) defines the AE index, and the AO index is the mean value of the AU and AL. The purpose of AU and AL indices is to indicate the strongest current intensity of the eastward and westward auroral electrojets respectively. The AO index gives a measure of the equivalent zonal current while the AE index represents the overall activity of the electrojets. AE index data is available from different sources such as `http://wdc.kugi.kyoto-u.ac.jp/aeasy/index.html`,`https://omniweb.gsfc.nasa.gov/form/dx1.html`, and `https://omniweb.gsfc.nasa.gov/form/omni_min.html`. In this work, AE index has been obtained from the last source together with SYM-H and used as modeling input parameters. The two geomagnetic activity indices were considered during modeling for the contribution of both equatorial ring current and auroral zones. It is important to recall that this study comprises of only storm time data which contains both negative and positive storm effects for the period 1996 - 2016 and hence there could be different physical mechanisms involved from different sources.

3.3.4   A, Ap, K, and Kp indices

A three-hour range index, K, was established with the purpose of characterizing the variation in the degree of irregular magnetic activity throughout the day (Bartels *et al.*, 1939). It is derived from the records of three orthogonal field components. The magnetic observatories traditionally measure the variations in the local magnetic coordinate system (H, D, Z) or the geographic coordinate system (X, Y, Z) (Bartels *et al.*, 1939; Bartels, 1957a; Rostoker, 1972). The K index measures the intensity of the solar particle-radiation effects (P-effects) which is strongest near the auroral zones (Bartels, 1957b). Since this is a local index, at every three-hour interval (00:00 - 03:00, 03:00 - 06:00, 06:00 - 09:00, ..., 21:00 - 24:00) a value of K index is assigned for each observatory, thus a total of eight values per day per station. The scale of K index is from 0 to 9. The scales have been adopted so that all stations report the same number of indices 0, 1, 2, ..., 9 for a specific year (Bartels, 1957a). For each observatory, a permanent scale is adopted once for all, giving the limits within the amplitude range R, measured in the unit of force gamma γ (where $1\gamma = 1$ nT). The amplitude range, R, is defined as the difference

between the highest and the lowest deviation within the three-hour interval for each of the three elements (H, D, Z). The value of R is then used to define the K index. R is the range of the disturbance variation in the most disturbed component (Bartels, 1957a). Each observatory has their own scaling, thus conversion table between R and K index, based on the geomagnetic latitude of the station. An example of the conversion from R to K index for the Hermanus geomagnetic observatory is given in Table 3.2 below.

K	0	1	2	3	4	5	6	7	8	9
R (nT)	3	6	12	24	42	72	120	198	300	

Table 3.2: The conversion table from K to R for Hermanus, South Africa

This means all values of R smaller than 3 nT defines K = 0, then R values greater than 3 nT and less than 6 nT defines K = 1, and for all R values greater than 300 nT defines K = 9 for the Hermanus observatory.

The three-hour range planetary K (Kp) index was introduced by Bartels (1949) and gives a global overview of the level of disturbance of geomagnetic activity. The Kp index is derived from the standardized K index (Ks) values from each of 13 geomagnetic observatories by averaging the Ks values at every three-hour interval. Standardization of the K index at each observatory was done because of the very pronounced daily variation encountered, for example, the three-hour intervals close to local midnight tend to be substantially more disturbed than all the other 3-hour intervals during the day. A standardization process was developed accordingly to overcome these difficulties. The resultant index Ks was defined as a continuous variable with limiting values (0o - 9o) rather than the integral K index (0 - 9) which was given in thirds of an integer. Thus typical Ks values comprise only 1/6 of a full interval, with ranges as follows: [0-1/6, 1/6-3/6, 3/6-5/6, 5/6-7/6, ...] which respectively equate to Ks codes [0o, 0+, 1-, 1o, ...] (Bartels, 1949; Rostoker, 1972). The tables of equal distributions of Ks values for each observatory at every three-hour interval of every season is created. For further information regarding the computation of Kp, readers are referred to Bartels (1949) and Rostoker (1972). The K indices are not very sensitive to the ring current variation (Mayaud, 1980).

The K-index is a quasi-logarithmic local index of the 3-hourly range in magnetic activity. For arithmetic manipulations, it is necessary to use an index based on a linear scale rather than quasi-logarithmic scale. The corresponding linear scale of the local K and planetary Kp indices are the three-hour a and ap indices respectively. The Ap index provides a daily average level for geomagnetic activity which is just the sum of eight values of three-hourly ap indices for a particular day. The Kp index in conjunction with Dst index was used in this work for the purpose of storm time selection criteria and obtained from `https://omniweb.gsfc.nasa.gov/form/dx1.html`. Similarly, the local A index is the average over eight three-hourly a index

values for the day. An example using Table 3.3, if the K index values for the day were 3, 4, 6, 5, 3, 2, 2 and 1, the daily A index will be the average of the equivalent amplitudes as follows: A = (15 + 27 + 80 + 48 + 15 + 7 + 7 + 3)/8 = 25.25

K	0	1	2	3	4	5	6	7	8	9
a	0	3	7	15	27	48	80	140	240	400

Table 3.3: Conversion table from K to a index.

The 3-hour K index for Hermanus $(34.4°S, 19.2°E)$ was converted to 3-hour a index using Table 3.3. The Hermanus local A index which is the average of the eight three-hourly a index values together with two other geomagnetic activity indices (SYM-H and AE) were then included in the modeling of storm time $foF2$ response. Local A index is included in the modeling to represent the contribution of the local time effect of geomagnetic conditions.

3.4 Solar activity index: $F_{10.7}$

Solar activity includes active transient and long-lived phenomena on the solar surface, such as solar flares, sunspots, prominences, filament eruptions, coronal mass ejections (CMEs) and high speed streams. Solar activity can lead to strong geomagnetic storms in the magnetosphere and the ionosphere through coupling of solar wind and the Earth's magnetosphere which may disturb radio wave propagation (Davies, 1990; McNamara, 1991). Therefore, the inclusion of the solar activity index in the model development is of paramount importance. Solar activity indices are indicators of the Sun's activity level for a specific period of time. The 10.7 cm solar radio flux along with sunspot number (SSN) are the most widely used indices of solar activity (Davies, 1990; McNamara, 1991; Tapping, 2013). The greatest distinction between the two solar activity indices is that radio flux is a physical quantity whereas SSN is synthetic. Often not measurable in physical units is a synthetic index while physical index has direct measurable values that provides quantifiable physical features of different aspects of solar activity and their effects (Usoskin, 2017). The emphasis for this study will be directed to the physical quantity index.

A measure known as the solar radio flux is used as the basic indicator of solar activity and determines the level of radiation being received from the Sun. The solar flux $(F_{10.7})$ is measured in solar flux units (SFU), where 1 SFU $= 10^{-22}$ W.m^2.Hz. Each value of $F_{10.7}$ measurement is the total amount of radio noise that is emitted at a frequency of 2800 MHz (a wavelength of 10.7 cm) (Tapping, 2013). The $F_{10.7}$ represents the intensity of the extreme ultraviolet (EUV) flux of a specific day. The values of $F_{10.7}$ varies from near 65 during solar minimum up to a maximum of about 200 during the high solar activity period (Davies, 1990). The $F_{10.7}$ measurements are done at the Penticton Radio Observatory in

British Columbia, Canada and are provided courtesy of the National Research Council Canada in partnership with the Natural Resources Canada. The ($F_{10.7}$) index data can be obtained from `https://www.ngdc.noaa.gov/stp/solar/solar-indices.html`.

Analysis of the long-term study by Liu *et al.* (2006) was performed to quantify the solar activity dependence of NmF2. In this study, it was demonstrated that solar activity factor P or $F_{10.7p}$ is a better representation of the solar EUV flux than $F_{10.7}$. Other studies have also reported that $F_{10.7p}$ is a better indicator of the solar activity level than $F_{10.7}$ (e.g. Richards *et al.*, 1994; Liu and Chen, 2009; Chen *et al.*, 2011). For example, Chen *et al.* (2011) examined the $F_{10.7}$ variation with the solar EUV flux and $foF2$ during a deep solar minimum (2007 - 2009). The results showed that $F_{10.7}$ is not an ideal proxy for solar EUV flux and its correlation with $foF2$ drops during deep solar minimum. It was pointed out that this consideration needs to be taken when developing ionospheric models with $F_{10.7}$ as one of the input parameters (Chen *et al.*, 2011). It is on this basis that $F_{10.7p}$ was considered in this study where $F_{10.7}$ data has been used to determine the solar activity factor ($F_{10.7p}$). The $F_{10.7p}$ is obtained by calculating the average of $F_{10.7}$ observed on the day and $F_{10.7A}$ according to the expression: $F_{10.7p} = (F_{10.7} + F_{10.7A})/2$, where $F_{10.7A}$ is the average of $F_{10.7}$ over the previous 81 days (Bergeot *et al.*, 2013; Uwamahoro and Habarulema, 2015).

3.5   Modeling techniques

Ionospheric models can either be theoretically derived from various laws of physics or empirical which is based on observational/measured data. Empirical ionospheric models are not only important for ionospheric research, but also very useful in a wide range of practical applications, e.g. HF radio communication. The artificial neural network (ANN) technique together with regression analysis and polynomial function are used in this study. These modeling techniques are described in this section.

3.5.1   Artificial neural networks (ANNs)

Artificial neural network (ANN), often referred to as neural network (NN) is an information processing system which is, from its inception, driven by performance functions similar to the biological neurons in a human brain (Haykin, 1994). The NN has been developed as a generalization of a mathematical model of human cognition with the following hypothesis: (i) information processing occurs at many simple elements called neurons, (ii) information moves across neurons over connection links, (iii) each connection link has an associated weight, and (iv) each neuron applies an activation function to its net (sum of weighted input information) to determine its output. The main characteristics of NN are connection patterns between the

neurons (called architecture), weight determination method on the connection (training), and activation function (Fausett, 1994; Haykin, 1994).

A neuron is an information processing unit and a key element to the operation of a NN. This unit is connected to other neurons through connection links to allow the flow of information between them. For each connecting link, there is an associated weight. Weights are randomly chosen at the start of the training in order to ensure generalization. A neuron (j) can be described mathematically by the following expressions:

$$u_j = \sum_{i=1}^{n} w_{ji} x_i \qquad (3.51)$$

$$y_j = \varphi(u_j - \theta_j) \qquad (3.52)$$

where x_i represents a set of input signals with the associated weights w_{ji} with $i = 1, 2, 3, ...,n$. The linear combiner output u_j and the threshold θ_j are used within the activation function $\varphi(.)$, also known as the squashing function. The threshold is applied externally with the purpose of lowering the net input of the activation function. The activation function controls the amplitude of the output signal, y_j of the neuron. Figure 3.9 shows an example of input signals fed to the neuron and its output signal for a nonlinear model of a neuron.
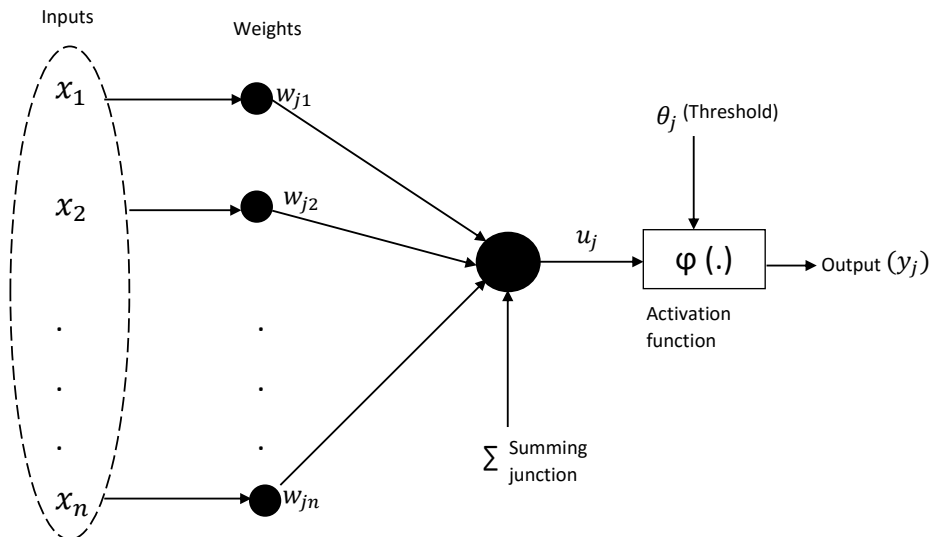
Figure 3.9: An example of a nonlinear model of a neuron (Habarulema, 2010, adopted from Haykin (1994)).

There are different types of neural networks for various applications such as feedforward, recurrent, and stuttgart neural network simulator for example (Elman, 1990; Haykin, 1994; Zell *et al.*, 1994; Medsker and Jain, 1999). The feedforward NN are widely used in pattern recognision problems and are suitable for modeling relationships between a set of predictor variables

and one/more response variables. This technique has been applied in different ionospheric modeling parameters that exhibit non-linear characteristics (e.g. McKinnell and Poole, 2004b; Oyeyemi *et al.*, 2006; Habarulema *et al.*, 2009; Okoh *et al.*, 2019; Otugo *et al.*, 2019). For this study, the multilayer feedforward NN was utilised and is briefly discussed in the next section.

3.5.1.1   Multilayer feedforward network

The classification of NN includes single-layer and multilayer networks, where a single-layer network has only one layer of connection links, or equivalently one layer of neurons which in this case is the output layer. That is, the input is linked directly to the output neurons. A multilayer NN is typically composed of an input layer, one or more hidden layer(s) of which the computational units are called hidden neurons, and an output layer (Fausett, 1994; Haykin, 1994). There is normally a layer of weights between two adjacent levels of units (input, hidden, or output). A multilayer feedforward network is capable of effectively dealing with more complex problems than a single-layer network (Fausett, 1994). For this study, the multilayer feedforward NN with backpropagation algorithm was utilised as one of the modeling techniques investigated, and Figure 3.10 is a schematic illustrative example of such a NN architecture. This network was implemented on the basis of supervised training principles, where a sequence of known input training patterns is presented with the desired system output patterns for the overall network during a training process.

The standard backpropagation is an effective general method of training a multilayer neural network and a widely used algorithm to perform supervised learning (Fausett, 1994; Haykin, 1994). This training method is simply a gradient descent technique that minimizes the total squared error of the output signal. The training of a network by backpropagation includes feedforward input training pattern, the calculation and backpropagation of the associated error, and adjustment of the weights (Fausett, 1994).

In the backpropagation algorithm, the initialization of weight is performed randomly with the limits $-1 \leq w \leq 1$. The feedforward process within the algorithm is when each input neuron receives an input signal (training pattern) and forwards this pattern to all neurons in the hidden layer. Each hidden neuron sums its weighted input patterns. The hidden neuron computes its input pattern using its activation function and forwards it to all neurons in the output layer. Each output neuron then sums its weighted input patterns and applies its activation function to compute its output pattern which then concludes the feedforward process of the training network. During the backpropagation of error process, each output neuron receives a target pattern corresponding to the input training pattern and calculates its error information term, computes its weight and bias correction terms, and then gets sent to neurons in the hidden layer. Each hidden neuron does the summation of its error information input

term. Each output and hidden neurons update its weight and bias. There are available detail descriptions of the backpropagation algorithm (Fausett, 1994; Haykin, 1994).

3.5.1.2   Architecture for NN

NN architecture represents the arrangement of neurons or nodes into the layers and the connection patterns between layers, activation functions, and learning methods. The model and the architecture of NN determine how a network mutates its input into an output data. The number of layers within a NN architecture can be obtained by just adding up the layers of connection links contained in that same network, this excludes the layer of input neurons because it does not perform any computation (Fausett, 1994).
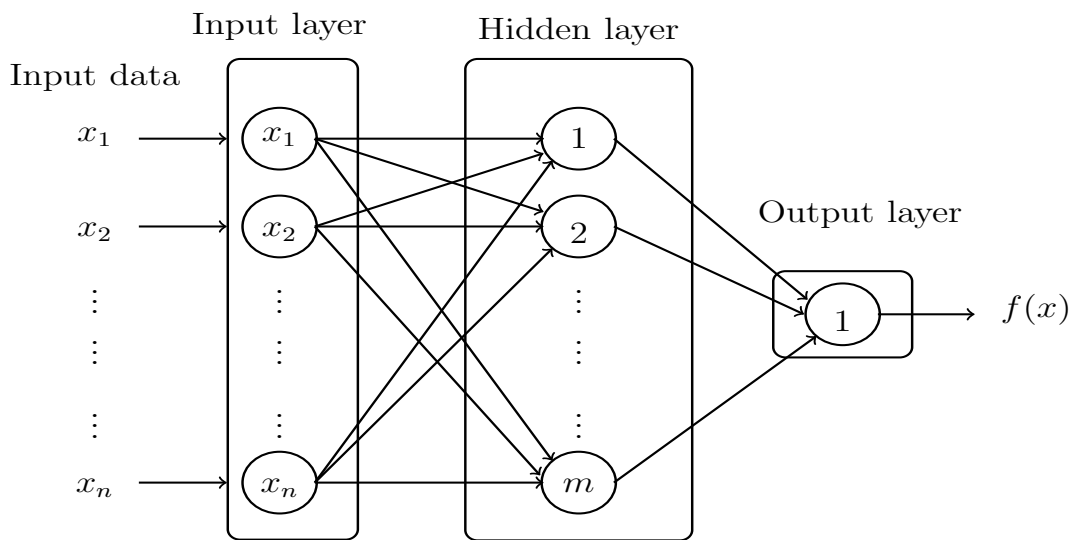
Figure 3.10: A schematic illustration of a multilayer feedforward NN architecture.

Figure 3.10 is an illustrative example of a NN architecture for a multilayer feedforward network which is the NN method considered in this work. It can be seen that during a feedforward process, each input unit $(x_1, x_2, ..., x_n)$ receives an input data/signal and transmits this signal to each of the hidden units $(1, 2, ..., m)$. Each hidden unit does the computation and sends the signal to the output unit to form the response variable, $f(x)$ in this case. In summary the network consist of n input neurons, one hidden layer with a total of m hidden neurons, and one output $f(x)$.

3.5.2   Regression analysis

Regression analysis, one of the oldest methods in the area of mathematical statistics, is a statistical method for investigating the relationship between a dependent variable (also known as a response variable) and one or more independent/predictor variables. In addition to establishing a relationship between dependent and independent variables, regression analysis includes the

prediction of a response variable based on a set of independent variables and also determines which independent variable contributes more than others to the response of dependent variable (Yan and Su, 2009). The mathematical regression analysis model that relates a dependent variable Y and an independent variable X is given by:

$$Y \approx f(X, \beta) \tag{3.53}$$

where β represents a set of unknown parameters called coefficients and are determined from a set of data using statistical methods (Chatterjee and Hadi, 2006). $f(X, \beta)$ is a function representing the mathematical expectation of the response variable. This regression function is called linear if the response variable is a linear combination of the independent variables ($X = x_1, x_2, ..., x_k$), otherwise is termed nonlinear (Chatterjee and Hadi, 2006; Yan and Su, 2009). The number of independent variables within the regression function is denoted by k. The three basic types of regression analysis are: (i) simple linear regression, (ii) multiple linear regression, and (iii) nonlinear regression. If the number of independent variables $k = 1$, then the function in Equation 3.55 is a simple linear regression model which can be expressed mathematically as follows:

$$y = \beta_0 + \beta_1 x + \varepsilon \tag{3.54}$$

where y is the dependent variable, β_0 is the y intercept, and β_1 is the slope of the simple linear line between x and y. The independent variable is denoted by x and ε is the random error. The random error, also known as residual, can be obtained by computing the difference between the measured value y of the dependent variable and the estimated value $\tilde{y}$, $\varepsilon = y - \tilde{y}$ (Cook and Weisberg, 1982; Rawlings *et al.*, 1988; Seber and Lee, 2003). Thus, the simple linear regression can be used to model a linear relationship between two variables, x and y. The difference between simple and multiple linear regression is determined by the number of independent variables (Chatterjee and Hadi, 2006; Yan and Su, 2009). The multiple linear regression model relates one dependent variable to several independent variables and is indicated by:

$$y = \beta_0 + \beta_1 x_1 + \beta_2 x_2 + ... + \beta_k x_k + \varepsilon \tag{3.55}$$

where regression coefficients are represented by $\beta_0, \beta_1, \beta_2, ..., \beta_k$. In the case where the relationship between the dependent variable and independent variables is not linear in regression parameters, a nonlinear regression model is presented. A typical example of such a model is

$$y = \frac{\alpha}{1 + e^{\beta x}} + \varepsilon \tag{3.56}$$

where α and β are the unknown regression parameters of the model which are estimated from a set of data. The unknown regression parameters can be obtained by a parameter estimation or model fitting method from a dataset (Mitchell and Beauchamp, 1988; Shen, 2000; Chatterjee

and Hadi, 2006). The most commonly used method of estimation was adopted in this study and is called the least squares method. The multiple linear regression model has been applied in this work to predict the response variable ($\Delta foF2$) based on the set of independent variables including solar and geomagnetic activity indices.

3.5.3   Polynomial functions

A polynomial is a mathematical expression constructed with coefficients and variables using the operations of addition, subtraction, multiplication, and non-negative integer exponents of variables. Polynomials appear in many areas of mathematics and science, and can be used to form polynomial equations or define polynomial functions. A polynomial function is a function that can be defined by evaluating a polynomial. A polynomial of degree n is a function of the form:

$$f(x) = \sum_{i=0}^{n} a_i x^i \qquad \text{or}$$

$$f(x) = a_0 + a_1 x + a_2 x^2 + ... + a_n x^n$$

(3.57)

where $f(x)$ is a polynomial function of a single variable x and $a_0, a_1, a_2, ..., a_n$ are called the polynomial coefficients (Leung *et al.*, 1992; Irving, 2003). The term a_0 has the exponent of 0 and is known as the constant term. The term $a_n x^n$ is called the leading term with its leading coefficients and the degree of this term is named the degree of polynomial (Leung *et al.*, 1992). If the degree of polynomial is 0, 1, 2, and 3 then the polynomials would respectively be named as constant, linear, quadratic and cubic functions (Leung *et al.*, 1992). An example of a cubic function can be written as follows:

$$f(x) = a_0 + a_1 x + a_2 x^2 + a_3 x^3$$

(3.58)

The easiest polynomial functions to solve, are those with the lowest degrees (Irving, 2003). It is important to highlight the fact that the coefficients a_i (for $i = 0, 1, 2, ..., n$) of a polynomial function are real numbers. Therefore, $f(x)$ is a polynomial in x with real coefficients or coefficients in R (Leung *et al.*, 1992), where R indicates that the coefficients are taken from the set of real numbers (Leung *et al.*, 1992; Irving, 2003). The simple structure of polynomial functions makes them a powerful tool in analyzing general functions using polynomial approximations. In this study the polynomial function is applied as a fitting tool to relate $foF2$ and TEC at similar or nearby locations. These relationships are then used to derive $foF2$ at GPS receiver locations that fall within the IPP coverage by considering elevation angles of 40 degrees over

the ionosonde locations.
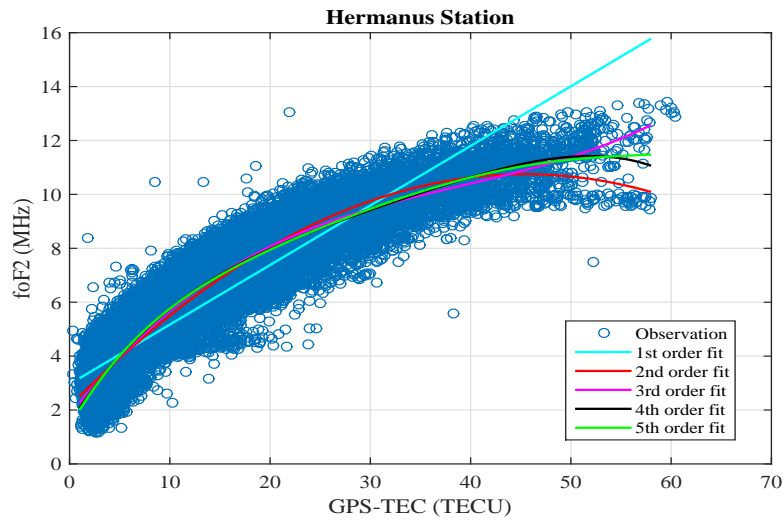
Figure 3.11: A graph representing $foF2$ in MHz versus GPS TEC in TECU with polynomial fitting up to 5th degree order over Hermanus from 2009-2017.

As an example, Figure 3.11 represents the $foF2$ versus GPS TEC measured respectively in MHz and TECU with polynomial fitting of first up to fifth degree. In this figure, the 1st, 2nd, 3rd, ... order fits represent linear, quadratic, cubic, ... functions respectively. The polynomial fitting was done to evaluate the polynomial function that best fits the data.

3.6   Summary

This chapter provided details of the data sources utilised in the study with the focus on $foF2$ measurements from the South African ionosonde stations and TEC measurements from GNSS receivers. An overview of geomagnetic and solar activity indices considered in this work was described. The modeling inputs as well as different modeling techniques considered for storm-time $foF2$ data were discussed. In the following chapter, results based on NNs and multiple linear regression techniques are presented.

Chapter 4

Single station modeling of storm time $foF2$ response

4.1 Introduction

This chapter discusses single station modeling of ionospheric critical frequency of the F2 layer ($foF2$) response to geomagnetic storms. The station considered for this analysis is Grahamstown ($33.3°S, 26.5°E$), South Africa using ionosonde $foF2$ measurements from 1996 - 2014. This station was chosen because of its advantage in having the longest dataset compared to the other three South African ionosonde stations. The neural network (NN) and linear regression (LR) modeling techniques are used in this study. The dataset for the development of the models was based on only disturbed days. The analysis and performance of both NN and LR techniques were tested for storm periods which were not included in the model development. Most of the results discussed in this chapter were published in a paper by Tshisaphungo *et al.* (2018).

4.2 Data and Modeling Techniques

4.2.1 Data processing

The $foF2$ measurements from the Grahamstown ionosonde were available with different time resolutions of 1 hour, 30- and 15-minutes data. The percentage of data for different time resolutions are approximately 7% (1996-1999), 37% (2000-2005), and 56% (2005-2014) for 1 hour, 30- and 15-minutes respectively. The top panel, in Figure 4.1(a) shows the number of geomagnetic storms observed over the period 1996-2014 with the smoothed monthly sunspot number indicating the degree of solar activity. As seen from Figure 4.1(a), the data covers the entire solar cycle 23 and half of solar cycle 24. The bottom panel, Figure 4.1(b) is the $foF2$ measurements for the same period. These data are only for the periods of geomagnetic storm

occurrences, hence the large data gaps observed, especially during solar minimum period. The dataset is a combination of two or one day before and after the storms' onset and recovery phase respectively depending on the time of occurrence. The criterion for selecting the periods of geomagnetic storm occurrences was based on $Dst \leq -50$ nT (Kamide *et al.*, 1998b; Vijaya Lekshmi *et al.*, 2011).
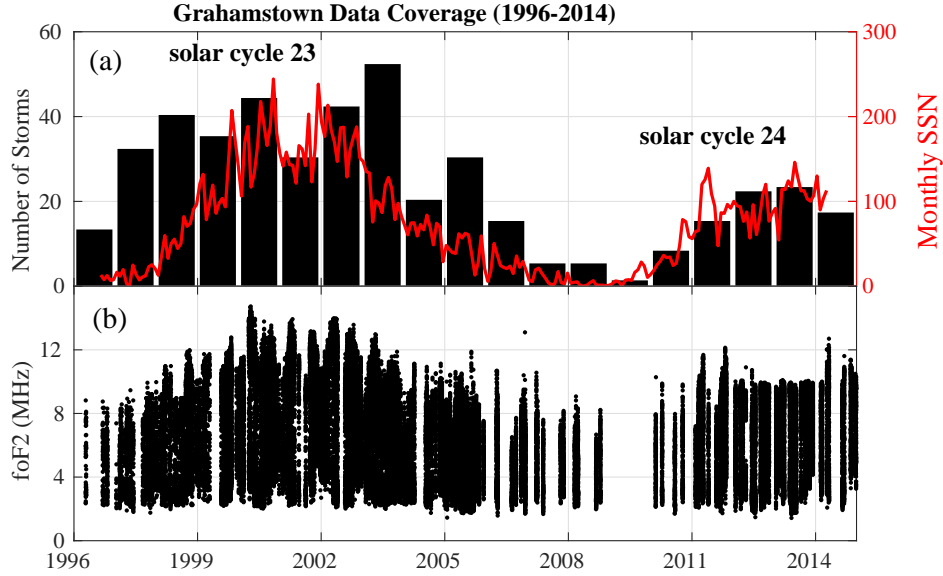
Figure 4.1: (a) Number of geomagnetic storms observed in black bars per year for the period 1996-2014. The red line represents the smoothed monthly sunspot number indicating the degree of solar activity, (b) Represents storm time dataset of $foF2$ (MHz) in black dots, showing the ionospheric data availability during a period 1996-2014.

Since the primary purpose of this work is to develop a model that can capture ionospheric storm effects during geomagnetic storms, the deviation of daily $foF2$ from the respective monthly median values ($\Delta foF2$) has been calculated using the following expression:

$$\Delta foF2 = \left(\frac{foF2 - foF2_m}{foF2_m} \right) \times 100 \tag{4.1}$$

where $foF2_m$ is the monthly median of $foF2$ values in MHz. $\Delta foF2$ in Equation 6.1 is used to define the quiet time ionospheric variability between ± 20 % as applied in other studies (Danilov, 2001; Gao *et al.*, 2008; Matamba *et al.*, 2015). The $foF2_m$ includes both quiet and disturbed days with data for the whole month.

The accurate modeling of the ionospheric storm time $\Delta foF2$ requires a good understanding of the physical driver mechanisms. The solar activity variation is one of the drivers for ionospheric variability. The solar radio flux at 10.7 cm (2.8 GHz frequency) ($F_{10.7}$) index is a well

known indicator of solar activity (Davies, 1990; McNamara, 1991; Tapping, 2013) and was considered in this work as one of the input parameters in modeling. The $F_{10.7}$ index data was downloaded from `https://www.ngdc.noaa.gov/stp/solar/solar-indices.html`. $F_{10.7}$ index has been used to calculate the solar proxy index, $F_{10.7p}$, which is a better indicator of solar activity than $F_{10.7}$ (e.g. Chen *et al.*, 2006; Liu and Chen, 2009). The $F_{10.7p}$ is obtained by computing the average of $F_{10.7}$ observed on the day and $F_{10.7A}$ according to the expression: $F_{10.7p} = (F_{10.7} + F_{10.7A})/2$, where $F_{10.7A}$ is the average of $F_{10.7}$ over the previous 81 days (Liu and Chen, 2009; Bergeot *et al.*, 2013; Uwamahoro and Habarulema, 2015).

Geomagnetic storms have significant impact in the ionosphere, hence geomagnetic activity indices are a crucial part of ionospheric modeling. In this study, three geomagnetic activity indices are considered for modeling: (i) the symmetric disturbance field in the horizontal (H) component of the Earth's magnetic field ($SYM - H$), (ii) the Auroral Electrojet (AE) index, and (iii) the local geomagnetic A index. Considering the existence of a large storm time dataset driven by different processes, more than one geomagnetic activity indicator was considered in this modeling attempt. $SYM - H$ is a geomagnetic activity index related to the equatorial ring current (Saba *et al.*, 1997) and is mainly associated with coronal mass ejection (CME) driven storms (Huttunen *et al.*, 2002). $SYM - H$ was chosen instead of the Dst index because of its advantage of having higher time resolution (1-minute) data as compared to hourly Dst index data (e.g., Wanliss and Showalter, 2006; Li *et al.*, 2011). Also, the effect of solar wind dynamic pressure variation is more pronounced in $SYM - H$ than hourly Dst-index as reported by e.g., Wanliss and Showalter (2006). The AE index is designed to provide a global, quantitative measure of auroral zone magnetic activity produced by enhanced ionospheric currents flowing below and within the auroral oval (e.g., Davis and Sugiura, 1966; Kamide and Akasofu, 1983). AE index is useful in studying the morphology of ionospheric effects during storms/sub-storms. $SYM - H$ and AE index data were obtained from `http://wdc.kugi.kyoto-u.ac.jp/aeasy/index.html`. The local geomagnetic A index was used to account for the local geomagnetic effect since the focus is on single station modeling. The K-index data for the Hermanus, South Africa ($34.4°S, 19.2°E$) station was used to obtain the A index data using the K-index conversion in Table 4.1.

K	0	1	2	3	4	5	6	7	8	9
a	0	3	7	15	27	48	80	140	240	400

Table 4.1: The table illustrates the conversion between geomagnetic K and A index values

4.2.2 Neural networks model construction

In this study, a feed forward neural network (NN) with backpropagation (Levenberg-Marquardt) algorithm was used (Hagan *et al.*, 1996; Yu and Wilamowski, 2011). The Levenberg-Marquardt

backpropagation algorithm has the advantage of minimum training time (Hagan *et al.*, 1996; Habarulema and McKinnell, 2012; Uwamahoro and Habarulema, 2015). The sigmoid transfer function was used during the NN training because it is differentiable and thus allows the computation of gradient necessary for training through backpropagation (Hagan *et al.*, 1996; Yu and Wilamowski, 2011). For this purpose, the NN is used to model the storm-time ionospheric $foF2$ response, $\Delta foF2$, as a function of time of the day (hr), day number of the year (dn), representing diurnal and seasonal variations respectively, solar ($F_{10.7p}$), and geomagnetic activity indices ($SYM - H$, AE, and local A). The $F_{10.7p}$ index represents solar activity while possible different processes induced in the ionosphere during solar wind-magnetosphere-ionosphere coupling are taken into account by including $SYM - H$ and AE indices. Contribution for local geomagnetic response is represented by A index. To avoid unrealistic numerical discontinuity, cosine and sine components are introduced for the time of the day (hr) and day number of the year (dn) input parameters during the training as previously applied by McKinnell and Poole (2004b); Oyeyemi *et al.* (2006); Habarulema *et al.* (2009) as follows:

$$dnc = cos\left(\frac{2\pi \times dn}{365.25}\right) \qquad dns = sin\left(\frac{2\pi \times dn}{365.25}\right) \qquad (4.2)$$

$$dnca = cos\left(\frac{4\pi \times dn}{365.25}\right) \qquad dnsa = sin\left(\frac{4\pi \times dn}{365.25}\right) \qquad (4.3)$$

$$hrc = cos\left(\frac{2\pi \times hr}{24}\right) \qquad hrs = sin\left(\frac{2\pi \times hr}{24}\right) \qquad (4.4)$$

where dnc, dns, hrc, hrs are the cosine and sine components of dn and hr respectively. In Equation 4.3, $dnca$ and $dnsa$ are the cosine and sine of day number representing semi-annual variations. The number of hidden nodes in the hidden layer was obtained based on the root-mean-square error (RMSE) values between the derived and predicted $\Delta foF2$ output. The RMSE was calculated using an expression below:

$$\text{RMSE} = \sqrt{\frac{1}{N}\sum_{i=1}^{N}(\Delta foF2_{NN} - \Delta foF2_{derived})^2} \qquad (4.5)$$

where $\Delta foF2_{NN}$ and $\Delta foF2_{derived}$ is the NN modeled and derived $\Delta foF2$ respectively over a number of sample size data, N. In order to determine the optimum NN model, several models were developed by varying the number of hidden nodes and calculating the RMSE values between the modeled and the derived $\Delta foF2$ using Equation 4.5. The storm periods reserved for validations (excluded from training set) are: 2-7 October 2000, 5-8 November 2001, 28 October-1 November 2003, and 6-12 November 2004. Figure 4.2 shows the RMSE values (%) against the number of hidden nodes. Initial number of hidden nodes is 10, which is equal to

the number of input parameters used in the model. The optimum solution was reached using 13 hidden nodes which gave the lowest RMSE value. For this application, the optimum NN architecture was 10:13:1 which is defined based on the 10 input variables, 1 output ($\Delta foF2$) variable and 13 hidden nodes chosen based on the lowest RMSE method that has been used in previous ionospheric modeling studies (McKinnell and Poole, 2004b; Habarulema *et al.*, 2009; Uwamahoro and Habarulema, 2015).
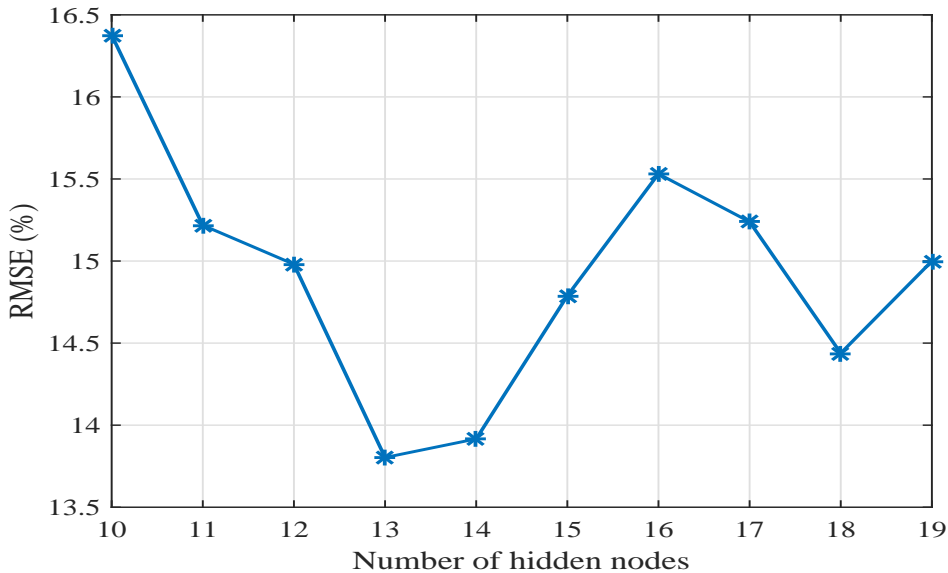
Figure 4.2: Root-mean-square error (RMSE) values between the derived and the NN modeled $\Delta foF2$ with corresponding number of hidden nodes for all storms used in model validation.

It is important to note that in this model, three geomagnetic indices were used which are $SYM - H$, AE, and local A indices. As mentioned in section 4.2.1, this is to account for the ring current contribution from the magnetosphere (e.g., Li *et al.*, 2011), the energy transport related processes from the auroral zones to mid- and low-latitudes ionosphere during storms/sub-storms (e.g., Davis and Sugiura, 1966; Akasofu, 1981), and local contribution of the geomagnetic disturbance respectively. In order to assess the contribution of each magnetic index, $SYM - H$, AE, and local A were separately added to the primary input parameters (PIP) (dn, hr, and $F_{10.7p}$). The NN training for the PIP was done followed by calculating the RMSE values between the modeled and actual $\Delta foF2$. The RMSE values (%) are presented in the top panel of Figure 4.3(a). Similar training was performed and RMSE obtained for the PIP with $SYM - H$, AE, and local A separately as well as the three geomagnetic indices combined. Figure 4.3(a) shows all the RMSE values (%) for the NN training of different input parameters, and Figure 4.3(b) is the contribution of each geomagnetic indices to modeling which was calculated using Equation 4.6.

$$contribution = \left(\frac{RMSE_{PIP} - RMSE_{GMI}}{RMSE_{GMI}} \right) \times 100 \qquad (4.6)$$

where $RMSE_{PIP}$ and $RMSE_{GMI}$ are the RMSE values for PIP and geomagnetic indices respectively. The largest contributing index is $SYM - H$ ($\simeq 41\%$), which means that it is the most important geomagnetic parameter used in modeling. AE, and local A indices lead to improvements of $\simeq 2\%$ and 11% respectively. A combination of all three geomagnetic indices to PIP shows an overall improvement of $\simeq 42\%$ based on the NN technique. The same analysis using linear regression yields similar results with the $SYM - H$ index providing higher improvement of 54% compared to 7% and 26% for AE, and local A indices respectively.
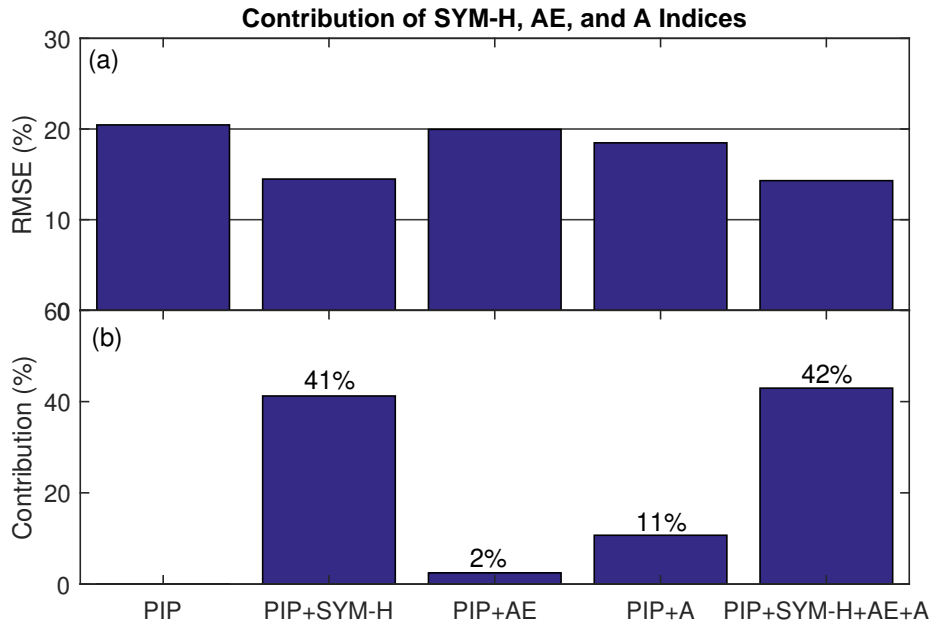
Figure 4.3: Root-mean-square error (RMSE) values (%) and the percentage contribution of the geomagnetic activity indices used in modeling.

One of the challenges when developing an ionospheric storm index is the choice of the appropriate representation of geomagnetic conditions (e.g., Fuller-Rowell *et al.*, 2000a; Pietrella and Perrone, 2008). In most cases, the choice of geomagnetic index is based on the intended temporal resolution for the developed ionospheric model. For example, Pietrella and Perrone (2008) used effective planetary geomagnetic index a_p in the local ionospheric storm model to forecast hourly $foF2$. The STORM model which is incorporated within the IRI model also uses an index analogous to the effective a_p index (Araujo-Pradere *et al.*, 2002; Araujo-Pradere and Fuller-Rowell, 2002). In this paper, high resolution geomagnetic indices, $SYM - H$ and AE, were investigated together with local A index in the modeling. A possibility of including

effective a_p index will be explored in future for possible improvement of the model.

4.2.3 Linear regression

Linear regression is a statistical method used to study the relationship between predictor and response variables. Regression methods have been used extensively in the past to model the ionospheric dependence on solar and geomagnetic activity (e.g., Zolesi *et al.*, 1993, 1996; Liu *et al.*, 2004; Laštovička *et al.*, 2006; Yue *et al.*, 2006). In this chapter, the predictor variables also known as independent variables are hr, dn, $F_{10.7p}$, $SYM - H$, AE, and local A as defined in section 4.2.2 and the response variable is $\Delta foF2$. The linear regression model to describe the relationship between the predictor and the response variables is as follows:

$$\Delta foF2 = f_1 + f_2 + f_3 \tag{4.7}$$

where f_1, f_2, and f_3 are defined as:

$$f_1 = a_1 + a_2 \times hrc + a_3 \times hrs + a_4 \times F10.7_p + a_5 \times symH + a_6 \times AE + a_7 \times A \tag{4.8}$$

$$f_2 = f_1 \times (b_1 \times dnc + b_2 \times dns) \tag{4.9}$$

$$f_3 = f_1 \times (c_1 \times dnca + c_2 \times dnsa) \tag{4.10}$$

where f_2 and f_3 correspond to annual and semi-annual variation components. Constants $a_1, a_2, ...a_7, b_1, b_2, c_1$, and c_2 are determined using least squares approach. Zhang *et al.* (2011) have shown that the model can reproduce quite well the original data based on these functions which represent the annual and semi-annual variations of foF2 data. Equation 4.9 shows $\Delta foF2$ dependency on seasonal (annual) variation represented by changes in day number of the year. Here it should be noted that f_2 in Equation 4.9 is a function of Equation 4.8 which has 7 coefficients. Since Equation 4.9 is a summation of cosine and sine components of day number of the year, it contains 14 coefficients. Similarly, Equation 4.10 which is a function of Equation 4.8 takes into account $\Delta foF2$ variations with respect to semi-annual changes, and also has 14 coefficients. Therefore, Equation 4.7 which is a combination of Equations 4.8 - 4.10, consists of a total of 35 coefficients which were used in testing the linear regression model's performance.

4.3 Results and discussion

This section describes the results of the NN and LR predicted $\Delta foF2$ in comparison with the derived $\Delta foF2$ for a number of selected geomagnetic storms. In consideration of the geomagnetic storms being presented, four interpolation (within 1996-2014) and two extrapolation (beyond 2014) storms were selected for validation. The dataset used to validate both NN and LR models was not used in the models' development. This makes the testing storm data independent when assessing the level of model performance.

4.3.1 Interpolation storms

Figure 4.4 shows the performance of NN and LR models during the four storm periods selected within the time period of models' development. These storm periods are thus referred to as "interpolation" storms. Figures 4.4(a) and 4.4(b) represent geomagnetic storms which occurred during maximum period of solar cycle 23 while Figures 4.4(c) and 4.4(d) show validation results for storms which occurred during the declining phase of the solar cycle. In each graph of Figure 4.4, Dst index is plotted on the top panel to represent the storm occurrence date and time, and its magnitude. The bottom panel is the derived $\Delta foF2$ (%) plotted in black dots and modeled $\Delta foF2$ (%) by means of NN (blue) and LR (red) methods respectively. The minimum Dst values reached in Figures 4.4(a) - (d) are -182 nT, -292 nT, -383 nT, and -374 nT respectively. According to Loewe and Prölss (1997), these storms are classified as strong, severe, and two great (storm periods) respectively.

Figure 4.4(a) represents a storm period during 2-7 October 2000. During this period, multiple peaks of minimum Dst index values of -143 nT (04 October at ∼20:00 UT), -175 nT (05 October 2000 at ∼07:00 UT), and -182 nT (at 13:00 UT on 05 October) are observed. According to Zhang *et al.* (2007) and Xystouris *et al.* (2014), the cause of this storm was a CME with unknown source or flare generated stream. In Figure 4.4(a), Dst index does not present a sudden increase known as the sudden storm commencement (SSC) which is a common feature for most CME-driven storms (Borovsky and Denton, 2006; Gopalswamy, 2009). A negative ionospheric response is observed starting at ∼19:00 UT on 4 October 2000 with $\Delta foF2$ values going below -20%. The decrease in $\Delta foF2$ is observed throughout the day on 5 until 6 October 2000 at ∼09:00 UT when $\Delta foF2$ values returned to quiet time variability threshold. In terms of the trend, both NN and LR seem to be following the ionospheric response observed. LR model is mostly within the quiet time variability threshold whereas the NN is successful in capturing most of the negative response observed.

Figure 4.4(b) shows a storm period during 5-8 November 2001 with minimum Dst index of -292 nT observed on 6 November 2001 at ∼06:00 UT. The main phase of the geomagnetic storm is observed with a decrease of Dst index values from ∼18:00 UT on 5 November to 6 November 2001 at 06:00 UT. This was a CME-driven storm associated with an X1.0 solar flare (Zhang

et al., 2007) and classified as severe storm according to Loewe and Prölss (1997). A precursor interplanetary electric field and a concomitant moderate storm occurring prior to the shock electric field event has been reported by Tsurutani *et al.* (2004). Other studies have analyzed different aspects of this storm (Maruyama *et al.*, 2004; Tsurutani *et al.*, 2004; Horvath and Lovell, 2008; Kikuchi *et al.*, 2008; Sojka *et al.*, 2012). For example, Maruyama *et al.* (2004) presented the daytime TEC enhancement on the 6 November which was associated with the prompt penetrating eastward electric field. A negative ionospheric response is observed on 6 November 2001 starting at ∼03:00 UT with $\Delta foF2$ values decreasing to ∼60%. This transpires after the intense, negative interplanetary magnetic field (IMF) Bz event (at ∼01:54 to ∼04:00 UT) which is the cause of the geomagnetic storm's main phase (Tsurutani *et al.*, 2004). The $\Delta foF2$ remained below -20% for most of the day on 6 November 2001 and continues until 7 November 2001 at ∼06:50 UT. The ionospheric response recovered to quiet time variability with $\Delta foF2$ above -20% threshold, as seen from Figure 4.4(b) on 7 November 2001. The ionospheric response to this geomagnetic storm lasted for only less than $1\frac{1}{2}$ days over the Grahamstown station. Both NN and LR models were accurate in capturing almost the entire negative ionospheric response during this period, although the LR model predicts stronger negative $\Delta foF2$ values compared to NN model.
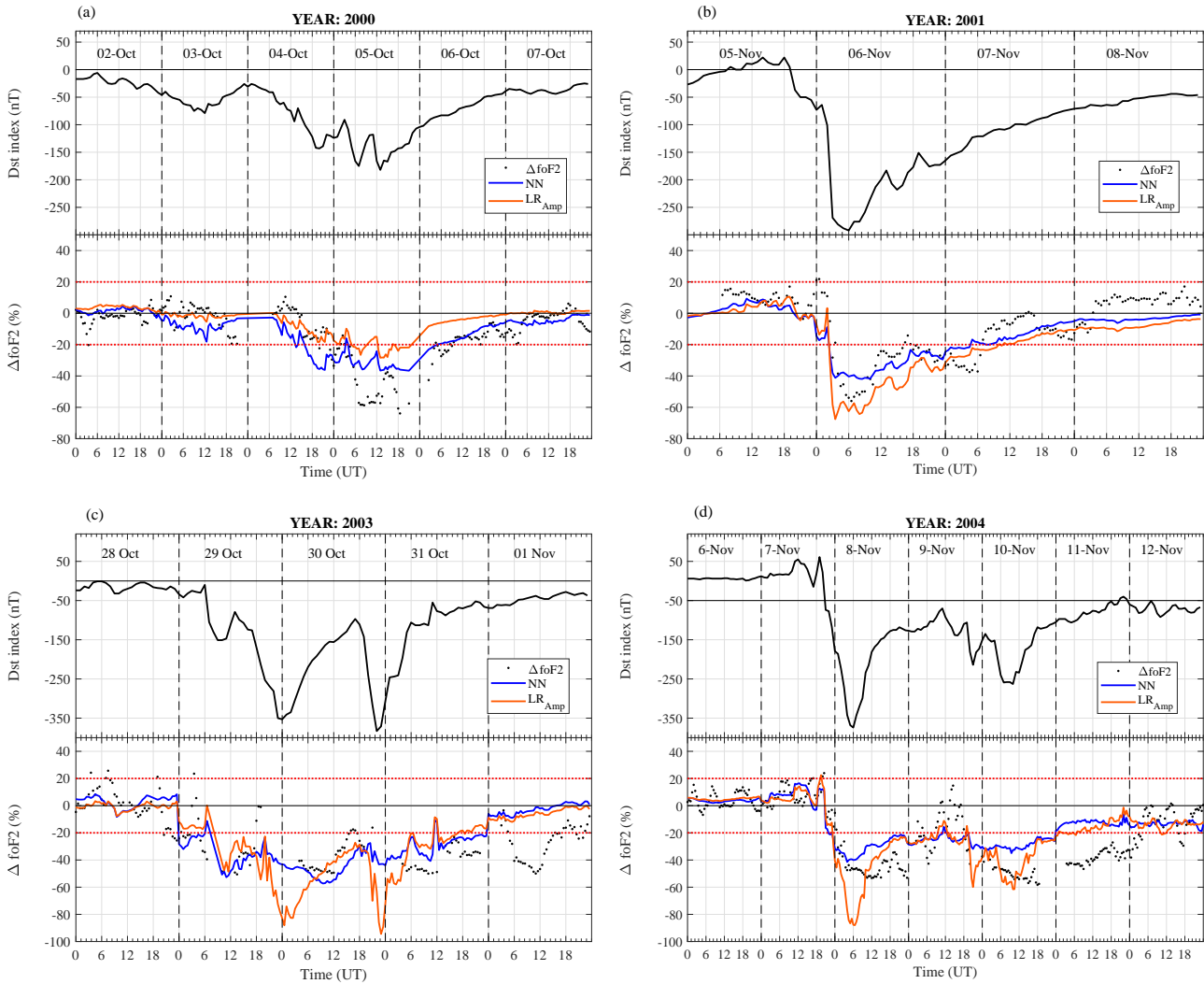
Figure 4.4: Derived and modeled $\Delta foF2$ (%) for four selected validation storm periods: (a) 2-7 October 2000, (b) 5-8 November 2001, (c) 28 October-1 November 2003, and (d) 6-12 November 2004. In each graph, Dst index is plotted on the top panel to represent the storm occurrence date and time, and its magnitude. The bottom panel is the derived $\Delta foF2$ (%) plotted in black dots and modeled $\Delta foF2$ (%) by means of NN (blue) and LR (red) techniques respectively

Figure 4.4(c) shows the Halloween storm period which occurred between 28 October - 01 November 2003. There are three successive storm main phases during this period with minimum Dst index values of -151 nT ($\sim$10:00UT) on 29 October, -353 nT ($\sim$00:00 UT) and -383 nT ($\sim$22:00 UT) on 30 October 2003. The third storm was the most intense and commenced around 18:00 UT during the recovery phase of the first storm. On 28 October 2003, an X17 solar flare was observed and associated with a CME which caused a geomagnetic storm on 30 October 2003 (Skoug *et al.*, 2004; Tsurutani *et al.*, 2005; Mannucci *et al.*, 2005; Tsurutani *et al.*, 2006). A negative ionospheric response was observed from 29 October until 01 November 2003. Both NN and LR models are able to follow most of the negative ionospheric responses during this period as seen from Figure 4.4(c) with LR underestimating the deviation magnitude. On 01 November 2003 both models were not able to capture the response. The LR model predicts stronger neg-

ative phases (at ∼00:00 UT and 23:00 UT) on 30 October 2003. On the 28 October 2003, the ionosphere experienced the effect (TEC enhancement) of the strongest solar flare ever observed on 28 October 2003 at ∼11:08 UT (Tsurutani *et al.*, 2005, 2006; Matamba *et al.*, 2016). This effect is not seen as significant on the $foF2$ data over the Grahamstown station, as seen in Figure 4.4(c), where $\Delta foF2$ (%) values remained mostly within quiet time variability on 28 October 2003. However, a pre-storm enhancement in maximum electron density around midday on 28 October 2003 over Chilton ($51.6°N, 358.7°E$) station has been reported by Burešová and Laštovička (2007). Short-duration positive enhancements are observed at ∼07:00 UT (before the extreme solar flare) and around ∼19:00 UT (after the solar flare). Similar ionospheric enhancement at ∼19:00 UT on TEC data is also noted in previous studies (e.g., Mannucci *et al.*, 2005; Tsurutani *et al.*, 2006).

Difficulties in modeling the ionospheric response during storm period of 28 October -01 November 2003 period have been reported (e.g., Habarulema *et al.*, 2010; Ercha *et al.*, 2012; Uwamahoro and Habarulema, 2015). These studies used NN (Habarulema *et al.*, 2010; Uwamahoro and Habarulema, 2015) and empirical orthogonal functions (Ercha *et al.*, 2012; Uwamahoro and Habarulema, 2015) to model the ionospheric TEC response and were unsuccessful in accurately capturing the magnitude of TEC during the negative storm effect on 30 October 2003. However the trend of the TEC response was captured (e.g., Habarulema *et al.*, 2010). In Figure 4(c) the negative ionospheric effect lasted for about 3 days and 18 hours. Despite the underestimation by the LR model, results in Figure 4(c) show that these models are capable of reconstructing 80% of the trend of the negative storm effect which is significant.

Figure 4.4(d) shows a CME driven geomagnetic storm period during 7 - 12 November 2004. This storm period is known as one of the most complex geomagnetic storms and has been analyzed in detail (Tsurutani *et al.*, 2008b; Echer *et al.*, 2010). Tsurutani *et al.* (2008b) looked at the solar and interplanetary complex structures on day 7 to 8 November 2004 of this storm period, which resulted in a superstorm event. They found that this superstorm was associated with three distinct fast forward shocks, three directional discontinuities and two reverse waves. The southwardly directed magnetic field within the magnetic cloud was the main cause of the superstorm. Echer *et al.* (2010) analyzed two large geomagnetic storms which occurred on 8 and 10 November 2004. These storms were a result of multiple flares associated with many CMEs from active region 10696 (AR10696). Three fast forward shocks were observed before the storm main phase which lasted for ∼11 hours on 8 November 2004. Other studies have also looked at a sequence of such geomagnetic storms and their impact on different latitude regions (Fejer *et al.*, 2007; Habarulema *et al.*, 2013).

A minimum Dst index of -374 nT (at ∼ 06:00 UT on 8 November 2004) for the first storm and -263 nT (at ∼ 10:00 UT on 10 November 2004) for the subsequent storm were observed. The effect of the first storm resulted in a strong negative storm effect on 8 November 2004

that lasted the whole day. On 9 November 2004 during the recovery phase of the first storm, the measured ionospheric $\Delta foF2$ was within the quiet time variability during daytime before experiencing another decrease later on the same day. The recovery of the second ionospheric response was a steady process which persisted for more than two days. Both NN and LR successfully captured most of the ionospheric response for 08 - 10 November 2004 storm. On 09 November 2004 during the time of observing ionospheric $\Delta foF2$ quiet conditions, the NN and LR models tried to also represent well the recovery of the ionospheric response before another strong negative ionospheric response occurs. For the second storm, both NN and LR models were successful in following the negative storm phase during the main-phase on 10 November 2004. The negative storm effect during the recovery is not modeled accurately by either model. Generally, with exception of 11 November 2004, both NN and LR models reproduced the trend of the negative storm effect during 8-10 November 2004, with one instance on 09 November where both models predicted a recovery when there were depleted foF2 values. According to Tsurutani *et al.* (2008b) and Echer *et al.* (2010), this is an example of a sophisticated magnetic storm with multiple flares and CMEs observed. Despite the fact that this storm period was influenced by one of most complex interplanetary structures as discussed extensively in Tsurutani *et al.* (2008b), both NN and LR models partly represent well the ionospheric response.

4.3.2 Extrapolation storms

Figure 4.5 shows two validation storms outside the period of the models' development (extrapolation storms). These storms occurred during the periods of 16 - 21 March 2015 and 19 - 23 December 2015. The minimum Dst index of -223 nT (at ~22:00 UT) on 17 March 2015 was observed, see Figure 4.5(a). The storm period results from a CME associated with solar flare and several type II/IV radio bursts (Wu *et al.*, 2016). A sudden increase of Dst index is evident at ~04:00 UT indicating the onset of the storm. On 17 March 2015, positive enhancements of ionospheric $\Delta foF2$ are observed (~11:00 and ~17:45 UT) during the storm's main phase occurrence (~ 05:00 - 22:00 UT). Similar observation over the African sector based on TEC data has been reported by Astafyeva *et al.* (2015) and Nava *et al.* (2016). A negative ionospheric response manifested starting at ~22:45 UT, immediately after observing the minimum Dst index, indicating the start of the recovery phase. A negative response is observed for several days. Detailed studies about this storm were made by Astafyeva *et al.* (2015) looking at a global overview of ionospheric response using multi-instruments and Nava *et al.* (2016) who presented the middle- and low- latitude ionospheric responses. In both studies, ionospheric positive storm effects during the onset and a strong decrease after the main phase were observed.

In Figure 4.5(b), a geomagnetic storm which occurred between 19-23 December 2015 led to a negative ionospheric response. This storm originated from a weak solar flare which produced a geo-effective CME cloud (Chashei *et al.*, 2016). During this period, the geomagnetic storm's

main phase was on 20 December 2015 with minimum Dst index of -155 nT at ∼20:00 UT. A negative ionospheric response is observed after the main phase of the storm. The ionospheric response returned to quiet time variability at ∼16:00 UT on 22 December 2015 with $\Delta foF2$ predominantly within ±20%. Both models in Figures 4.5(a) and 4.5(b) tried to follow the general trend during the storms' onset but performance degrades after the main phase. The ionospheric response during 19-23 December 2015 storm was captured better by both models as compared to 16-21 March 2015 storm. For both storms positive ionospheric enhancements are observed during and prior to the storms' main phase as seen in Figures 4.5(a) and 4.5(b) respectively. Both NN and LR models are unable to capture these positive enhancements. Previous studies have shown that mid-latitude positive ionospheric storms have the most unpredictable features and in general present spiky structures of the ionospheric response (Tsagouri *et al.*, 2000). Other studies, based on TEC modeling, also reported the inadequate capturing of short-term TEC variations during geomagnetic storm using NN models (e.g., Habarulema *et al.*, 2010; Uwamahoro and Habarulema, 2015).
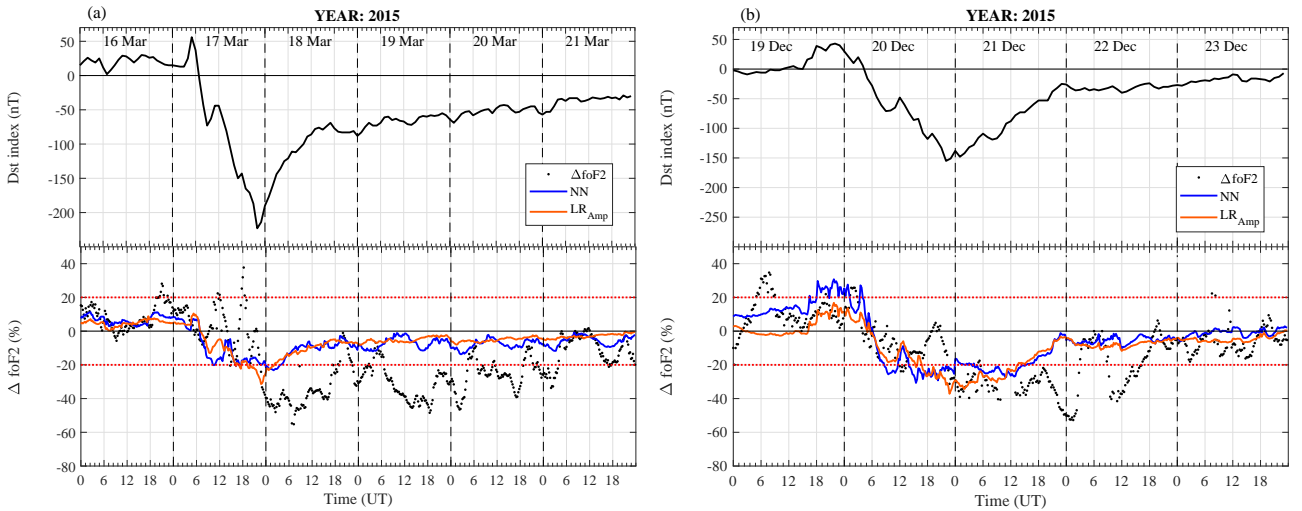
Figure 4.5: Geomagnetic storms selected during medium solar activity period for validation: (a) 16-21 March 2015 and (b) 19-23 December 2015.

4.3.3   Statistical analysis of results

Figure 4.6 shows scatter plots of the derived $\Delta foF2$ versus NN (black dots) and LR (red dots) predicted $\Delta foF2$ for (a) 2-7 October 2000, (b) 5-8 November 2001, (c) 28 October-1 November 2003, (d) 6-12 November 2004, (e) 16-21 March 2015, and (f) 19-23 December 2015 storm periods. A statistical analysis was performed by calculating the RMSE and the correlation coefficient (R) to quantify how well the models perform against the derived $\Delta foF2$. The calculated values of RMSE and R for all selected validation storms are presented in Figure 4.6. High R values are observed for storm periods which occurred during the maximum of solar cycle 23 (2-7 October 2000 and 5-8 November 2001). The 5-8 November 2001 storm has the highest

R values of 0.87 and 0.86 for LR and NN respectively. The 2-7 October 2000 storm has R values of 0.80 and 0.76 for LR and NN respectively. In terms of the R values, the performance of LR model is better compared to NN model for the 2-7 October 2000 and 5-8 November 2001 storm. However, the RMSE values for 2-7 October 2000 and 5-8 November 2001 storms are smaller for NN model in comparison with LR model. This means that the deviation between the derived and predicted data is less for NN model than for LR model. It is important to note that one statistical method may not be sufficient to draw a conclusion on the performance of the model. Both R and RMSE are required along with the examination of the data trend as seen in Figure 4.6. In general, performance for NN model is better than LR model in capturing the ionospheric responses.

Figures 4.6(c) and 4.6(d) represent scatter plots for storms which occurred on the declining phase of the solar cycle, during 28 October-1 November 2003 and 6-12 November 2004. The 28 October-1 November 2003 storm analysis gave R values of 0.61 and 0.57 for NN and LR models respectively. RMSE values are 18.38% and 18.57% for NN and LR models respectively during the 28 October -1 November 2003 storm period. Given the reported difficulties in modeling this storm period (e.g., Habarulema *et al.*, 2010; Ercha *et al.*, 2012; Uwamahoro and Habarulema, 2015), a correlation of 0.6 and the fact that 80% of the negative storm effect trend was reconstructed makes these results significant. For the storm period of 6-12 November 2004, both NN and LR models gave a similar correlation value of 0.76. RMSE values for both models are also comparable with LR providing a slightly lower value. Despite the fact that 6-12 November 2004 was one of sophisticated geomagnetic storms (e.g., Tsurutani *et al.*, 2008b; Echer *et al.*, 2010), both NN and LR models partly followed well the trend of the negative ionospheric response. During the declining phase, the R values range from 0.57-0.76 for LR model and 0.61-0.76 for NN model. These obtained R values are comparable to results reported by Zolesi *et al.* (2004) who presented large values (0.60 and 0.75) of correlation coefficient for a regional ionospheric model.
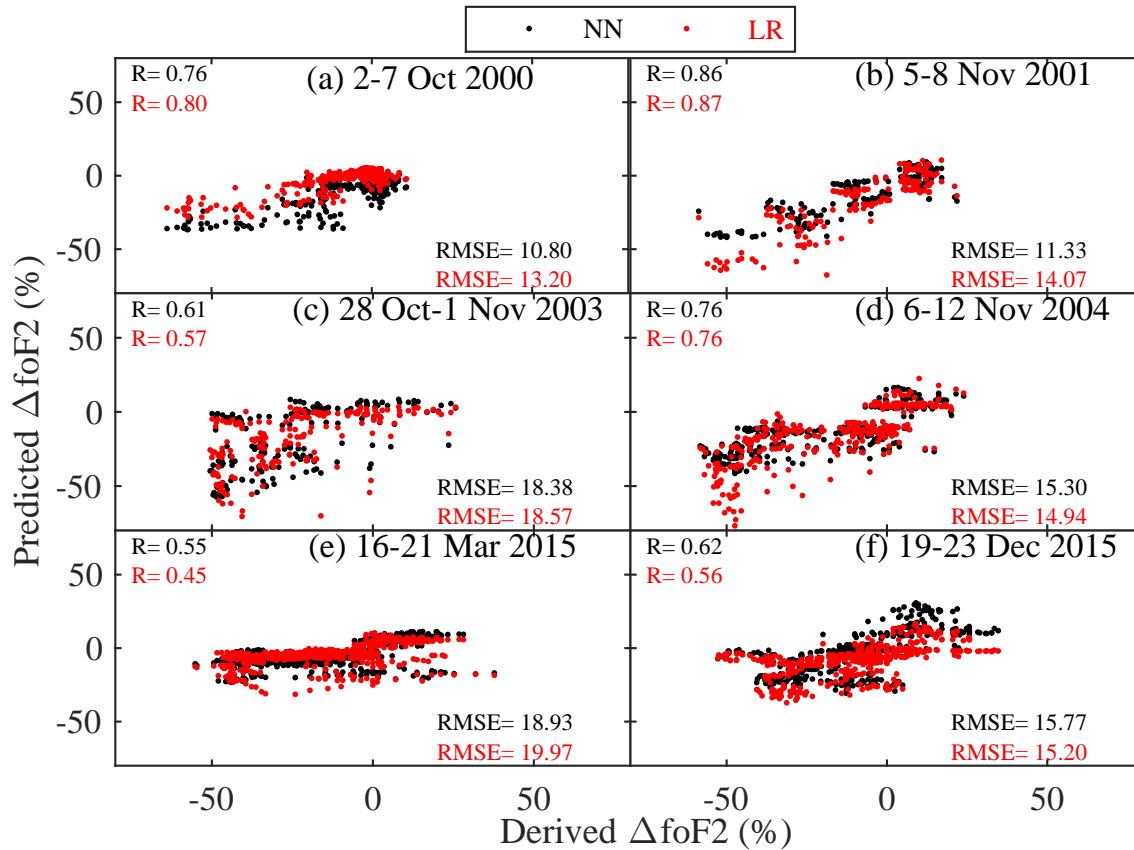
Figure 4.6: Statistical analysis of the NN and LR models' performance.

Figures 4.6(e) and 4.6(f) show scatter plots of extrapolation storms for the period 16-21 March 2015 and 19-23 December 2015. The R values between 0.55-0.62 for NN and 0.45-0.56 for LR models were obtained. From the statistical analysis of the presented storms (both in terms of R and RMSE values), it is clear that both NN and LR models perform better during the interpolation storms as compared to extrapolation storms. The NN model performs better for validation storms beyond the period of model development.

Similar to related studies (e.g., Fuller-Rowell *et al.*, 2000a; Habarulema *et al.*, 2009), these results show that the local developed model performs better than the climatological empirical International Reference Ionosphere (IRI) model. For example, the NN model gave a percentage improvement of about ∼23% and ∼7% for storm periods of 2-7 October 2000 and 5-8 November 2001 respectively over the IRI 2016 model with the F peak storm model option (Fuller-Rowell *et al.*, 1998, 2000a) activated.

4.4 Summary and Conclusion

Data from Grahamstown ($33.3°S, 26.5°E$) ionosonde station was used to build a database of ionospheric responses ($\Delta foF2$) during geomagnetic storms for the period 1996-2014. This storm time database was used to develop the NN and LR models to predict ionospheric $\Delta foF2$ changes. Three geomagnetic indices ($SYM - H$, AE, and local A) were investigated and the $SYM - H$ index gave the largest contribution (41% and 54% for NN and LR models respectively) in $\Delta foF2$ modeling. It has been shown that NN and LR models are capable of capturing most of the ionospheric responses during geomagnetic storms presented, which is important for monitoring and forecasting purposes. However, both models were unable to capture the short term features of the ionospheric storm variability including the observed positive enhancements which are known to be unpredictable (Tsagouri et al., 2000).

The correlation coefficient values from 0.45 - 0.87 for both NN and LR models were obtained for the presented ionospheric storms with weaker linear relationship for extrapolation storms and 28 October-1 November 2003 storm. Overall, the performance of both NN and LR models is comparable during selected storms which fell within the data period (1996-2014) used in modeling. However, when validated on storm periods beyond the period 1996-2014, the NN model gives a better performance (R=0.62) compared to LR model (R=0.56) for a storm that reached a minimum Dst index of -155 nT during 19-23 December 2015. It is also important to note that both NN and LR models are capable of capturing the ionospheric $foF2$ responses during two great geomagnetic storms (28 October-1 November 2003 and 6-12 November 2004) which had been proven to be difficult storms to model (e.g., Sahai et al., 2005; Uwamahoro and Habarulema, 2015).

The use of annual and semi-annual components was adopted from the work of Zhang et al. (2011) which applied these components in empirical orthogonal function analysis of TEC modeling, and showed that they significantly improve the LR modeling of ionospheric response to geomagnetic storms. Regardless of the shortcomings associated with NN and LR modeling, the modeled $\Delta foF2$ results show a promising trend for negative ionospheric response to geomagnetic storms. Although significant improvement is still required to improve the accuracy of the models especially for short term responses and extrapolation storms, the results reveal that the NN and LR models give adequate agreement with observational data in identifying the resulting ionospheric response as a result of storms. The study was expanded to include data from other South African ionosonde stations to develop a storm-time regional model, and this is the focus of Chapter 6.

Chapter 5

Estimation of foF2 from GPS TEC

The total electron content (TEC) and critical frequency of the F2 layer ($foF2$) are known to be highly correlated (e.g. Kouris *et al.*, 2004; Ssessanga *et al.*, 2014; Pignalberi *et al.*, 2019). In this chapter, a relationship between TEC and $foF2$ is established over South Africa for each ionosonde-GPS co-located station shown in Table 5.1. The relationship was obtained using polynomial functions based on storm-time (disturbed day) dataset with data period from 2003 - 2016. The storm-time expressions obtained from the four co-located stations are used to derive $foF2$ from GPS TEC data. In addition, four general expressions were also obtained using the entire dataset, thus including both quiet and disturbed periods. These expressions were established with the purpose of getting modeled monthly median $foF2$ for the calculations of $\Delta foF2$. The results of $\Delta foF2$ from modeled and measured $foF2$ data over the ionospheric pierce point (IPP) coverage around the ionosonde stations are presented. The results based on radio occultation data were also compared with results from modeled $foF2$ over the region which is outside the IPP coverage. The principal objective of estimating $foF2$ from GPS TEC is to have good spatial data coverage of $foF2$ over the South African region for the development of a regional ionospheric storm-time index.

5.1 $foF2$ and TEC data description

Data from the GPS receiver stations which are co-located with ionosonde stations in South Africa (see Table 5.1) are used to develop mathematical expressions describing the relationship between TEC and $foF2$. The period covered when developing the mathematical expression is only when both GPS and ionosonde data are available for a particular station. For instance, the ionosonde data over Grahamstown station is from 1996 and the GPS data starts from 2006. Because of the difference on the start dates of the measurements, the ionosonde data will be considered only from 2006 onwards. The data coverage for the four ionosonde-GPS co-located stations are: Grahamstown (2006 - 2016), Hermanus (2009 - 2016), Louisvale (2004 - 2016), and Madimbo (2003 - 2016). Since the objective of this study is to develop a storm-time ionospheric

Co-locations	Station Name	Location	Ionosonde Code	GPS Code
1	Hermanus	$34.42°S, 19.22°E$	HE13N	HNUS
2	Grahamstown	$33.32°S, 26.51°E$	GR13L	GRHM
3	Louisvale	$28.50°S, 21.20°E$	LV12P	
	Upington	$28.41°S, 21.26°E$		UPTN
4	Madimbo	$22.39°S, 30.88°E$	MU12K	
	Thohoyandou	$23.08°S, 30.38°E$		TDOU

Table 5.1: Station names for ionosondes and their co-located GPS receivers with geographic coordinates and station codes.

index, the criteria for creating a storm-time $foF2$ database was based on Dst $\leqslant$ -50 nT and Kp $\geqslant$ 4. The elevation angle of greater than 40° was considered in order to have as close as near vertical TEC data as possible, for comparison with ionosonde measurements which are based on vertical incidence sounders. In addition, the selection of elevation angle reduces the multipath effects while retaining useful amounts of data. Ionosonde data is measured at 15-minute interval and GPS TEC at 30 seconds interval. Because of the different time resolution, a direct comparison between ionosonde and GPS data can lead to a huge loss of GPS data with a possibility of isolated TEC outliers recorded exactly at the same time as ionosonde data. Because of this, a window of ±7.5 minutes was applied at each 15-minute interval to obtain averaged TEC data, for the 24 hours dataset except at 00:00 and 23:45 UT.

The $foF2$ depends on maximum electron density within the ionosphere through the following expression:

$$NmF2 = 1.24 \times 10^{10} foF2^2 \tag{5.1}$$

where $NmF2$ is the maximum electron density of the F2 layer measured in electrons/m^3. TEC is measured in TECU and 1 TECU = 10^{16} electrons/m^2. In order to compare parameters expressed in similar units when deriving polynomial functions, Equation 5.1 was used to obtain $NmF2$ from $foF2$ data and TEC values in electrons/m^2 was used instead of TEC data expressed in TECU. Similar approach was used in the study by Pignalberi *et al.* (2019). $NmF2$ data was then used together with TEC in electrons/m^2 to derive polynomial expressions at the four co-located stations indicated in Table 5.1. The polynomial expressions were then used to estimate $foF2$ from GPS TEC data over and within the IPP coverage area of each ionosonde location. As seen in Figure 5.1, there are GPS receiver stations which are outside the IPP coverage of any of the ionosonde locations. Figure 5.1 is an overview map of GPS receiver stations represented by black triangles, the four ionosonde stations shown in red dots, and the IPP coverage over the four ionosonde stations. The data presented is for an elevation angle of greater than 40° on 18 February 2015.
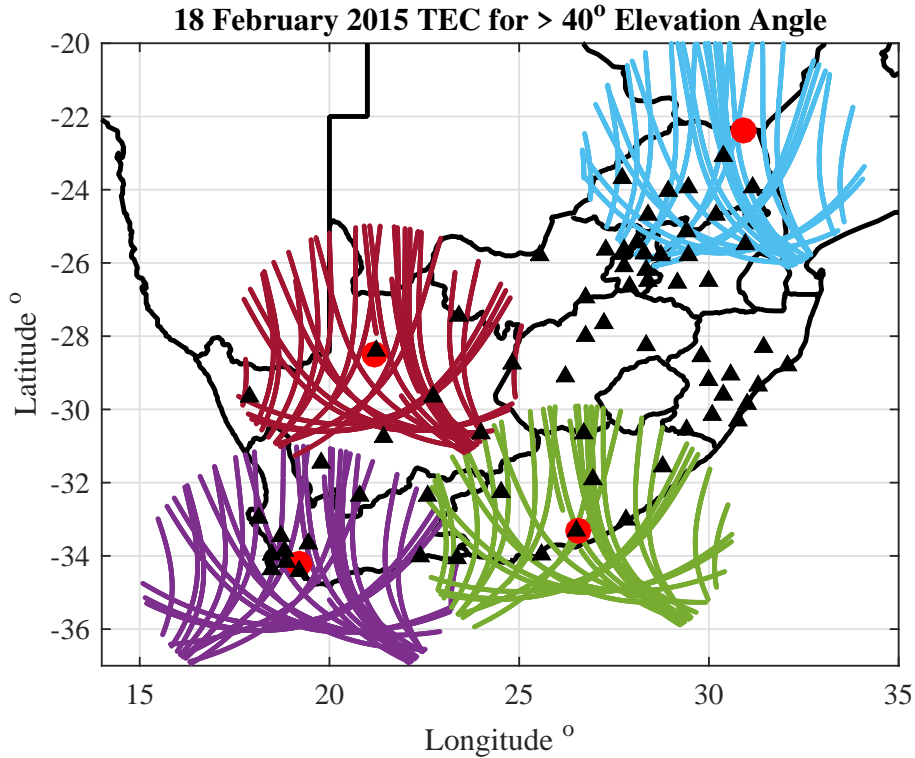
Figure 5.1: South African map showing the GPS receiver stations indicated by black triangles (▲), the four ionosonde stations represented by red dots (•) and the IPP coverage over each ionosonde location for an elevation angle greater than 40°

5.1.1   Relationship between $foF2$ and TEC

The relationship between $foF2$ and TEC is presented for the Hermanus station during storm conditions. Figures 5.2 (a) and (b) show the scatter plots of $foF2$ and TEC at 10:00 and 20:00 UT respectively from 2009-2017. In both Figures 5.2 (a) and (b), a linear relationship between $foF2$ and TEC is revealed with correlation coefficients of 0.88 and 0.82 at 10:00 and 20:00 UT respectively. The study by Ssessanga *et al.* (2014) found that the linear relationship between TEC and $foF2$ over the Grahamstown station between 20:00 - 23:00 UT is not consistent for arbitrary days in 2006 which matches with other studies (e.g. Kouris *et al.*, 2004; Krankowski *et al.*, 2007), where low correlation values are obtained during night time compared to daytime correlation. This may be due to plasmasphere contribution to TEC which is higher during night time than daytime (Belehaki *et al.*, 2004; Yizengaw *et al.*, 2008; Klimenko *et al.*, 2015). Despite the limitations, a strong correlation still exists between $foF2$ and TEC (Kouris *et al.*, 2004; Ssessanga *et al.*, 2014) during storm conditions as seen in Figures 5.2 (a) and (b), although this might have a negative impact on the modeled results especially during night time. Because of such a linear relationship, a polynomial function approach was taken to develop the mathematical relationship. The polynomial fitting technique is used to develop a function that estimates $foF2$ from TEC data. The $NmF2$ and TEC data were fitted with polynomial
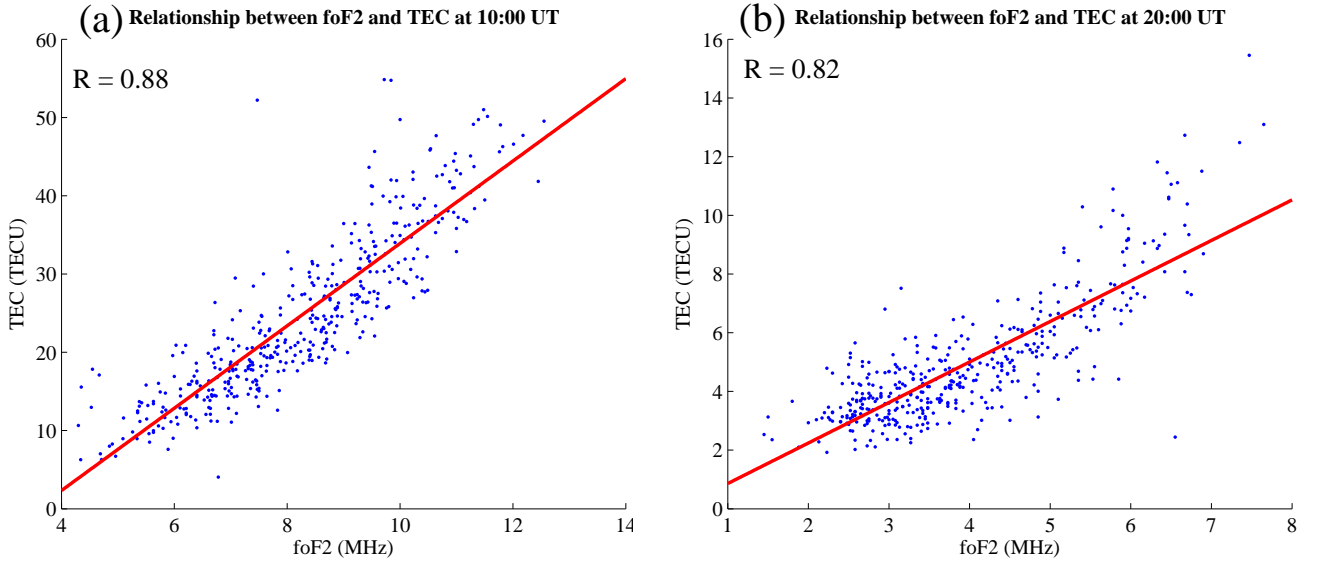
Figure 5.2: Scatter plot of $foF2$ versus TEC at (a) 10:00 UT and (b) 20:00 UT for Hermanus station from 2009-2017.

functions of degree of 1 to 5 for Grahamstown (2006 - 2016), Hermanus (2009 - 2016), Louisvale (2004 - 2016), and Madimbo (2003 - 2016). These polynomial functions of degree 1 to 5 can be mathematically expressed as follows:

$$
\begin{aligned}
f(x) &= a_0 + a_1 x \\
f(x) &= a_0 + a_1 x + a_2 x^2 \\
f(x) &= a_0 + a_1 x + a_2 x^2 + a_3 x^3 \\
f(x) &= a_0 + a_1 x + a_2 x^2 + a_3 x^3 + a_4 x^4 \\
f(x) &= a_0 + a_1 x + a_2 x^2 + a_3 x^3 + a_4 x^4 + a_5 x^5
\end{aligned}
\tag{5.2}
$$

where $f(x) = NmF2$ in electrons$/m^3$ and $x =$ TEC in electrons$/m^2$. Thus $NmF2$ can be derived as a function of TEC. The RMSE and correlation coefficient (R) between $NmF2$ and TEC were calculated for the first to fifth degree polynomial. Table 5.2 shows the results of RMSE and R for first to fifth order degree polynomial fitting for the Hermanus station. The results of the higher order fit does not show any significant improvement, hence the first order fit (linear function) was selected for this study. Similar method has been applied (Ssessanga *et al.*, 2014) with the purpose of obtaining the $foF2$ data over the African region due to the scarcity of ionosonde data.

		Polynomial	degree of	order:	
	First	Second	Third	Fourth	Fifth
R	0.9511	0.9556	0.9557	0.9558	0.9558
RMSE	1.2376×10^{11}	1.1804×10^{11}	1.1801×10^{11}	1.1788×10^{11}	1.1785×10^{11}

Table 5.2: The RMSE and R results of polynomial fitting for first, second, third, fourth, and fifth order obtained between $NmF2$ and TEC for Hermanus storm time data from 2009 - 2016.

5.2   Results and discussion

The results based on the linear polynomial fitting technique are discussed in this section. The storm-time polynomial function is used to estimate $foF2$ from TEC at GPS receiver locations that falls within the IPP coverage area of each ionosonde location. In order to calculate $\Delta foF2$ based on TEC data, monthly median $foF2$ data was derived using the general polynomial expression at ionosonde-GPS co-located stations. For each ionosonde location, the results of the modeled $\Delta foF2$ based on TEC data and actual $\Delta foF2$ from ionosonde data are presented for the storm period 6 - 11 September 2017 at co-location and other locations within the IPP coverage. The validation was also performed during the storm period 4-8 August 2011 at GPS receiver locations within and outside the IPP coverage area. The accuracy of the modeled data at locations outside the IPP coverage of any ionosonde location was evaluated using radio occultation data.

5.2.1   Monthly median $foF2$ based on TEC data

The monthly median values of $foF2$ were used in this study as a quiet-time basis to determined the relative deviation of $foF2$ ($\Delta foF2$) during geomagnetic storms. The actual $\Delta foF2$ was computed based on $foF2$ measurements from ionosondes and their monthly median values. The modeled $\Delta foF2$ ($\Delta foF2_p$) based on TEC data was calculated using the modeled monthly median $foF2$ ($foF2_{pm}$) rather than the monthly median values based on ionosonde measurements. This is to minimize the possible biases that may be introduced into the final results when making the comparison between actual and modeled $\Delta foF2$. To illustrate these biases, ionosonde $foF2$, modeled $foF2$ based on GPS TEC and monthly median $foF2$ from both ionosonde and modeled $foF2$ are presented in Figure 5.3 for the storm period of 6-11 September 2017 over Hermanus. Each graph in Figure 5.3, shows the Dst (red curve) and Kp (black bar) indices plotted on the top panel to indicate the storm occurrence date and time, and its magnitude. The middle panel represents the measured and modeled $foF2$ ($foF2$ and $foF2_p$ in black and red respectively) with ionosonde monthly median $foF2$ ($foF2_m$) shown by a blue curve. In addition, the modeled monthly median $foF2$ based on GPS TEC ($foF2_{pm}$) and TEC (green and magenta curve respectively) are shown in the middle panel of Figure 5.3 (b). The comparison between actual and modeled $\Delta foF2$ ($\Delta foF2$ and $\Delta foF2_p$) are plotted

in the bottom panel of each graph in black and red curves respectively. In Figure 5.3 (a), both $\Delta foF2$ and $\Delta foF2_p$ are computed based on $foF2_m$ from ionosonde measurements. In contrast, the $\Delta foF2_p$ in Figure 5.3 (b) was computed from $foF2_{pm}$ based on GPS TEC data instead of $foF2_m$ from ionosonde measurements.
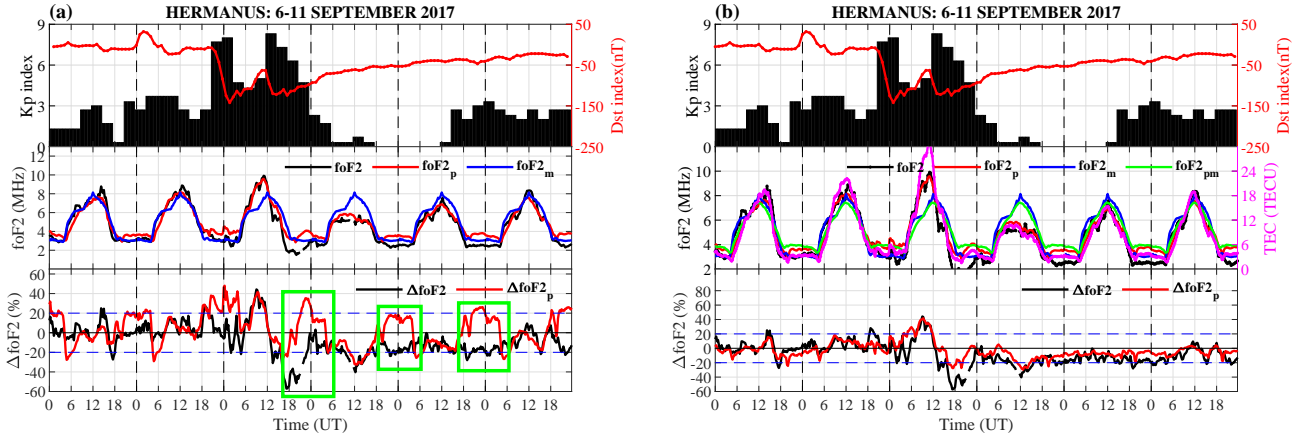
Figure 5.3: Comparison example of the measured and modeled $\Delta foF2$ plotted in black and red respectively in the bottom panel of each graph, (a) with the use of only ionosonde monthly median $foF2$ and (b) using both ionosonde and GPS TEC based monthly median values.

The discrepancy as a result of using only ionosonde $foF2_m$ is observed in the bottom panel of Figure 5.3 (a) in green squares. These differences in the bottom panel of Figure 5.3 (a) between $\Delta foF2$ and $\Delta foF2_p$ are observed at night which is consistent with other related studies (e.g. Kouris *et al.*, 2004; Ssessanga *et al.*, 2014; Pignalberi *et al.*, 2019). This may be due to the well known nighttime enhancement of the F-region electron content reported in several studies (e.g. Balan *et al.*, 1994; Dabas and Kersley, 2003; Burešová and Laštovička, 2008; Luan *et al.*, 2008; Li *et al.*, 2018). The study by Balan *et al.* (1994) reveals that enhancements are more frequent and slightly stronger in the southern hemisphere mid-latitude region. The electron density enhancements are different in different regions. The longitudinal variations caused by different downward plasma flux due to the magnetic field tilting effect is a possible cause of nighttime electron density enhancements (Luan *et al.*, 2008). The study by Li *et al.* (2018) also supports the idea of the plasmaspheric contribution to the mid-latitude ionosphere by downward plasma influx along the magnetic field lines which creates the nighttime ionization enhancements. With the electron density measurements at ~ 350 and 850 km, the results revealed that the enhancements are well placed between $\pm 30^o$ and $\pm 50^o$ magnetic latitude (Li *et al.*, 2018). This study also supports the fact that sometimes the regions above the F2 layer peak height provide the largest plasmaspheric contribution to TEC which has been observed to be more pronounced during night-time (Klimenko *et al.*, 2017). This provides possible reason for higher values of modeled $foF2$ which is based on GPS TEC compared to measured ionosonde $foF2$ during nighttime. Other studies have also observed large variations during night-time hours

between TEC and $foF2$ (e.g. Kouris *et al.*, 2004). It is therefore important to use the modeled monthly median $foF2$ from GPS TEC for the computation of modeled $\Delta foF2$ to minimize such differences as indicated at the bottom panel of Figure 5.3 (b) as opposed to Figure 5.3 (a).

The polynomial function used to estimate the $foF2_{pm}$ is a general expression derived from the entire dataset (quiet and disturbed conditions), which defines the relation between $foF2$ and TEC . To assess the performance of the developed expressions, the results of the $foF2_{pm}$ are compared with $foF2_m$ from ionosondes. Figure 5.4 represents the relationship between
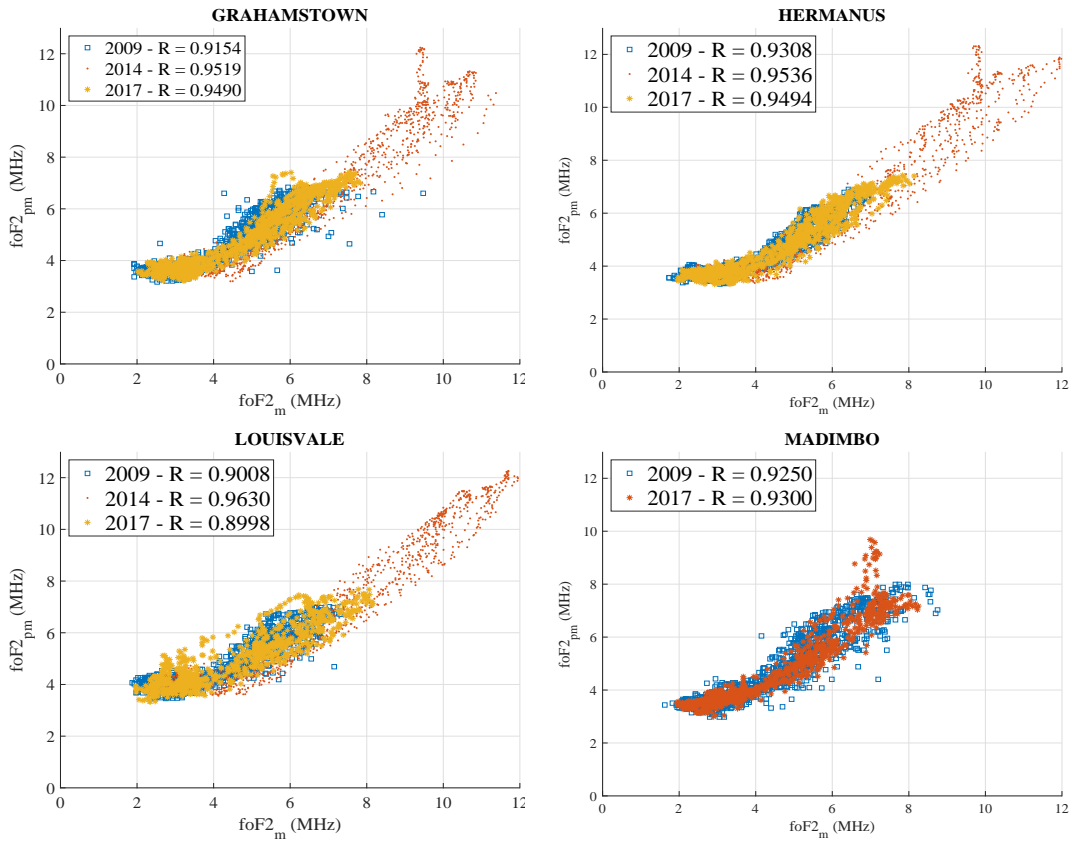
Figure 5.4: The relationship between the monthly median ionosonde $foF2$ and modeled $foF2$ from GPS TEC over the four co-located stations for the selected years: 2009, 2014, and 2017.

$foF2_m$ and $foF2_{pm}$ for Grahamstown, Hermanus, Louisvale, and Madimbo stations. The data for selected years during low and high solar activity periods as well as the declining phase of the solar cycle (2009, 2014, and 2017 respectively) were used in this study. Figure 5.4 (d) shows that Madimbo station does not have data during the high solar activity period, 2014. There is a huge data gap for ionosonde measurements over Madimbo station during which the instrument was not operational, that is from mid 2012 to end of 2015. This is the period of high solar activity during solar cycle 24.

The scatter plots in Figures 5.4(a) - (d) exhibit linear relationship between $foF2_m$ and $foF2_{pm}$. There is a clear distinction between frequencies during low and high solar activity period as presented in Figures 5.4(a) - (c). Higher values of monthly median $foF2$ are observed in 2014 with maximum values of ~12 MHz for Hermanus and Louisvale stations as shown in Figures 5.4(a) and (c). The maximum values over Grahamstown station are ~11 MHz during 2014 as seen in Figure 5.4(b). For the low solar activity period, 2009, the maximum monthly median $foF2$ values are ~7 - 8 MHz with just a few data points observed above 8 MHz in Figures 5.4(b) and (d). These are the typical maximum values of $foF2$ over the South African ionosonde stations (e.g Ssessanga *et al.*, 2014). Thus lower frequencies are expected during low solar activity as compared to higher frequencies during high solar activity period (e.g. Rishbeth and Mendillo, 2001; Ataç *et al.*, 2009). The 2017 year is near the minimum of the solar cycle 24 period with maximum frequencies of ~8 MHz for all stations.

The statistical analysis comparing $foF2_m$ and $foF2_{pm}$ over each co-located station is computed based on the root mean square error (RMSE), the mean absolute error (MAE), and the correlation coefficient (R) functions and is represented in Table 5.3. The average RMSE values of 0.39, 0.06 and 0.31 MHz are calculated over the four ionosonde stations during 2009, 2014 and 2017 respectively. Louisvale station has the highest values of RMSE for all the years presented. Overall, the 2014 solar maximum year presented the lowest RMSE values.

YEAR	GRAHAMSTOWN	HERMANUS	LOUISVALE	MADIMBO	Average
Root Mean Square Error (RMSE) in MHz					
2009	0.3793	0.3918	0.5238	0.2815	0.3941
2014	0.0586	0.0229	0.0904	-	0.0573
2017	0.2235	0.2876	0.4604	0.2439	0.3085
Mean Absolute Error (MAE) in MHz					
2009	0.5603	0.5358	0.6668	0.5375	0.5751
2014	0.6816	0.7225	0.6399	-	0.6813
2017	0.4550	0.5171	0.7496	0.5270	0.5622
Correlation Coefficient (R)					
2009	0.9154	0.9308	0.9008	0.9250	0.9180
2014	0.9519	0.9536	0.9630	-	0.9562
2017	0.9490	0.9494	0.8998	0.9300	0.9321

Table 5.3: The root mean square error (RMSE), the mean absolute error (MAE), and the correlation coefficient (R) between the measured and modeled monthly median foF2 ($foF2_m$) over Grahamstown, Hermanus, Louisvale, and Madimbo stations for the years 2009, 2014 and 2017.

The MAE is defined as:

$$\text{MAE} = \frac{1}{N} \sum_{i=1}^{N} \left| foF2_m - foF2_{pm} \right| \tag{5.3}$$

where $i = 1, 2, 3, ..., N$ is the number of data points. The average MAE for 2009, 2014 and 2017 are respectively 0.57, 0.68 and 0.56 MHz with correlation coefficients of 0.92, 0.96 and 0.93. These results indicate a relationship between $foF2$ and GPS TEC which are consistent with other related studies (e.g. Kouris *et al.*, 2004; Krankowski *et al.*, 2007; Ssessanga *et al.*, 2014; Otugo *et al.*, 2019; Pignalberi *et al.*, 2019). For example, Pignalberi *et al.* (2019) calculated a correlation coefficient of 0.948 between $foF2$ and GPS TEC over the Hermanus co-located GNSS and ionosonde station for the period 2011-2017. Furthermore, the study by Ssessanga *et al.* (2014) obtained the average RMSE and R values of 0.51 MHz and 0.7 respectively over the four South African ionosonde stations from 2006-2012. The high correlation that exist between $foF2$ and GPS TEC data means that the derived expression can be utilized with high confidence in estimating $foF2$ from GPS TEC in areas where ionosondes are not available. It should be noted that these results are only for the co-located stations. The same expressions need to be tested over the GPS locations which are located further away from ionosonde stations.

5.2.2   Monthly median $foF2$ comparison at different GPS locations

To test the validity of modeled monthly median $foF2$ from GPS TEC on a regional scale, ionosonde monthly median $foF2$ is compared with corresponding modeled monthly median values at the furthest GPS receiver stations within the IPP coverage area of each ionosonde location. The selected furthest GPS stations are Aliwal North, Calvinia, De Aar, and Benoni (ANTH, CALV, DEAR, and BENI). These stations are chosen with the anology that if the expression works for the furthest station, then the same expression will have similar performance for all other stations within the IPP coverage area. The distances between the ionosonde stations and the selected outermost stations are estimated to be $\sim$ 294, 311, 362, and 495 km for ANTH, CALV, DEAR, and BENI respectively. Figure 5.5 shows the RMSE values calculated between $foF2_m$ and $foF2_{pm}$ from ionosonde and GPS TEC respectively for each month of 2009, 2014 and 2017. The RMSE values between $foF2_m$ and $foF2_{pm}$ for the four co-located stations (GR13L, HE13N, LV12P, and MU12K) are plotted in blue curves with their respective furthest stations (ANTH, CALV, DEAR, and BENI) shown in orange as seen in in Figure 5.5. Figure 5.5 indicates that the RMSE values for the stations which are furthest away within the IPP coverage area are comparable to that of the co-located stations. The only large noticeable difference observed is over MU12K station during 2017 as seen in the bottom panel of Figure 5.5. The large difference may be due to the following factors during the estimation process: (i) the ionosonde and GPS stations are not exactly co-located, thus distance of about 90 km apart and (ii) the large data gap (Jul 2012 - Nov 2015) of ionosonde measurements may reduce the accuracy of the developed expression used to estimate $foF2$ from GPS TEC. During solar minimum period (2009) the higher RMSE values are observed around winter solstice months in the southern hemisphere with lower values during the equinox months. Similar trend is observed during 2017 period.
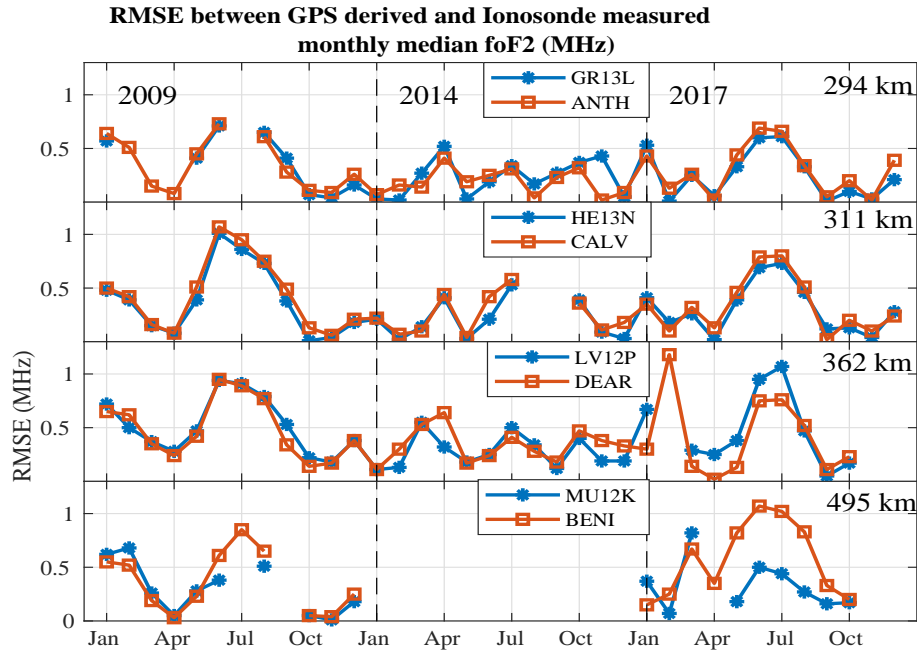
Figure 5.5: The comparison of RMSE values between measured and modeled monthly median $foF2$ ($foF2_m$ and $foF2_{pm}$) from ionosonde and GPS TEC respectively are presented. Four co-located and outermost stations within the IPP coverage area of each ionosonde location are compared for the selected years: 2009, 2014, and 2017.
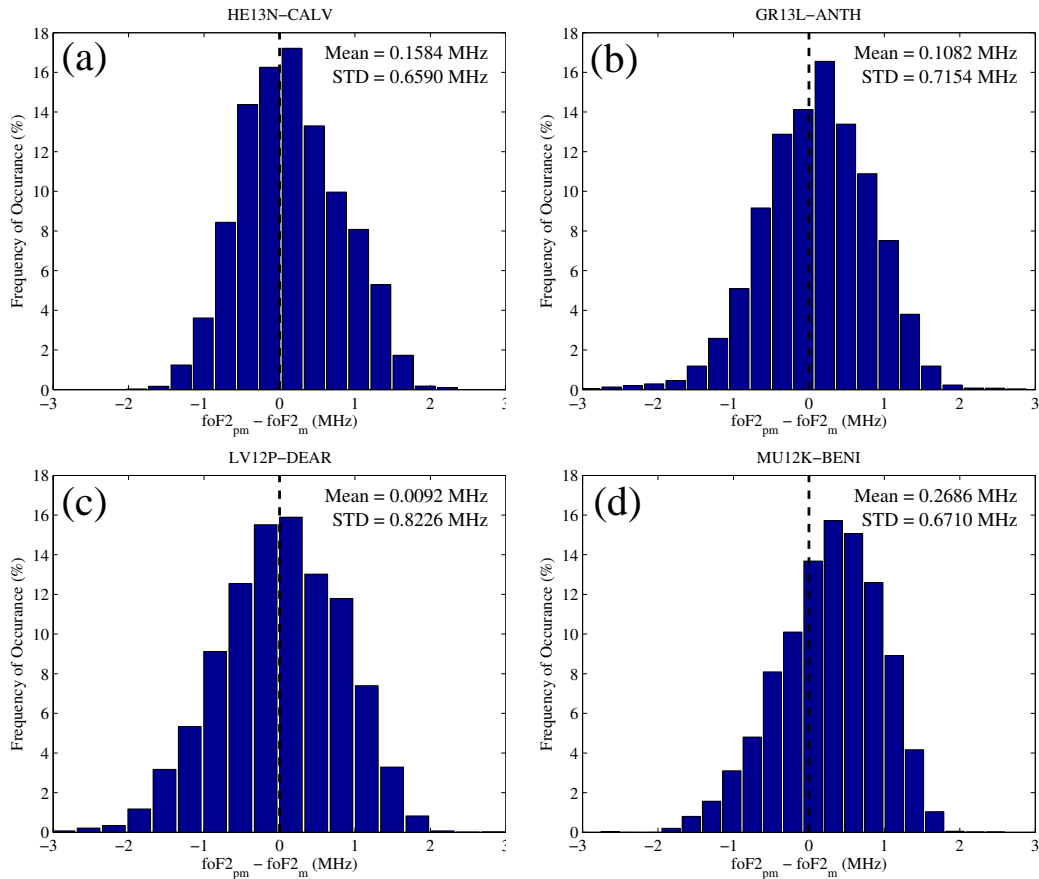
Figure 5.6: The histograms of residuals between modeled and measured monthly median $foF2$ values.

In general, lower values of RMSE are observed during solar maximum period of 2014. The overall RMSE values ranges between 0.05 MHz to 1.2 MHz which are within the frequency ranges obtained in other studies over the mid-latitude stations (e.g. Krankowski *et al.*, 2007; Ssessanga *et al.*, 2014). In the study by Krankowski *et al.* (2007), the RMS errors of 1-1.5 MHz between TEC-derived $foF2$ and measured $foF2$ for all mid-latitude European ionosonde stations during the disturbed month of October 2003 were presented. The results of this study show that the estimated monthly median $foF2$ ($foF2_{pm}$) over co-located stations can be used at other GPS receiver stations which fall within the IPP coverage area of each ionosonde location due to the small difference of RMSE values between the co-located stations. In order to determine the dominant error range, a histogram over each ionosonde location was plotted (see Figure 5.6). The mean and standard deviation (STD) were computed between the modeled and measured monthly median $foF2$. The results show that the expressions at ionosonde locations can be used to estimate $foF2$ with accuracy of less than 0.8 MHz.

5.2.3   Evaluation of modeled $foF2$ during the storm period of 6 - 11 September 2017

An illustration of how well the modeled $foF2$ performs compared to the measured $foF2$ for the storm period of 6 - 11 September 2017 is presented. Figure 5.7 shows the Dst index plotted in the top panel of each graph together with Kp index to represent the storm occurrence date and time as well as the magnitude of the storm over: (a) Grahamstown, (b) Hermanus, (c) Louisvale, and (d) Madimbo. The middle panel of Figure 5.7 is the measured $foF2$ (black curve), the modeled $foF2_p$ (red curve), the measured monthly median $foF2_m$ (blue curve), and $foF2_{pm}$ is the modeled monthly median $foF2$ from TEC data (green curve). The GPS TEC is plotted on the right handside of the middle panel in each graph (magenta curve). The bottom panel of each graph shows a comparison of actual and modeled $\Delta foF2$ ($\Delta foF2$ and $\Delta foF2_p$ in black and red respectively).

The September 2017 storm occurred during the downside of solar cycle 24, close to the minimum of a cycle. Different aspects of this storm period have been reported in several studies (Tassev *et al.*, 2017; Aa *et al.*, 2018; Yasyukevich *et al.*, 2018; Blagoveshchensky and Sergeeva, 2019; Imtiaz *et al.*, 2020; Mosna *et al.*, 2020, and references therein). During this storm period, two X-class x-ray solar flares were observed on 6 September 2017. An X2.2 peaking at ~9:10 UT was the most prolonged flare of solar cycle 24 and an X9.3 observed at ~12:02 UT was the most intense one (Tassev *et al.*, 2017; Yasyukevich *et al.*, 2018). The X9.3 was associated with a CME which resulted in an intense geomagnetic storm as determined by strong negative Dst index values on 8 September 2017. The two minimum values of Dst index were observed on 8 September 2017 with Dst = -142 nT at ~02:00 UT and Dst = -122 nT at ~14:00 UT, thus a
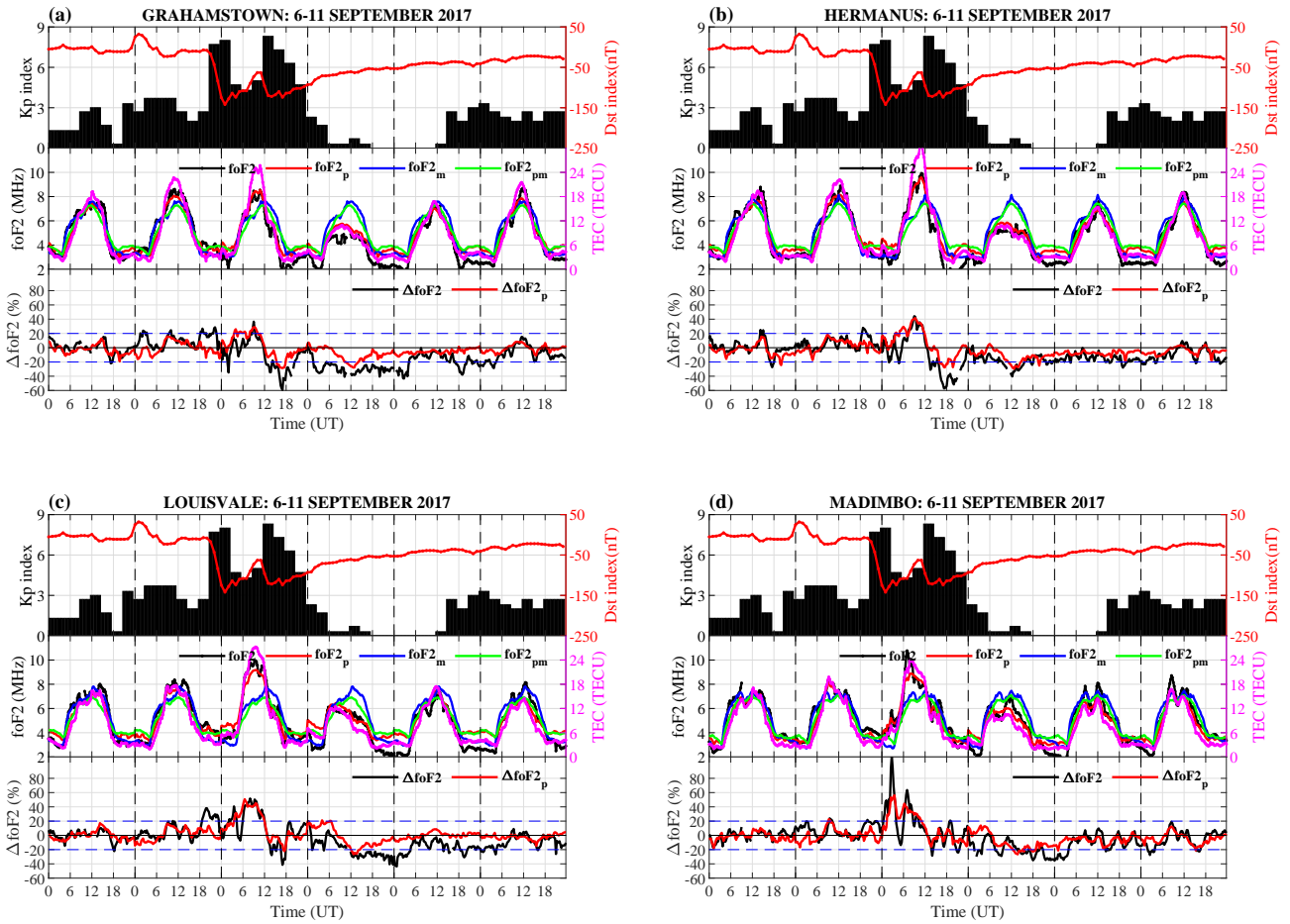
Figure 5.7: In each graph, Dst index is plotted in the top panel together with Kp index to represent the storm occurrence date and time, and its magnitude. The middle panel is the measured $foF2$ ($foF2$) plotted in black dots, modeled $foF2$ ($foF2_p$) in red dots and blue dots represent monthly median $foF2$ ($foF2_m$) from ionosonde measurements. The actual and modeled $\Delta foF2$ in the bottom panel ($\Delta foF2$ and $\Delta foF2_p$ respectively), are presented for four stations: (a) Grahamstown, (b) Hermanus, (c) Louisvale, and (d) Madimbo for the storm period 6 - 11 September 2017.

sequence of two storms (Blagoveshchensky and Sergeeva, 2019; Imtiaz *et al.*, 2020). The $\Delta foF2$ in Figure 5.7 shows a positive followed by a negative ionospheric storm response at all stations. Similar observation was made by Blagoveshchensky and Sergeeva (2019) at high to mid-latitude stations where TEC was enhanced during the first main storm phase and depressed during the second storm phase on 8 September 2017. Many other studies have observed electron density enhancement during the main phase of the storm on 8 September 2017 (e.g. Aa *et al.*, 2018; Imtiaz *et al.*, 2020). In Figure 5.7 (d), the Madimbo station observed a very strong positive ionospheric enhancement with $\Delta foF2$ greater than 80% compared to other ionosonde stations. One of the contributing factors may be the expansion of the equatorial ionisation anomaly (EIA) as far as 40°S magnetic latitude observed on 8 September 2017 (Habarulema *et al.*, 2020). The LV12P station data shows the second strongest ionospheric enhancement around

06:00 - 12:00 UT with $\Delta foF2$ greater than 50% as presented in Figure 5.7 (c). The $\Delta foF2$ over GR13L and HE13N stations in Figures 5.7 (a) and (b) exhibits only small enhancements between 06:00 and 12:00 UT. However, these two stations observed stronger negative values of $\Delta foF2$ of $\sim$60% at $\sim$15:00 - 19:00 UT on 8 September 2017 as seen in Figures 5.7 (a) and (b). The negative storm effect continued to the 9 September at all stations as seen in Figures 5.7 (a) - (d). The negative storm effect may have been triggered by the equatorward movement of depleted thermospheric O/N2 density ratio (e.g. Habarulema *et al.*, 2020; Imtiaz *et al.*, 2020). In all the Figures 5.7(a) - (d), the $\Delta foF2_{\mathrm{p}}$ estimated from TEC data is capable of reproducing the ionospheric response to the geomagnetic storm period 6-11 September 2017. The polynomial functions provide fairly accurate estimates of positive storm response of $\Delta foF2$ during the main storm phase on 8 September 2017 at $\sim$06:00 - 12:00 UT for all stations. The estimation of $\Delta foF2$ during the negative storm response is somewhat not well represented especially over Grahamstown. For example, in Figure 5.7 (a), Grahamstown data shows a negative storm response the whole day of 9 September 2017 while the $\Delta foF2_{\mathrm{p}}$ reveals a negative storm response for only few hours of the the day ($\sim$ 10:00 - 14:00 UT). However, this is not the case over Hermanus as seen in Figure 5.7 (b) where the $\Delta foF2_{\mathrm{p}}$ accurately represents the measured $\Delta foF2$.

Similar analysis was performed for the stations which are furthest away within the IPP coverage area known as Aliwal North (ANTH), Calvinia (CALV), Springbok (SBOK), and Pretoria (PRET) using the functions developed over GR13L, HE13N, LV12P, and MU12K stations respectively. Figure 5.8 represents the storm period 6 - 11 September 2017 for the selected stations. The stations considered for analysis are at the furthest locations from each ionosonde location within the IPP coverage area and where data was also available for this particular storm period. The reason for such an option was taken with the assumption that, if the function over each ionosonde location works at the furthest point, then it will be equally applicable at all other locations within the IPP coverage area. Similar performance is seen over all locations (ANTH, CALV, SBOK, and PRET) where $\Delta foF2_{\mathrm{p}}$ generally reproduces well the actual $\Delta foF2$ response. In Figures 5.8 (a) and (b), the positive storm response is observed earlier as seen by an increase in $\Delta foF2_{\mathrm{p}}$ few hours before the $\Delta foF2$ at around 03:00 - 06:00 UT on 8 September 2017. The positive storm response on 8 September 2017 at $\sim$6:00 - 12:00 UT is well captured by the modeled data as shown in Figures 5.8 (c) and (d) for SBOK and PRET respectively. The overall trend of $\Delta foF2$ during this storm period is well represented by the $\Delta foF2_{\mathrm{p}}$.
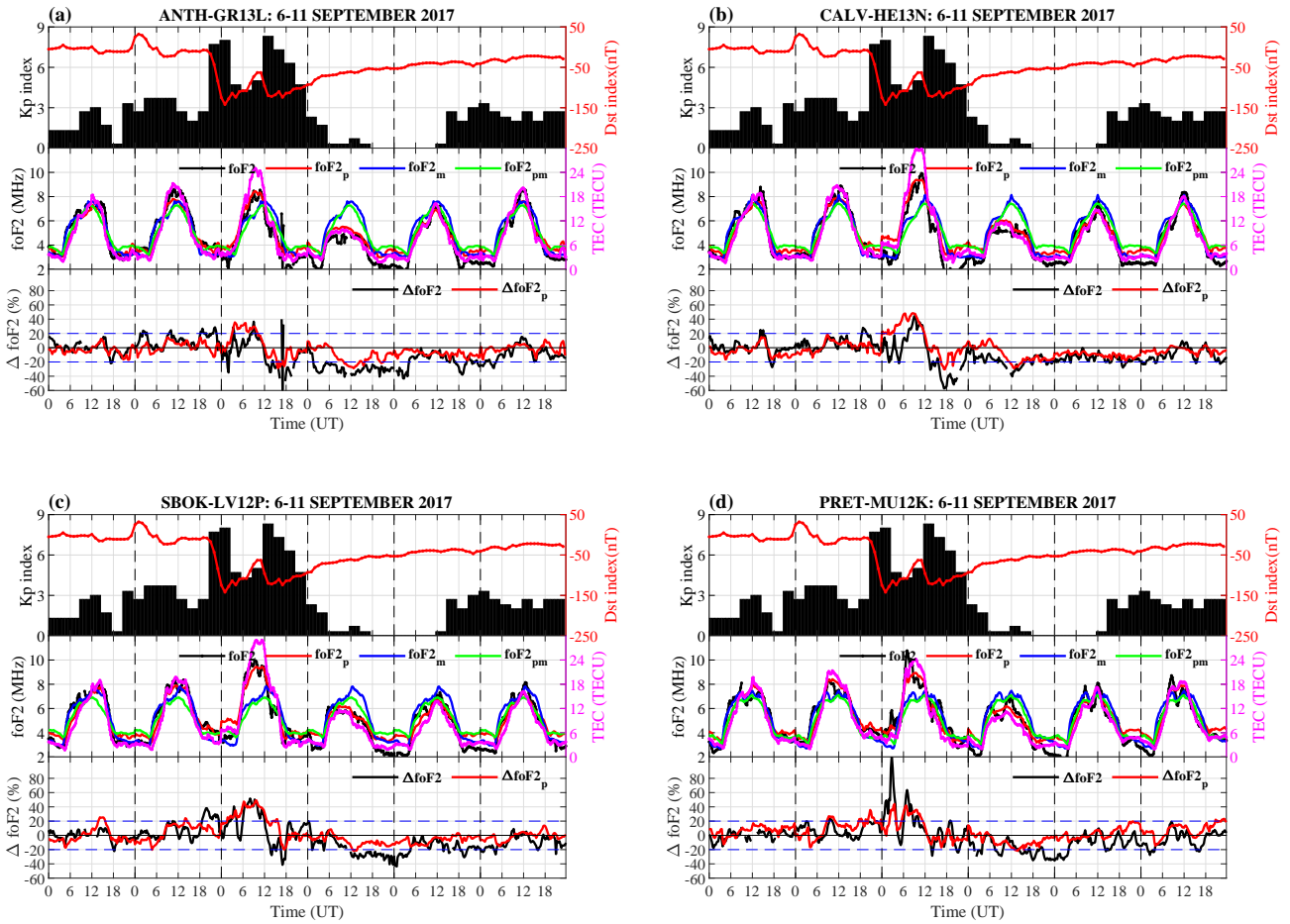
Figure 5.8: Similar to Figure 5.7, but for stations which are furthest away within the IPP coverage area of each ionosonde location: (a) Aliwal North (ANTH), (b) Calvinia (CALV), (c) Springbok (SBOK), and (d) Pretoria (PRET) for the storm period 6 - 11 September 2017.

5.2.4   Evaluation of modeled $foF2$ during the storm period of 4 - 8 August 2011

The performance of polynomial functions is also validated during the storm period of 4 - 8 August 2011 at four outermost GPS locations within the IPP coverage area (ANTH, CALV, SBOK, and PRET). A comparison of actual and modeled $\Delta foF2$ are presented. Figure 5.9 shows the storm occurrence date and time as indicated in the top panel of each graph by Dst and Kp indices (red curve and black bar respectively). The middle panel shows the measured and modeled $foF2$ in black and red ($foF2$ and $foF2_p$) respectively. Their respective measured and modeled monthly medians ($foF2_m$ and $foF2_{pm}$) are presented in blue and red respectively together with GPS TEC on the right hand side of the graph in magenta curve. The actual and modeled $\Delta foF2$ is respectively represented as $\Delta foF2$ (black curve) and $\Delta foF2_p$ (red curve) in the bottom panel of each graph in Figure 5.9. As seen in Figure 5.9, the storm main phase occurred on 5 - 6 August 2011 as a result of three consecutive CMEs. The three CMEs were associated with three M-class flares: M1.4, M6.0 and M9.3 on 2, 3 and 4 August
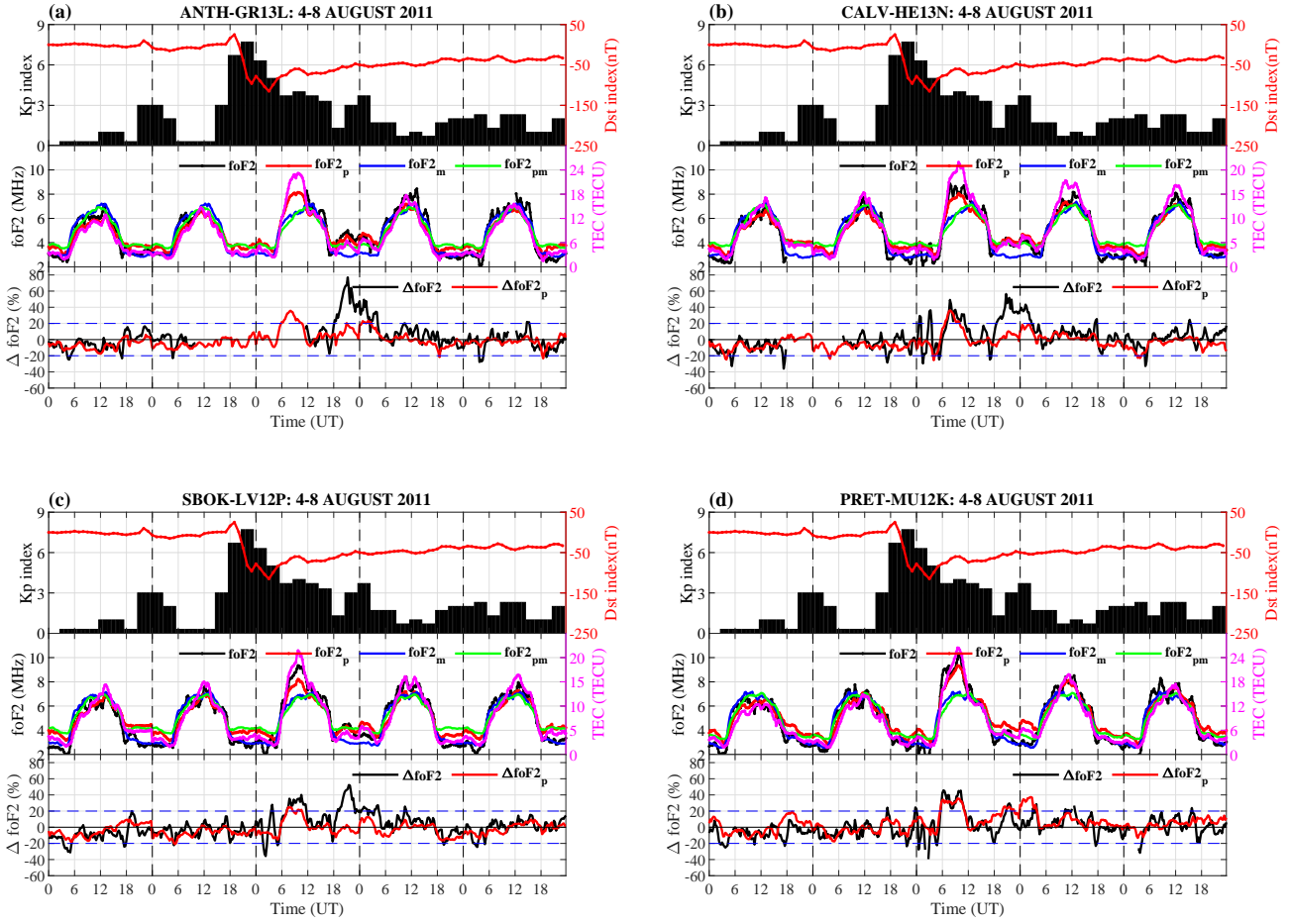
Figure 5.9: Comparison of actual and modeled $\Delta foF2$ during the storm period 4 - 8 August 2011 for (a) Aliwal North (ANTH), (b) Calvinia (CALV), (c) Springbok (SBOK), and (d) Pretoria (PRET)

2011 respectively (e.g. Rodkin *et al.*, 2017). The minimum Dst index value of -115 nT was recorded at around 03:00 UT on 6 August 2011 and is classified as a strong geomagnetic storm (Loewe and Prölss, 1997). The positive storm response is observed on 8 August 2011 at ∼06:00 - 12:00UT as seen by an increase in $\Delta foF2$ over HE13N, LV12P and MU12K in Figures 5.9 (b)-(d). Although a similar conclusion cannot be made with actual $\Delta foF2$ over GR13L due to unavailability of data, the modeled data was able to show a positive storm response at its most distant location (ANTH) within the IPP coverage area as shown by an increase in $\Delta foF2_{\mathrm{p}}$ around ∼06:00 - 12:00UT on 8 August 2011 (see Figure 5.9(a)). Daytime positive ionospheric storm effects at mid-latitudes are usually attributed to storm-induced neutral wind within the F region that pushes the plasma up the magnetic field lines (e.g. Rishbeth and Garriott, 1969; Prölss, 1993a, 1995, 2008; Buonsanto, 1999). Another increase in $\Delta foF2$ during the late hours on 6 August 2011 is observed, however it is less prominent over MU12K as seen in Figure 5.9(d). Both increases in $\Delta foF2$, thus positive storm effect, occurred during the recovery phase of geomagnetic storm on 6-7 August 2011. The analysis is done over the southern hemisphere midlatitude stations within the African sector. The positive ionospheric response observed

was later than over the North, Central, and South American sector as well as the Caribbean region, where TEC enhancements occurred during the storm's main phase (Valladares *et al.*, 2017). This may be due to fact that ionospheric response to magnetic storms depends on the local time of the storm onset (Prölss, 1993a, 2008). The ionospheric response with effect of the storm onset time during 5-7 August 2011 storm was analyzed in detail by Greer *et al.* (2017) where TEC enhancements were observed ∼2 hours after the storm onset. The study by Valladares *et al.* (2017) suggests that the prominent storm-enhanced density observed during this storm period was confined and localized to mid-latitude regions. It was concluded that the TEC enhancements observed over the mid-latitude region did not originate from low-latitude ionospheric fountain effect (Valladares *et al.*, 2017). The ionosphere response to geomagnetic storm during 5-6 August 2011 at different regions has also been reported in other studies (e.g. Huang *et al.*, 2014; Yiğit *et al.*, 2016). Looking at Figure 5.9, the modeled data were unable to capture the second positive storm effect as observed by $\Delta foF2_\mathrm{p}$ between 18:00 UT on 6 August to 06:00 UT on 7 August 2011 at all stations except MU12K. The inadequate results may be due to low correlation that exists at night between $foF2$ and TEC (e.g. Krankowski *et al.*, 2007; Ssessanga *et al.*, 2014), which is caused by higher plasmasphere contribution to TEC at night than daytime (e.g. Belehaki *et al.*, 2004; Yizengaw *et al.*, 2008; Klimenko *et al.*, 2015). In Figure 5.9(d), the positive storm is observed by both $\Delta foF2$ and $\Delta foF2_\mathrm{p}$ at around 20:00 UT on 6 August 2011. On the 7 August 2011, the $\Delta foF2_\mathrm{p}$ shows a longer positive storm effect as compared to what is observed ($\Delta foF2$). In general, the estimated data at the furthest stations within the IPP coverage area was able to represent a true picture of the ionosphere response as observed by MU12K data for both enhancements of $\Delta foF2$.

5.2.5   Statistical analysis

Figure 5.10 shows statistical results of RMSE and R which are computed using actual and modeled $\Delta foF2$ for 4-8 August 2011, 6-14 March 2012, 6-10 May 2016, and 6-11 September 2017. According to their Dst index minimum values, the 4-8 August 2011, 6-14 March 2012 and 6-11 September 2017 are classified as strong storms while 6-10 May 2016 was moderate (Loewe and Prölss, 1997). The RMSE values are presented in Figure 5.10 (a) to assess how close the modeled data is from observation at each co-located station(GRHM, HNUS, TDOU, and UPTN) and their respective most distant stations within the IPP coverage of each ionosonde location (ANTH, CALV, PRET, and SBOK). This is considering that observations/measurements are done over the four ionosonde stations (GR13L, HE13N, MU12K, and LV12P) and used as references. Considering all the storms presented, the lowest RMSE values are obtained for the 6-14 March 2012 storm period at all locations (see Figure 5.10 (a)). In addition, the RMSE values are almost similar during this storm period between co-located and furthest stations within the IPP coverage, except TDOU where data was not available. Similar observation can be seen for the storm period 4-8 August 2011 where the minimal differences when comparing RMSE
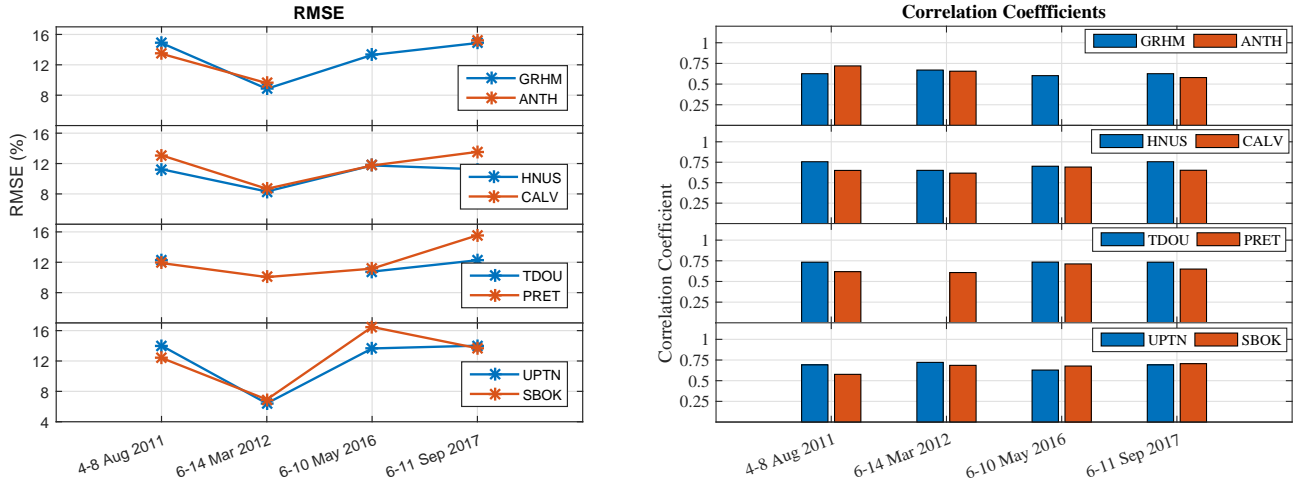
Figure 5.10: The RMSE values and correlation coefficients (Rs) between the actual and the modeled $\Delta foF2$ for selected storm periods. Each panel in (a) and (b) represent the GPS-ionosonde co-locations in blue with outermost GPS receiver stations in orange.

values calculated at co-located and furthest stations within the IPP area. This implies that the expression derived over a specific GPS-ionosonde co-location can be used to estimate $foF2$ for the computation of $\Delta foF2$ during storm conditions at other GPS locations. There is good agreement of RMSE values between HNUS and CALV as well as TDOU and PRET for 6-10 May 2016 storm. The storm period 6-11 September 2017 is considered to be an extrapolated storm because the data used for the development of expressions did not include 2017 data. Despite this fact, the RMSE values between GRHM and ANTH as well as UPTN and SBOK are comparable to others. However, slight differences of RMSE values between HUNS and CALV as well as TDOU and PRET during 6-11 September 2017 storm period is observed. In Figure 5.10 (b) the R values are presented to determine the capability of the derived expressions to reproduce the trend of the observed $\Delta foF2$. The overall R values range between 0.55 and 0.75 for all stations presented. For the storm period 4-8 August 2011, the R values for HNUS, TDOU, and UPTN are higher that for CALV, PRET, and SBOK respectively. In contrast, the most distant station (ANTH) has a higher value of R compared to the co-located station (GRHM). In general, for all the presented storm periods, the R values at co-located stations are higher that those stations which are far away within the region covered by IPP, which is an expected result. Interesting to note is that, higher R values are also obtained during the extrapolated storm 6-11 September 2017.

5.2.6   Evaluation of modeled $foF2$ over GPS locations outside the ionosonde's IPP coverage

The TEC data from GPS receiver stations which are outside the ionosonde's IPP coverage area have been used to estimate $foF2$ data based on the station's specific derived functions. Some of

the stations are approximately equidistant from the three ionosonde locations (GR13L, LV12P, and MU12K) and expressions over each specific location can be implemented. Because of the location of these GPS receiver stations with respect to the ionosonde stations, the measured $foF2$ from ionosonde will not be used to evaluate how well the modeled data performs. Instead, the satellite measurements from the Constellation Observing System for Meteorology, Ionosphere, and Climate (COSMIC)/Formosa Satellite 3 (FORMOSAT-3) (Hajj *et al.*, 2000; Rocken *et al.*, 2000; Lei *et al.*, 2007; Schreiner *et al.*, 2007) will be used as an independent validation dataset for the selected stations. The six COSMIC satellites operated simultaneously and their orbits were designed to spread apart gradually to their final orbits (Hajj *et al.*, 2000; Rocken *et al.*, 2000). The constellation tracks radio signals from the GPS as they pass through the Earths atmosphere. The vertical ionospheric electron density profiles are then retrieved from the radio occultation (RO) technique (Kursinski *et al.*, 2000) using the changes in frequency and amplitude of the GPS signals. In deriving electron density profiles from RO data, the Abel inversion technique is used and detailed description is well documented in a number of sources (e.g. Schreiner *et al.*, 1999; Hajj *et al.*, 2002; Lei *et al.*, 2007). There are existing validation studies that compare RO data with ionosonde, GNSS and other data sources over different regions (e.g. Chu *et al.*, 2010; Krankowski *et al.*, 2011; Liu *et al.*, 2011; Habarulema *et al.*, 2014; Habarulema and Carelse, 2016). For example, Krankowski *et al.* (2011) validated the electron density derived from FORMOSAT-3/COSMIC with ionosonde data over the European region. A good agreement was found between COSMIC and ionosonde data with correlation coefficients reaching 0.986 and 0.949 for $NmF2$ and maximum height of the F2 layer ($hmF2$) values, respectively. The study by Habarulema *et al.* (2014) performed a comprehensive validation of FORMOSAT-3/COSMIC, GRACE, and CHAMP with ionosonde data over the African low-latitude, equatorial, and midlatitude regions. A correlation of $foF2$ over GR13L in 2008 was computed to be 0.9175, 0.8389, and 0.9204 for COSMIC, CHAMP, and GRACE respectively. Another important study which provides confidence in using RO data as an independent validation dataset in the absence of ionosonde data is well documented in Habarulema and Carelse (2016). In this study, a long-term comparative analysis of RO $NmF2$ and $hmF2$ with ionosonde (GR13L) data was presented during geomagnetic storm periods from 2003 to 2015. This is a key reference study to this research because it is based on storm time data and was completed for the same area of focus. The advantage of using RO data is that it can be utilized over the regions where there is insufficient ground-based data (Krankowski *et al.*, 2011; Habarulema *et al.*, 2014). For this reason, the modeled $foF2$ data at locations outside the IPP coverage will be validated using the RO measurements from COSMIC.

Figure 5.11 (a) is an example of the electron density profiles from RO data for 7 August 2011 at different times of the day over Mafikeng (MFKG) station. The analysis was done by restricting profiles within a spatial resolution of 4.5° x 4.5° in both latitude and longitude space
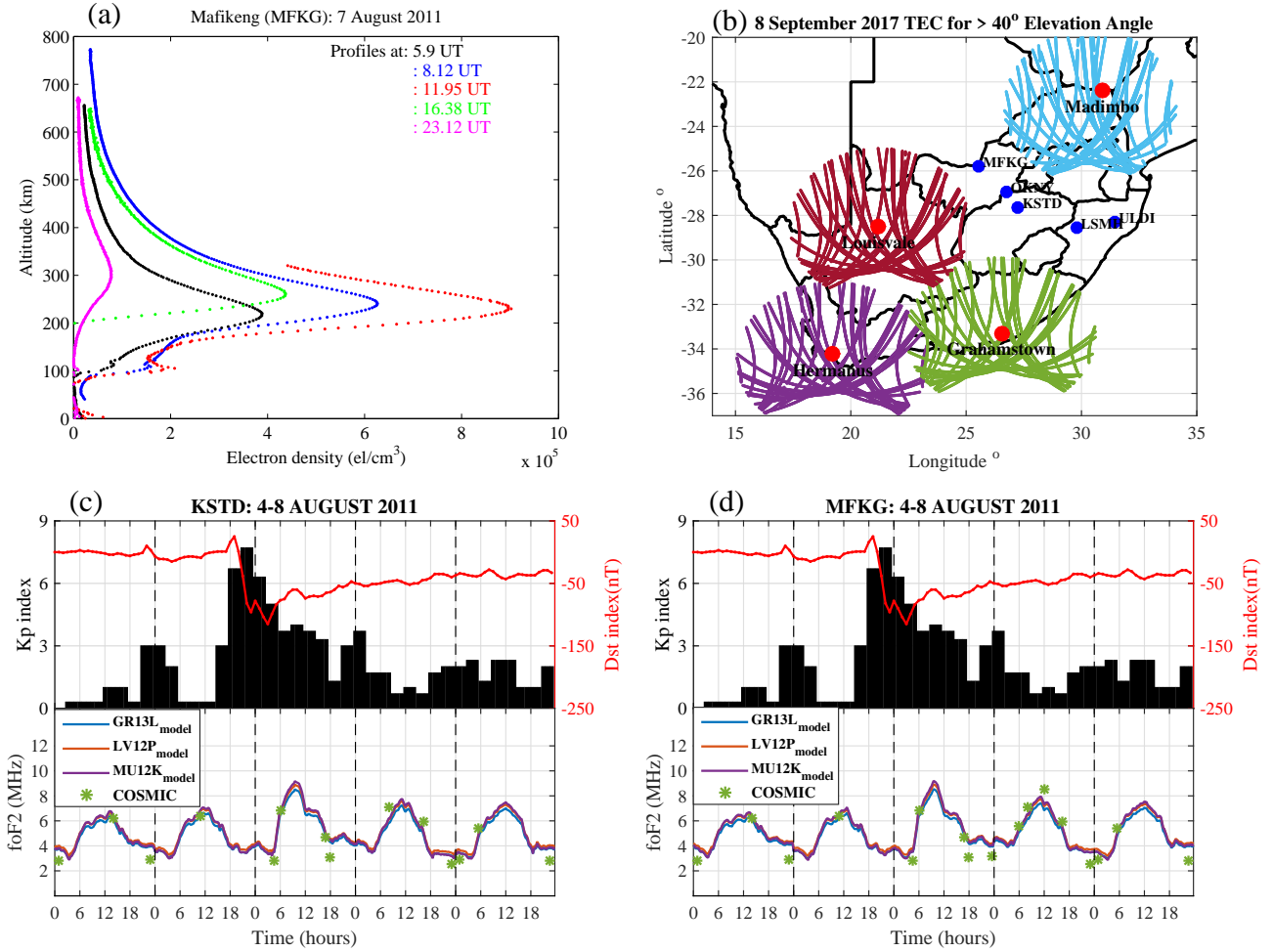
Figure 5.11: (a) An example of electron density profiles for 7 August 2011 at different times of the day over Mafikeng (MFKG) station, (b) a map showing the IPP area coverage over each ionosonde location with GPS receiver stations outside the IPP coverage, and the comparison between the modeled $foF2$ (GR13L in blue, LV12P in orange, and MU12K in purple) and COSMIC derived $foF2$ in green dots during the storm period 4 - 8 August 2011 over (c) Kroonstad (KSTD) and (d) MFKG stations.

(Habarulema et $al.$, 2014). As seen in Figure 5.11 (a), the electron density (el/cm^3) is plotted against the altitude in km. The maximum electron density of each profile is retrieved and then used to calculate $foF2$ using the known expression: $N_e(max)$=1.24x10^{10} $foF2^2$ el/m^3. This means that on this day over MFKG station, only 5 data points were obtained for comparison. Figure 5.11 (b) is a map illustrating the IPP area coverage over each ionosonde location with GPS receiver stations outside the IPP coverage. The IPPs were plotted for the selected elevation angle of $> 40^o$ on 8 September 2017. The stations in Figure 5.11 (b) are represented by MFKG, KSTD, OKNY, LSMH, and ULDI (Mafikeng, Kroonstad, Orkney, Ladysmith, and Ulundi) and have been used for the validation of modeled $foF2$ data with COSMIC derived $foF2$. Figures 5.11 (c) and (d) shows the three modeled and COSMIC derived $foF2$ represented by GR13L$_{model}$, LV12P$_{model}$, MU12K$_{model}$, and COSMIC in blue, orange, purple lines, and green

stars respectively. The comparison is done during the storm period 4 - 8 August 2011 over KSTD and MFKG stations (see Figures 5.11 (c) and (d) respectively). In each graph, Dst index (red curve) is plotted in the top panel together with Kp index (black bar) to represent the storm occurrence date and time as well as the magnitude of the storm. The three modeled $foF2$ data (GR13L$_{model}$, LV12P$_{model}$, MU12K$_{model}$) are based on the developed functions over each ionosonde station. The $foF2$ data from all three models represents well the COSMIC $foF2$ data points for both stations as seen in Figures 5.11 (c) and (d). The $foF2$ values from COSMIC during day time hours ($\sim$ 6:00 - 16:00 UT) are accurately captured by all three models over KSTD and MFKG stations. This is also true during the recovery phase of the storm on 6 August 2011 at $\sim$ 6:00 UT where minimal difference is observed. In the case of night time hours, all the models are over predicting the actual $foF2$ measurements. An example is seen in Figure 5.11 (d) at $\sim$ 18:00 and 23:00 UT on 6 August 2011 where modeled $foF2$ values are much higher than the COSMIC derived $foF2$ values. Figure 5.12 shows statistical results
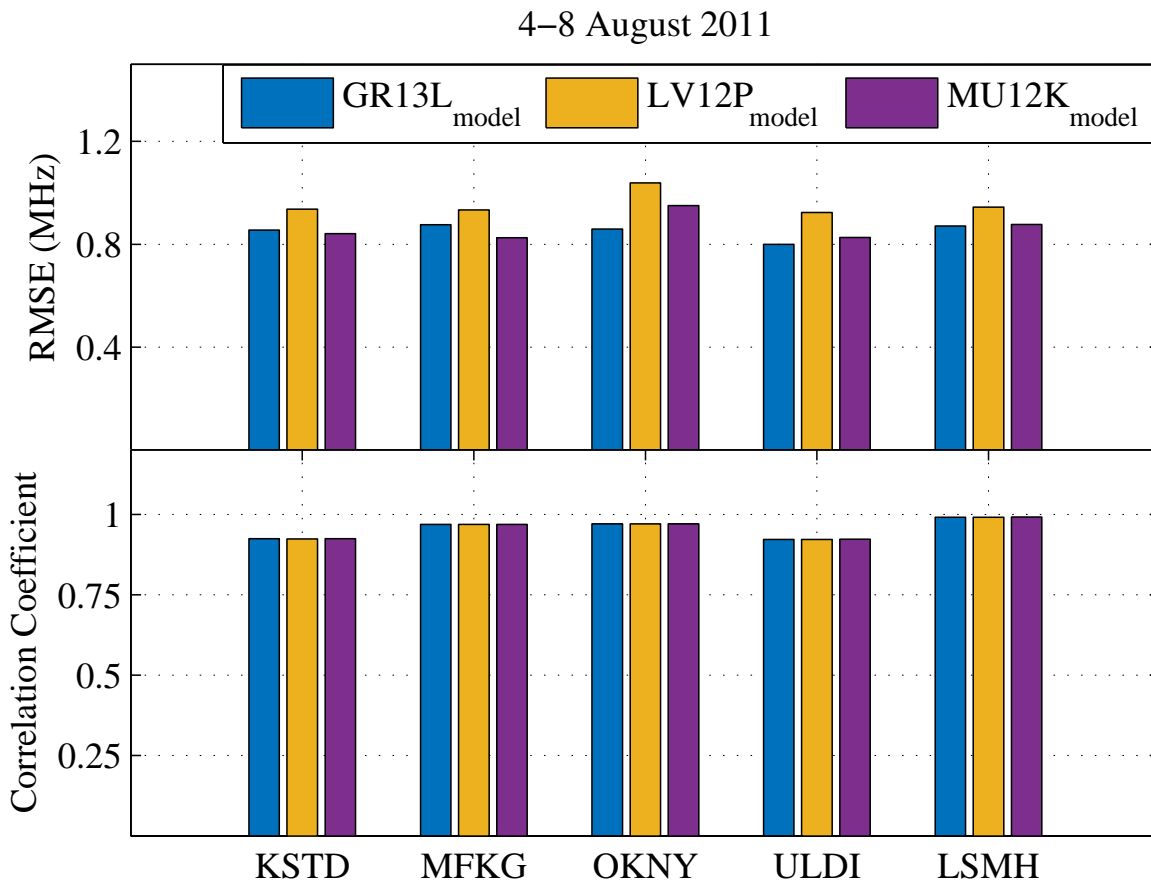
Figure 5.12: The RMSE and R values of COSMIC derived $foF2$ with the three modeled $foF2$ (GR13L$_{model}$, LV12P$_{model}$, MU12K$_{model}$ in blue, orange, purple respectively) during a storm period of 4-8 August 2011.

of RMSE and R which are calculated using modeled and COSMIC $foF2$ data for 4-8 August

2011. The results are also presented in Table 5.4. The top panel of Figure 5.12 represents the RMSE values in MHz for GR13L$_{model}$, LV12P$_{model}$, and MU12K$_{model}$ in blue, orange, and purple respectively. The analysis was performed over five different locations which are KSTD, MFKG, OKNY, ULDI, and LSMH for the same storm period. The correlation coefficient values are plotted at the bottom panel of Figure 5.12. The RMSE values at all stations for LV12P$_{model}$ appears higher than the other two models. The lowest RMSE values are observed for MU12K$_{model}$ over KSTD and MFKG stations, while over OKNY and ULDI, the GR13L$_{model}$ is the one with lowest RMSE values. Generally, the RMSE values ranges between 0.8 and 1 MHz which are within the error ranges obtained in other studies over the mid-latitude stations (Habarulema *et al.*, 2014). The average annual RMSE values of 0.88 and 0.84 for GR13L and MU12K respectively for the year 2008 were obtained (Habarulema *et al.*, 2014). The correlation coefficient of greater than 0.9 for all three models at all locations are obtained. This is consistent with the study by Habarulema *et al.* (2014) where authors computed a correlation coefficient of 0.9175 between COSMIC and ionosonde $foF2$ over GR13L in 2008. These statistical results demonstrate the ability of all three models in predicting $foF2$ with high accuracy in areas outside the IPP coverage of each ionosonde station.

Table 5.4: Statistical results of RMSE and R between the modeled and COSMIC $foF2$ data for 4-8 August 2011

Station Code	RMSE (MHz)			Correlation Coefficient		
	GR13L$_{model}$	LV12P$_{model}$	MU12K$_{model}$	GR13L$_{model}$	LV12P$_{model}$	MU12K$_{model}$
KSTD	0.86	0.94	0.84	0.92	0.92	0.93
MFKG	0.88	0.93	0.83	0.97	0.97	0.97
OKNY	0.86	1.04	0.95	0.97	0.97	0.97
ULDI	0.80	0.92	0.83	0.92	0.92	0.92
LSMH	0.87	0.94	0.88	0.99	0.99	0.99

5.3   Summary and conclusion

In this chapter, a mathematical relationship between $foF2$ and TEC during storm conditions over four midlatitude stations: Grahamstown (2006 - 2016), Hermanus (2009 - 2016), Louisvale (2004 - 2016), and Madimbo (2003 - 2016) was established. Because of the linearity between $foF2$ and TEC, a choice of polynomial function was selected to obtain the mathematical expressions. Since the study is based on ionospheric $foF2$ response to geomagnetic storms ($\Delta foF2$), careful consideration on the use of monthly median $foF2$ was taken specifically for modeled $\Delta foF2$. A separate mathematical expression to derive monthly median $foF2$ from TEC data was established for this purpose. The results show that the expressions at ionosonde locations can be applied at other GPS locations within the IPP coverage area with accuracy of less than 0.8 MHz. The developed functions during storm conditions were validated at selected

GPS locations which are co-located and furthest within the IPP coverage of each ionosonde location. The comparison between modeled and actual $\Delta foF2$ (%) were performed for selected storm periods of 4-8 August 2011, 6-14 March 2012, 6-10 May 2016, and 6-11 September 2017 at co-located stations as well as stations within the IPP coverage area of each ionosonde location. The average RMSE and R values of 12.0583 and 0.6722 respectively for all stations were obtained. GPS stations which are outside the IPP coverage area were also validated using an independent RO dataset from COSMIC for one storm period of 4-8 August 2011. The results showed a correlation coefficient of more than 0.9 with RMSE values of not more than 1 MHz. The results of this chapter provide a certain degree of confidence that the modeled $foF2$ data can be applied in the development of a regional ionospheric storm-time index with high spatial resolution.

Chapter 6

Regional ionospheric storm-time index model

This chapter discusses the regional modeling results of the ionospheric storm-time $foF2$ response based on artificial neural networks (ANNs) over the South African mid-latitude region. The development of a regional ionospheric storm-time model was based on $foF2$ measurements from the four South African ionosonde stations (Grahamstown $33.3°S, 26.5°E$, Hermanus $34.42°S, 19.22°E$, Louisvale $28.50°S, 21.20°E$, and Madimbo $22.39°S, 30.88°E$). The criteria for selecting the storm-time $foF2$ data was based on Dst $\leqslant$ -50 nT and/or Kp $\geqslant$ 4. The NN model was evaluated over the ionosonde locations and randomly selected GPS stations. The analysis of the results comparing actual and NN modelled $\Delta foF2$ was performed during the following storm periods: 5-8 November 2001, 19-24 November 2003, 7-12 November 2004, and 19-23 December 2015. The results presented in this chapter are the initial attempt towards the development of a regional ionospheric storm-time index.

6.1   Development of a storm-time $foF2$ dataset

The $foF2$ measurements from the four South African ionosonde stations were used in creating the storm-time dataset for a NN regional model. Figure 6.1 indicates the $foF2$ data coverage for (a) Grahamstown (GR13L), (b) Hermanus (HE13N), (c) Louisvale (LV12P), and (d)Madimbo (MU12K) for the period between 1996-2016, 2009-2016, 2000-2016, and 2000-2016 respectively. Comparing data from the four stations, Grahamstown has the longest dataset covering solar cycle 23 and 24, followed by Louisvale. Hermanus has the least dataset covering only one solar cycle 24. It is important to note a huge data gap in Figure 6.1(d) for Madimbo station from mid 2012 to end of 2015. The $foF2$ data in MHz is plotted with Dst index during the same period to show the magnitude and the occurrence of geomagnetic storms. The black dashed horizontal lines represent geomagnetic storm categories as classified by Loewe and Prölss (1997) as weak to moderate (-50 nT $\leqslant$ Dst $\leqslant$ -100 nT), strong (-100 nT $\leqslant$ Dst $\leqslant$ -200 nT), severe (-200 nT $\leqslant$

Dst $\leqslant$ -350 nT), and great (Dst $\leqslant$ -350 nT). Considering the data used for modeling, Figure 6.1 shows that there are few data points which fall within severe to great geomagnetic storms. The majority of the storms are within the weak to moderate classification. The focus of the study is to model the ionospheric $foF2$ response to geomagnetic storms ($\Delta foF2$) according to the following expression:

$$\Delta foF2 = \left(\frac{foF2 - foF2_m}{foF2_m} \right) \times 100 \tag{6.1}$$

where $foF2_m$ is the monthly median of $foF2$ values in MHz. The $\Delta foF2$ values within
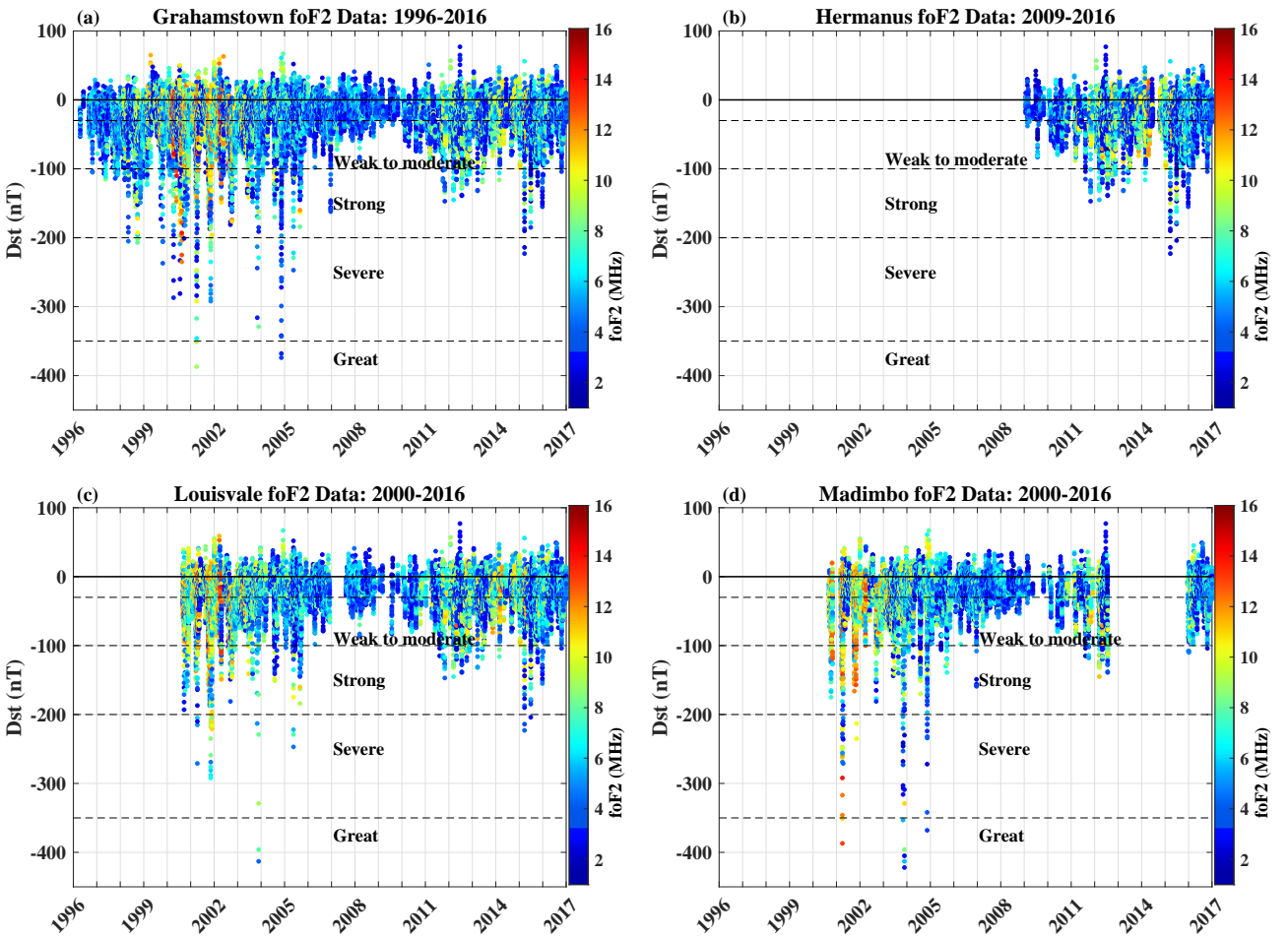
Figure 6.1: The $foF2$ in MHz for (a) Grahamstown (1996-2016), (b) Hermanus (2009-2016), (c) Louisvale (2000-2016), and (d) Madimbo (2000-2016) is plotted with Dst index over the time period considered for model development. The black dashed horizontal lines represent geomagnetic storm categories as classified by Loewe and Prölss (1997).

the range of ± 20 % has been established to be the quiet time variability as reported and used widely in literature (e.g. Danilov, 2001, 2013; Gao *et al.*, 2008; Matamba *et al.*, 2015). The actual $\Delta foF2$ for the selected storm periods is computed over the ionosonde stations (red dots) and GPS stations (green triangles) as represented in Figure 6.2 to evaluate the

model's performance. The four GPS stations which are randomly selected for model validation
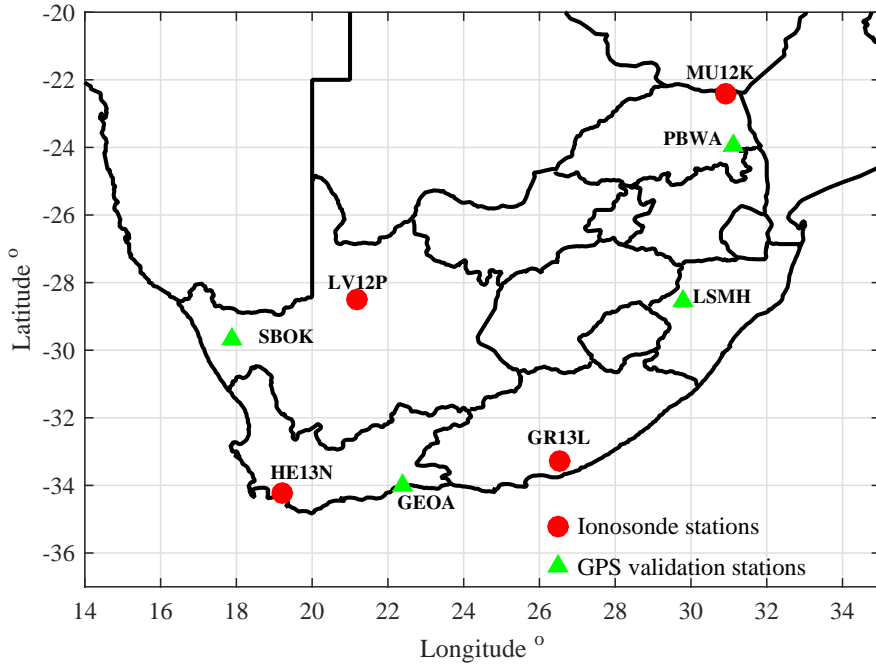
Figure 6.2: South African map showing the four ionosonde stations represented by red dots (●) and the randomly selected GPS stations which are represented by green triangles (▲)

are George $(34.00°S, 22.38°E)$, Ladysmith $(28.56°S, 29.78°E)$, Phalaborwa $(23.95°S, 31.13°E)$, and Springbok $(29.67°S, 17.88°E)$ and are represented by GPS station codes GEOA, LSMH, PBWA, and SBOK respectively. It is important to note that for assessing how well the model is performing over the GPS locations, the actual $\Delta foF2$ which is compared to the NN modeled $\Delta foF2$ is based on TEC data using the developed equations which are described in chapter 5.

6.2 Regional modeling inputs

The inputs for the development of the neural network based model comprises of time of the day, hr (diurnal variation), day number of the year, dn (seasonal variation), geographic longitude and latitude, the $F_{10.7p}$ solar flux index (solar activity), and geomagnetic activity indices (symmetric disturbance in the horizontal component of the Earth's magnetic field $SYM - H$ and auroral electrojet AE). To avoid unrealistic numerical discontinuity, cosine and sine components are introduced for the hr and dn (McKinnell and Poole, 2004b; Oyeyemi *et al.*, 2006; Habarulema *et al.*, 2009; Uwamahoro and Habarulema, 2015). The semi-annual variation is also considered (Zhang *et al.*, 2011; Uwamahoro *et al.*, 2018b) for dn as defined in Equation 4.3 of chapter 4. Thus, there is a total of eleven input parameters for the development of neural network-based model. In order to determine the optimum NN model, several models were developed by varying the number of hidden nodes and calculating the RMSE values between the modeled
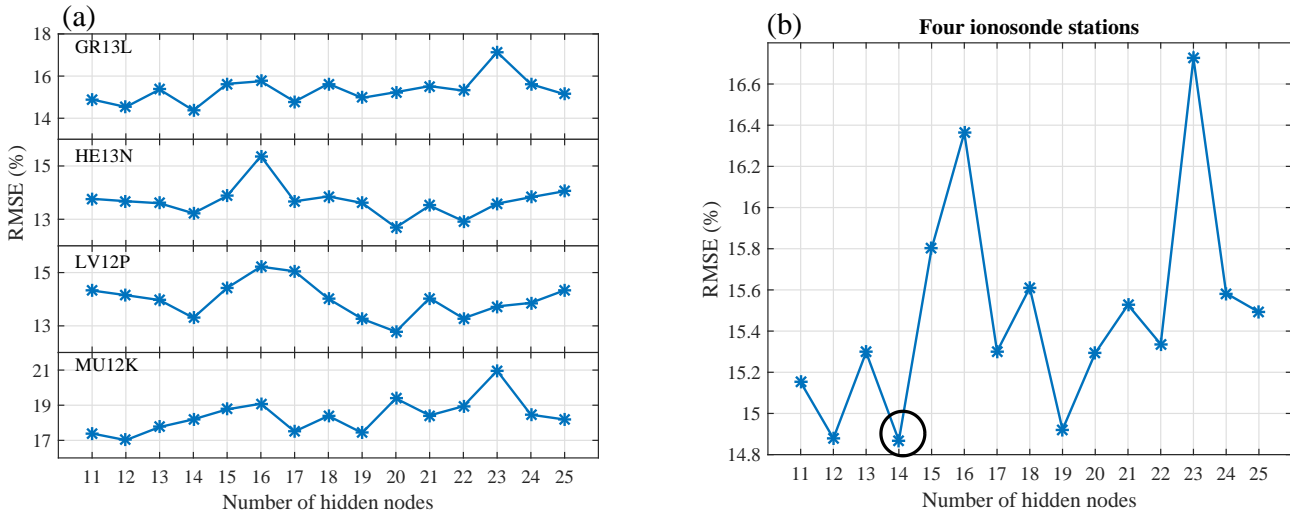
Figure 6.3: RMSE values between derived $\Delta foF2$ and NN predictions with number of hidden nodes for validation storm periods (a) over a station: GR13L, HE13N, LV12P, and MU12K and (b) the average RMSEs over the four stations.

and the derived $\Delta foF2$. The storm periods reserved for validations (excluded from training set) are 5-8 November 2001, 19-24 November 2003, 7-12 November 2004, and 19-23 December 2015. Figure 6.3 shows the RMSE values (%) against the number of hidden nodes. Initial number of hidden nodes is 11, which is equal to the number of input parameters used in the model. The optimum solution was reached using 14 hidden nodes which gave the lowest RMSE value. For this application, the optimum NN architecture was 11:14:1 which is defined based on the 11 input variables, 1 output ($\Delta foF2$) variable and 14 hidden nodes chosen based on the lowest RMSE method that has been used in previous ionospheric modeling studies (McKinnell and Poole, 2004b; Habarulema *et al.*, 2009; Uwamahoro and Habarulema, 2015).

6.3   Results and discussion

This section describes the performance of the regional NN model. The model results are validated for the storm periods of 5-8 November 2001, 19-24 November 2003, 7-12 November 2004, and 19-23 December 2015 over all the four ionosonde stations and the selected GPS receiver locations shown in Figure 6.2. The magnitude of the storms are classified according to Loewe and Prölss (1997) based on the minimum Dst index values as presented in Table 6.1.

Table 6.1: Classification of the selected storm periods by Dst (Loewe and Prölss, 1997).

Storm period	Minimum Dst (nT)	Minimum Dst Date	Classification
5-8 November 2001	-292	6 November 2001	Servere
19-24 November 2003	-422	20 November 2003	Great
7-12 November 2004	-374	8 November 2004	Great
19-23 December 2015	-155	20 December 2015	Strong

6.3.1   Validation results at ionosonde locations

Figure 6.4 represents the validation results of the NN model with actual data during the storm period of 5-8 November 2001. This is a CME-driven storm that was associated with a solar flare which occurred on 4 November 2001 at ∼16:00 UT (e.g. Zhang *et al.*, 2007; Horvath and Lovell, 2008).
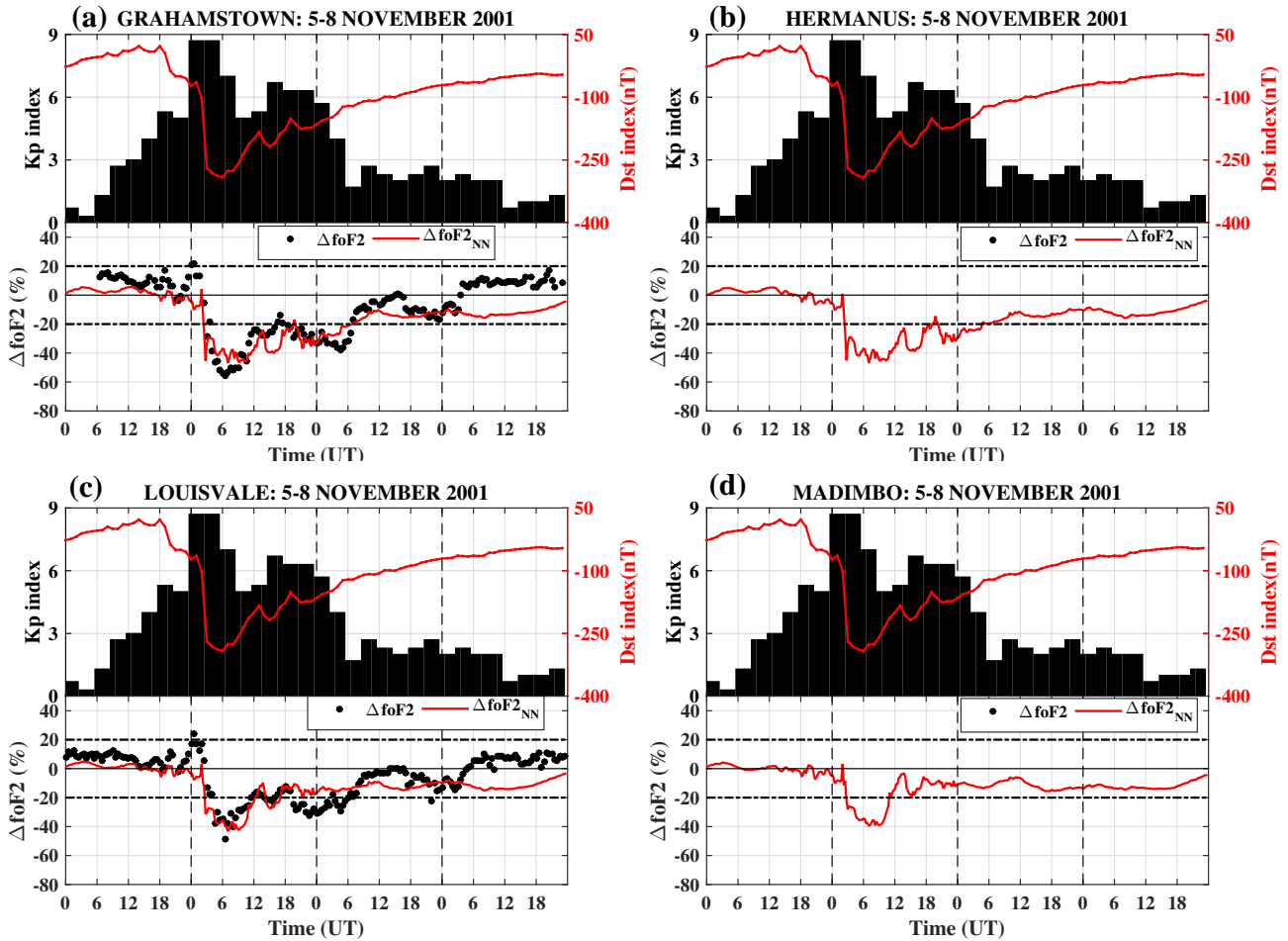
Figure 6.4: The Dst index (red curve) is plotted on the top panel of each graph together with Kp index (black bars) to represent the storm occurrence date and time, and its magnitude. The bottom panel of each graph shows the actual $\Delta foF2$ (black dots) and NN modeled $\Delta foF2$ ($\Delta foF2_{NN}$, red curve) for (a) Grahamstown, (b) Hermanus, (c) Louisvale, and (d) Madimbo during the storm period of 5-8 November 2001. The horizontal black dotted lines in the bottom panel of each graph represent the threshold of ±20 % established as quiet time variability.

Figure 6.4 shows the Dst index (red curve) on the top panel of each graph together with Kp index (black bars) to represent the storm occurrence date and time, and its magnitude. The minimum Dst index of -292 nT was observed on 6 November 2001 at 06:00 UT (e.g. Tsurutani *et al.*, 2004; Zhang *et al.*, 2007; Horvath and Lovell, 2008). Corresponding to this disturbance, the Kp index increased up to a maximum of 9 as seen in Figure 6.4. The development of the storm started on 5 November 2001 at ∼17:00 UT with a sudden increase in Dst index value

followed by a decrease in Dst index around 19:00 UT (Krankowski *et al.*, 2004; Maruyama *et al.*, 2004). The bottom panels of each graph in Figure 6.4 represent the actual $\Delta foF2$ (black dots) and NN modeled $\Delta foF2$ ($\Delta foF2_{NN}$, red curve) for (a) Grahamstown, (b) Hermanus, (c) Louisvale, and (d) Madimbo. During this storm period, there were no measurements for Hermanus and Madimbo as seen in Figures 6.4 (b) and (d), however, the modeled data was reproduced. The $\Delta foF2$ values around mid-night on 5-6 November 2001 indicate a short duration positive storm response, see Figures 6.4 (a) and (c). Similar remarks have been made by Krankowski *et al.* (2004) who observed the night time TEC enhancement after 19:00 UT over the European GPS stations.

A negative ionospheric response is observed on 6 November 2001 starting at ∼03:00 UT with $\Delta foF2$ values decreasing below ∼ -20%. This occurs following a negative interplanetary magnetic field (IMF) Bz event at ∼01:54 to ∼04:00 UT (Tsurutani *et al.*, 2004), which triggered the geomagnetic storm's main phase. The negative storm effect may be attributed to equatorward neutral winds (e.g. Buonsanto, 1999; Maruyama *et al.*, 2004). The ionospheric response during the storm period 5-8 November 2001 was analyzed at different latitude regions (e.g. Tsurutani *et al.*, 2004; Maruyama *et al.*, 2004; Krankowski *et al.*, 2004; Zhang *et al.*, 2007; Horvath and Lovell, 2008). For example, a decrease of ∼16% in total ionospheric TEC occurred at midlatitude and equator regions on 6 November 2001 (Tsurutani *et al.*, 2004). Krankowski *et al.* (2004) also observed a negative ionospheric storm effect, where TEC was depressed on 6 November 2001 at all latitudes over the European sector. The analysis by Maruyama *et al.* (2004) suggests that there were two competing factors determining the TEC variations during the storm period of 5-8 November 2001. One was a gradual increase in TEC, which started at ∼ 07:00 Japan Standard Time (JST = UT + 9) and was noticeable at higher latitudes. Then, an abrupt decrease in ΔTEC, which started at ∼ 08:00 JST. Where ΔTEC is the reference value subtracted from TEC on the storm day. Possible causes for the negative ionospheric storm effect observed over the Grahamstown and Louisvale stations may be due to thermospheric winds and neutral composition changes (Tsurutani *et al.*, 2004). It is well known that negative ionospheric storms at midlatitudes are largely caused by neutral composition changes (Mendillo *et al.*, 1970; Prölss, 1993a, 1995, and references therein). A study by Matamba *et al.* (2016) investigated the ionospheric response to four great geomagnetic storms (29 March to 2 April 2001, 27-31 October 2003, 18-23 November 2003, and 6-11 November 2004) over the African-European midlatitude sector. This study revealed that for the storms analysed, negative ionospheric responses were mainly associated with neutral composition changes. In both Figures 6.4 (a) and (c), the negative storm effect is observed from ∼ 03:00 UT reaching a minimum $\Delta foF2$ values at ∼ 06:00 UT on 6 November 2001. A negative storm response persisted for almost the entire day on 6 November 2001 except for around 16:00 - 18:00 UT over Grahamstown and around 12:00 - 18:00 UT for Louisvale station including the morning hours

until $\sim$ 06:00 UT on 7 November 2001. For both stations, the NN model is able to capture the negative response as determined by the negative values of $\Delta foF2$. In Figure 6.4 (a), the NN model in general, had a good estimate of the negative storm effects. However, the NN modeled $\Delta foF2$ over Louisvale was unable to capture the negative response observed $\sim$ 18:00 UT on 6 November 2001 to $\sim$ 06:00 UT on 7 November 2001. Although there were no measurements at Hermanus and Madimbo stations, the NN modeled $\Delta foF2$ is able to show negative storm responses on 6 November 2001 as seen in Figures 6.4(b) and (d).

Figure 6.5 represents the storm period of 19-24 November 2003, one of the greatest geomagnetic storms which occurred during the declining phase of solar cycle 23. This was due to a CME associated with a solar flare of magnitude X28 (Blanch *et al.*, 2005) observed on 18 November 2003. The speed of a CME near the Sun was recorded to be $\sim$ 1660 km/s (Gopalswamy *et al.*, 2005b). The top panel of each graph in Figure 6.5 indicates the Dst index (red curve) and Kp index (black bars). The storm's main phase occurred on 20 November 2003 with Dst index decreasing from -34 nT at 08:00 UT to a minimum value of -472 nT at 20:00 UT as seen in Figure 6.5. According to Loewe and Prölss (1997), this storm is classified as a great geomagnetic storm and is also reported in other studies (Blanch *et al.*, 2005; Gopalswamy *et al.*, 2005b; Yizengaw *et al.*, 2006; Matamba *et al.*, 2016, and references therein). The maximum Kp index of 9 was recorded. The bottom panel of each graph in Figure 6.5 shows $\Delta foF2$ (black dots) and $\Delta foF2_{\mathrm{NN}}$ (red curve) for (a) Grahamstown, (b) Hermanus, (c) Louisvale, and (d) Madimbo during the storm period 19-24 November 2003. During this storm period, Hermanus station was not yet operational, hence no actual $\Delta foF2$ values in Figure 6.5 (b). There is also a data gap for several hours during the main storm phase around 18:00 UT to $\sim$ 03:00 UT on 20-21 November 2003 over Grahamstown station, see Figure 6.5 (a). In Figure 6.5 (c), there are only a few actual $\Delta foF2$ data points available. A decrease in $\Delta foF2$ values below -20% at $\sim$ 18:00 UT on 20 November indicates the start of a negative ionospheric response which lasted through the whole day on 21 November 2003 as seen in Figure 6.5 (d). Where data was available, a negative storm effect is also observed on 21 November over Grahamstown and Louisvale, see Figures 6.5 (a) and (c). The NN model reproduced a negative ionospheric storm starting at $\sim$ 16:00 UT on 20 November in Figures 6.5 (a)-(d) as determined by $\Delta foF2_{\mathrm{NN}}$ values below -20%. In Figure 6.5 (a), the NN model was able to capture the negative storm response for almost the entire day on 21 November. Similar trend is seen in Figure 6.5 (b) where only the NN model data is available. A faster return to quiet time ionospheric variability of $\Delta foF2_{\mathrm{NN}}$ is noted in Figure 6.5 (c) at $\sim$ 12:00 UT on 21 November. The NN model over Madimbo station was unable to capture the negative storm response on 21 November 2003 as seen in Figure 6.5 (d), however the values of below -20% are observed only until $\sim$ 04:00 UT on 21 November 2003. Generally, similar response of the NN modeled data compared to the actual data is revealed for only few hours from $\sim$ 18:00 to 06:00 UT on 20-21 November 2003. The storm period 19-24
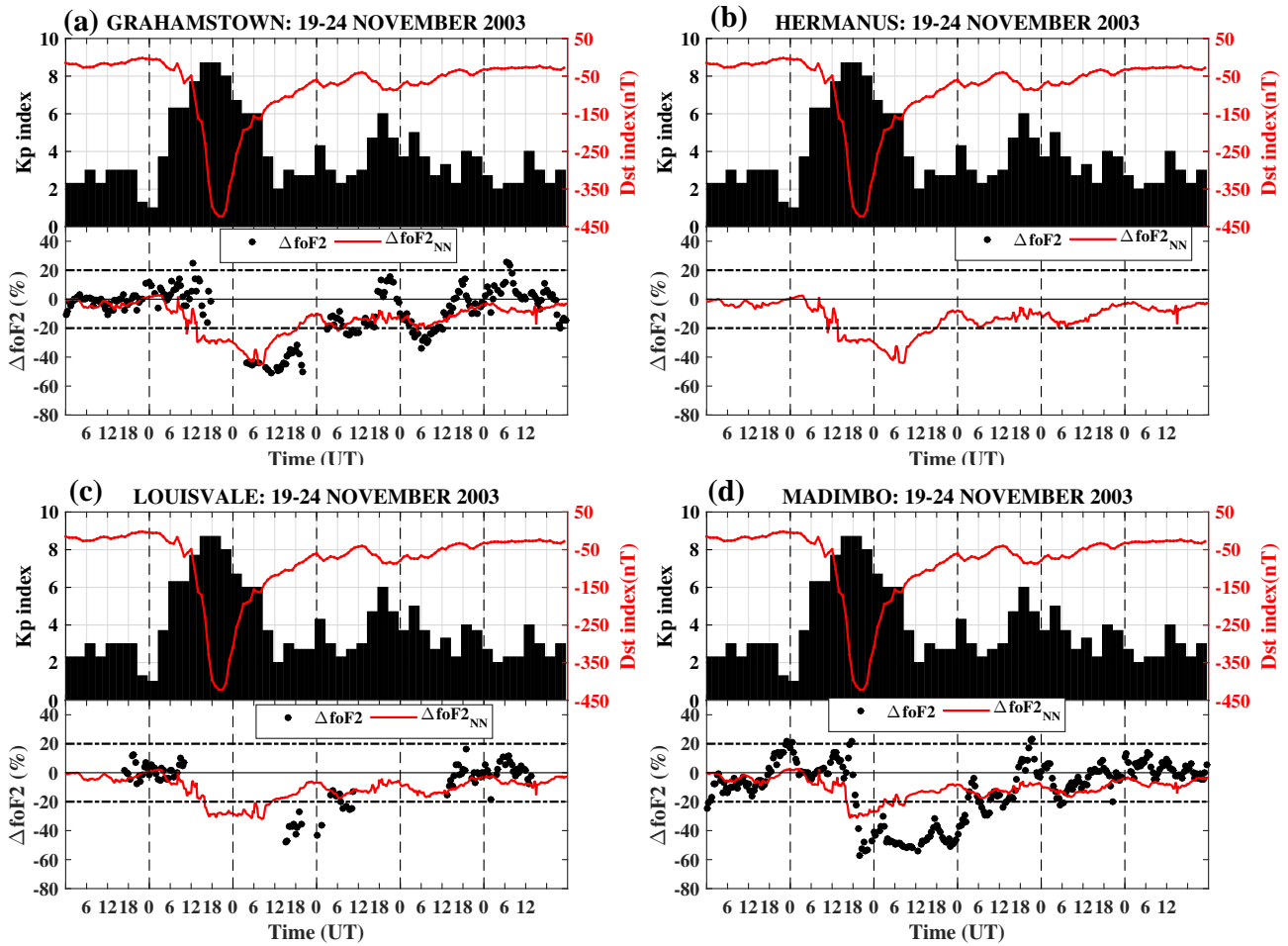
Figure 6.5: Similar to Figure 6.4 for the storm period of 19-24 November 2003.

November 2003 falls within the category of great geomagnetic storms. Looking at Figure 6.1, there is insufficient amount of data included in this storm category during model development, which means some of the mechanisms which are involved for this storm category are not well represented. This may be one of the probable reasons for the inability of NN model to capture some of the ionospheric responses.

The storm period of 7-12 November 2004 is presented in Figure 6.6 to assess how well the NN model performs compared to the actual measurements. The detailed description of the interplanetary characteristics during this storm period has been reported (Tsurutani *et al.*, 2008b; Echer *et al.*, 2010, and references therein). This storm was as a result of multiple CMEs associated with solar flares and was identified to have the most complex interplanetary structures due to the presence of multiple shocks and waves (Tsurutani *et al.*, 2008b; Echer *et al.*, 2010). Two consecutive main phases of geomagnetic storms are observed during this period as seen by the Dst index curve at the top panel of each graph in Figure 6.6. The first storm started on 7 November reaching a minimum Dst index of $\sim$ -374 nT around 07:00 UT on 8 November. During the recovery phase of the first storm, the second storm occurred in phases starting on
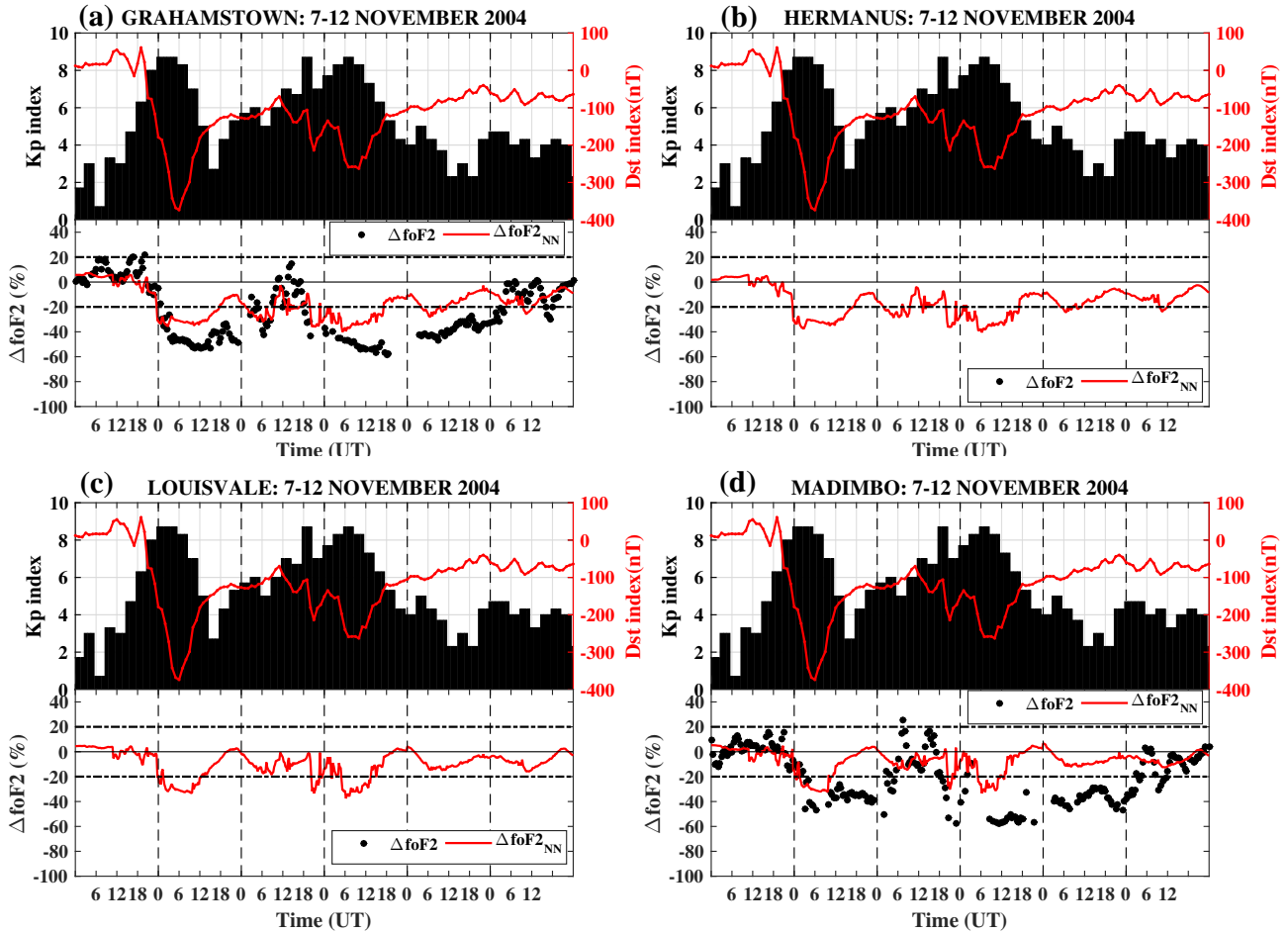
Figure 6.6: Similar to Figure 6.4 for the storm period of 7-12 November 2004.

9 November and reaching the peak minimum Dst index value of $\sim$ -263 nT on 10 November as seen in Figure 6.6. The Kp index increased to a maximum value of 9 on 8-10 November around the same time as the storm's main phases. The Hermanus and Louisvale stations do not have the measurements of $foF2$ during this storm period, see Figures 6.6 (b) and (c). A negative storm effect is observed on 8 November in response to the first main phase and lasted for the whole day. This was observed over Grahamstown and Madimbo stations which is demonstrated by negative values of $\Delta foF2$ (black dots) as shown in Figures 6.6 (a) and (d). Similar response is observed on 10-11 November following the second storm main phase. The ionospheric storm response during this period over the South African midlatitude stations is also reported by Habarulema *et al.* (2013); Matamba *et al.* (2016). In the study by Habarulema *et al.* (2013), it was revealed that the negative storm effects on 8 and 10 November 2004 as observed by TEC data agrees with the corresponding reduction in the oxygen to nitrogen (O/N_2) ratio. This is considered to be the predominant cause of the decrease in electron density over midlatitude regions during geomagnetic storms. On the 9 November, both negative and slight positive storm effects are noted over Madimbo as shown in Figure 6.6 (d). Considering the model's performance over Grahamstown in Figure 6.6 (a), the NN model could reproduce the

104

negative storm effects observed on 8-10 November 2004. At Madimbo station, between 8-10 November, $\Delta foF2_{\text{NN}}$ negative storm effects transpire for a shorter period when compared to $\Delta foF2$. Indeed, on the 8 November 2004, $\Delta foF2$ lasted the whole day below -20% while $\Delta foF2_{\text{NN}}$ only persisted from $\sim$00:00 - 12:00 UT as seen in Figure 6.6 (d). Further, during the recovery phase on 11 November 2004, the NN model failed to represent the negative storm effects. The $\Delta foF2_{\text{NN}}$ over Grahamstown during the same period observed a negative response only for a short time around 06:00 UT. Although there were no measurements over Hermanus and Louisvale stations, the $\Delta foF2_{\text{NN}}$ is able to represent similar negative storm responses as the other two stations. This is shown by the negative $\Delta foF2_{\text{NN}}$ values below -20% threshold for several hours on 8 and 10 November 2004 in Figures 6.6(b) and (c). Overall, the model is capable of capturing most of the negative storm effects during the November 2004 storm period.

The December 2015 storm which occurred during the solar cycle 24 was also considered for a regional NN model validation and is presented in Figure 6.7. This CME-driven storm was associated with a C6 solar flare which occurred on 16 December 2015 (e.g. Cherniak and Zakharenkova, 2018). A minimum Dst index of $\sim$ -155 nT was recorded around 22:00 UT on 20 December 2015. This is classified according to Loewe and Prölss (1997) as a strong geomagnetic storm. A maximum Kp index of 7 was also observed on 20-21 December 2015 around 19:00 and 01:00 UT respectively, see the top panel of each graph in Figure 6.7. Other studies also analyzed the impact of this storm using ground-based and satellite datasets at different latitude regions (Chashei *et al.*, 2016; Blagoveshchensky *et al.*, 2018; Cherniak and Zakharenkova, 2018; Mansilla, 2019; Morozova *et al.*, 2019, and references therein). The initial phase started on 19 December with Dst index values increasing to a maximum of 43 nT $\sim$ 22:00 UT. This sudden increase in Dst index values is also known as the sudden storm commencement. As seen at the top panel of each graph in Figure 6.7, a decrease in Dst index values from $\sim$ 22:00 UT on 19 December to a minimum value of $\sim$ -155 nT around 22:00 UT on 20 December is an indication of the storm's main phase which lasted for $\sim$24 hours. The actual $\Delta foF2$ (black dots) and NN modeled $\Delta foF2_{\text{NN}}$ (red curve) are presented at the bottom panel of each graph in Figure 6.7. There is missing data during initial, main, and part of recovery phase of the storm (19-21 December 2015 around 08:00 UT) for actual $\Delta foF2$ over Madimbo station, see Figure 6.7 (d). Considering actual $\Delta foF2$ on 19 December 2015, there are positive storm effects around 06:00 UT and 19:00 UT over Grahamstown and Hermanus in Figures 6.7 (a) and (b) respectively. The possible effect may be the occurrence of pre-storm enhancements which are considered to be strong for $\Delta foF2$ greater than 20% (Burešová and Laštovička, 2007). However, these positive storm effects are not observed over Louisvale station, see Figure 6.7 (c). An enhancement in maximum electron density of the F2 layer (NmF2) which has sometimes been observed few hours to a day before the onset of geomagnetic storm is known as pre-storm enhancement (Burešová and Laštovička, 2007). Another positive storm response is observed on 20 December
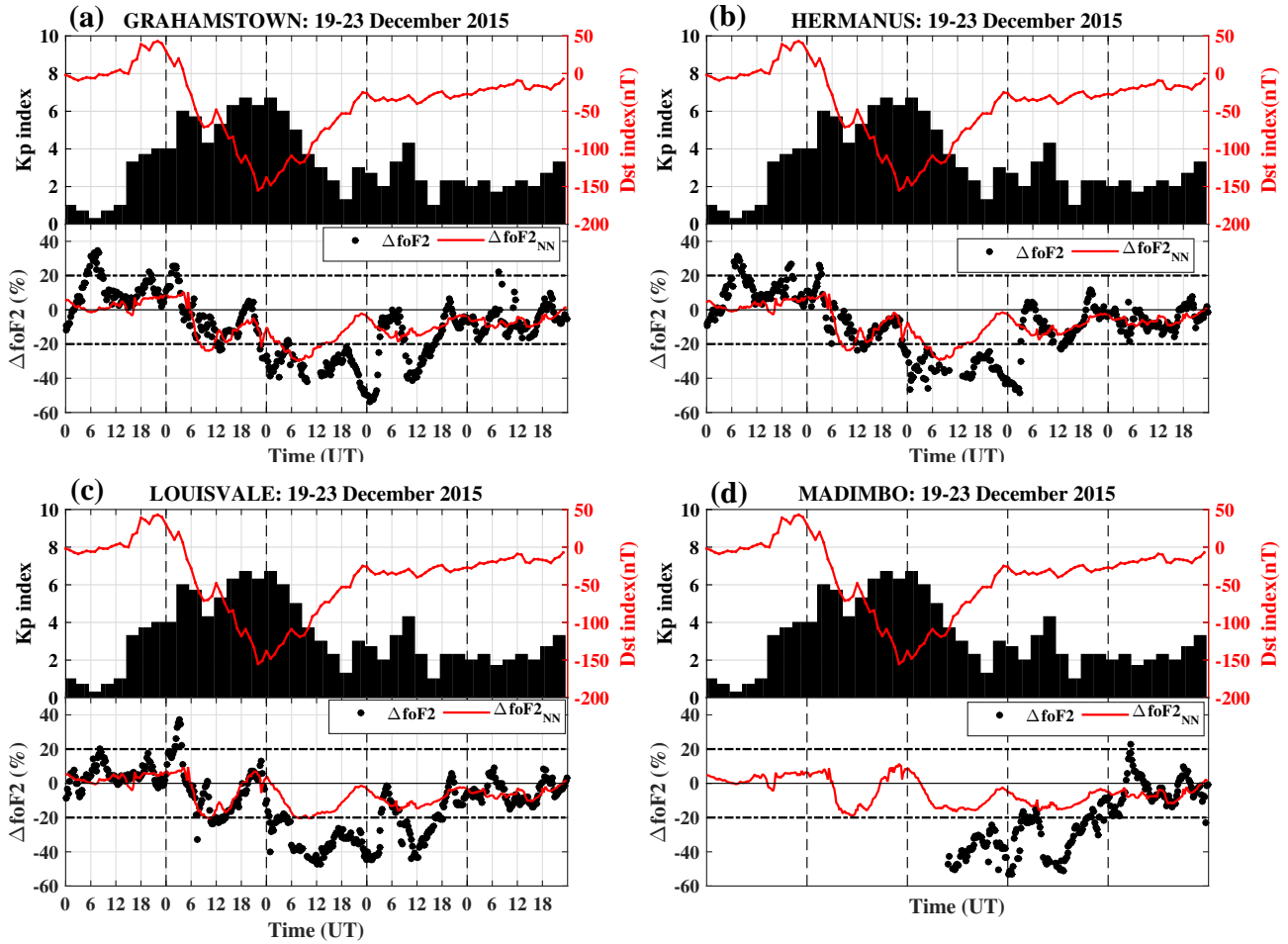
Figure 6.7: Similar to Figure 6.4 for the storm period of 19-23 December 2015.

at ∼03:00 UT over the three stations as shown in Figures 6.7 (a) - (c). This was followed by a negative storm effect later around 12:00 UT. A stronger negative storm response is observed on 21 December through to 22 December 2015 before returning to quiet time variability. This is consistent with other studies, (e.g. Cherniak and Zakharenkova, 2018) which reported the signatures of negative storm phase at midlatitudes as indicated by the plasma density measurements. The NN model was able to capture the negative storm response on 20 December during the storm main phase over Grahamstown and Hermanus stations. However, the model predicted the response earlier that the actual response at both stations, see Figures 6.7 (a)-(c). During the recovery phase on 21 December, the model predicted the negative response for a shorter period of time (∼ 04:00-12:00 UT) compared to the actual $\Delta foF2$ at both stations. This is not the case over Louisvale and Madimbo (Figures 6.7 (c)-(d)), where the values of $\Delta foF2_{NN}$ were mostly within ±20% during the entire storm period although the trend is noticeable. It appears that the model performs well for typical midlatitude locations, but fails towards mid-low latitude stations. The Louisvale and Madimbo stations are located more towards the low latitude and different mechanisms may be influencing the ionospheric responses over these locations. One of the mechanisms that is well known to originate from the equatorial

region and contributes to positive ionospheric storm effect at midlatitudes is the expansion of the equatorial ionization anomaly (EIA) (Prölss, 1993a; Balan *et al.*, 2010; Ngwira *et al.*, 2012; Katamzi and Habarulema, 2014; Matamba *et al.*, 2016, and references therein). For example, the study by Katamzi and Habarulema (2014) confirms the expansion of EIA towards the African midlatitude regions during the 28-31 October 2003 storm. The observations were based on the presented global IONosphere EXchange (IONEX) TEC maps at 10:00 and 12:00 UT during the storm period 28-31 October 2003. The analysis by Matamba *et al.* (2016) suggests that the cause for pronounced positive ionospheric storm effects were due to the expansion of EIA. This was done during the four great geomagnetic storms, 29 March to 2 April 2001, 27-31 October 2003, 18-23 November 2003, and 6-11 November 2004, at midlatitude regions. Overall, the presented results indicate that although the $\Delta foF2$ trend is reproduced, the model fails to capture most of the negative responses during this storm period.

6.3.2   Validation results at GPS locations

The regional NN model is also validated at randomly selected GPS locations within the region. The actual $\Delta foF2$ presented in this section is based on TEC data using the developed equations which are described in chapter 5. The important information to recall from chapter 5 is that, the monthly median $foF2$ derived from GPS TEC over each co-location can be used to compute $\Delta foF2$ at any other GPS location within the IPP coverage area of each ionosonde location. To demonstrate the NN model's performance at GPS locations, two storm periods 7-12 November 2004 and 19-23 December 2015 are considered over four GPS locations: George ($42.3°S$), Ladysmith ($38.5°S$), Phalaborwa ($34.6°S$), and Springbok ($39.0°S$) geomagnetic latitude (GMLAT). Figure 6.8 represents the two subsequent geomagnetic storms which occurred during the period 7-12 November 2004 with Dst index of $\sim$ -374 nT and -263 nT on 8 and 10 November respectively. An enhancement is observed during the main phase of the first storm over Springbok as seen in Figure 6.8 (b) at $\sim$ 00:00 - 04:00 UT on 8 November 2004. Another positive storm effect occurred during the second storm's main phase on 10 November 2004 at $\sim$ 03:00 - 06:00 UT, see Figures 6.8 (a), (b), and (d). The decrease in $\Delta foF2$ was predominantly below -20% on 8 November 2004 at all four stations as reported in other studies (e.g. Habarulema *et al.*, 2013; Matamba *et al.*, 2016). The NN modeling results also shows a negative storm response for several hours as shown in Figures 6.8 (a)-(d). During the recovery phase of the first storm, 9 November 2004, the values of $\Delta foF2$ were varying mostly within $\pm20\%$ although there were occasions of negative storm responses observed. The ionospheric responses to the second main phase were generally negative storm effects on 10-11 November as seen in Figures 6.8 (a)-(d). The NN model was able to capture the negative storm response for most hours on 10 November 2004 at all four stations but fails to do so on 11 November 2004.
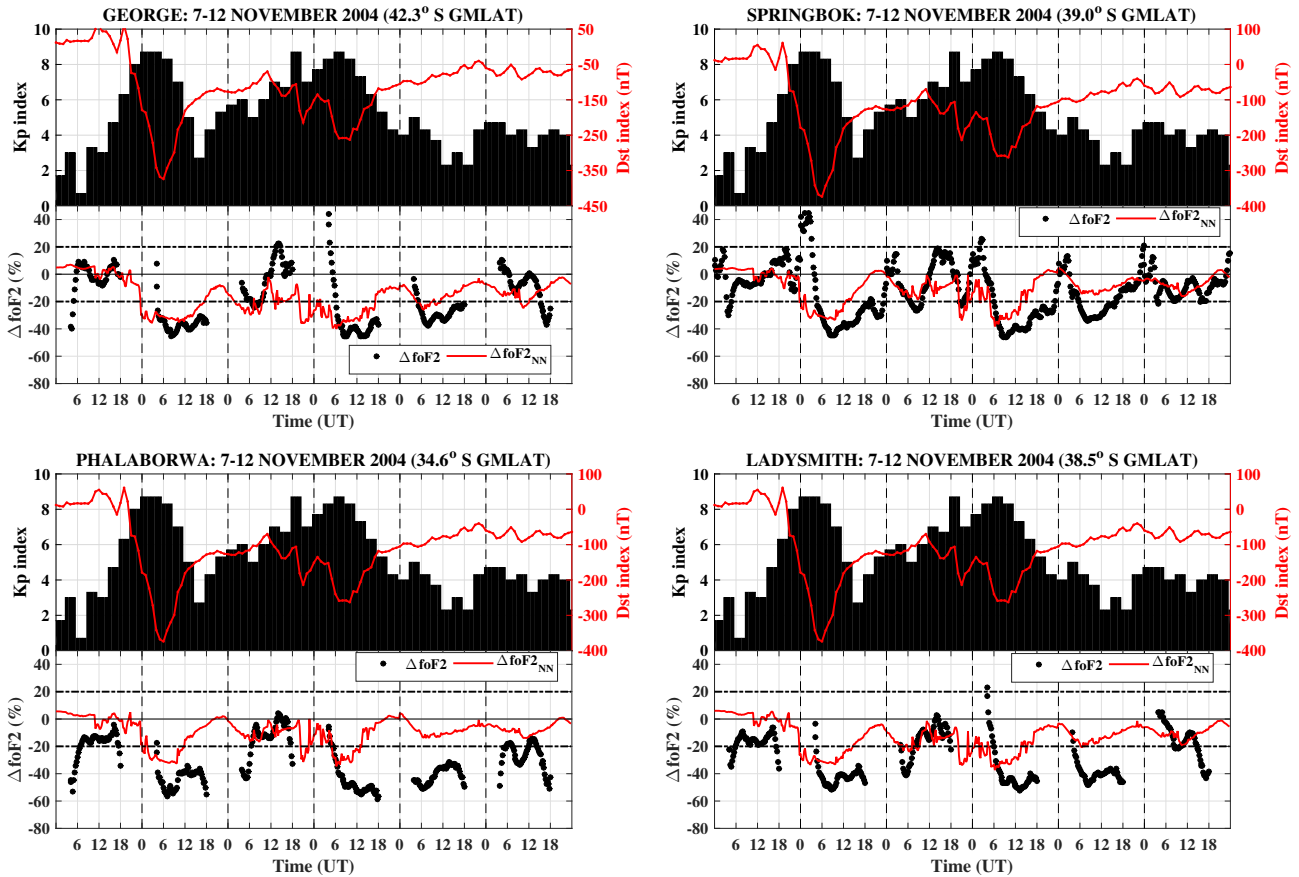
Figure 6.8: The Dst index (red curve) is plotted on the top panel of each graph together with Kp index (black bars) to represent the storm occurrence date and time, and its magnitude. The bottom panel of each graph shows the actual $\Delta foF2$ (black dots) and NN modeled $\Delta foF2$ ($\Delta foF2_{\mathrm{NN}}$, red curve) for (a) George, (b) Springbok, (c) Phalaborwa, and (d) Ladysmith during the storm period of 7-12 November 2004.

Figure 6.9 is similar to Figure 6.8 for the storm period 19-23 December 2015 representing the model's performance during this period. An increase in $\Delta foF2$ is observed on 20 December 2015 at ~00:00 - 05:00 UT for all stations except Springbok. This is during the occurrence of the geomagnetic storm's main phase. Later on the same day, a short duration negative storm response is observed around 22:00 UT over the three stations: Springbok, Phalaborwa, and Ladysmith. Another positive storm effect on 21 December at ~03:00 UT over Phalaborwa and Ladysmith stations is observed, as indicated by $\Delta foF2$ greater than 20% in Figures 6.9 (c) and (d). Figures 6.9 (a)-(d) indicate that a negative storm response was observed at all stations for several hours on 21 December around 09:00 - 23:00 UT, during the recovery phase of the geomagnetic storm. The general trend of the ionospheric storm response is relatively well predicted by the NN model although mostly $\Delta foF2_{\mathrm{NN}}$ varies within ±20%. Thus, the model fails to predict most of the responses during this storm period. However, the model was able to predict, for several hours, the negative storm response which occurred on 21 December over George.
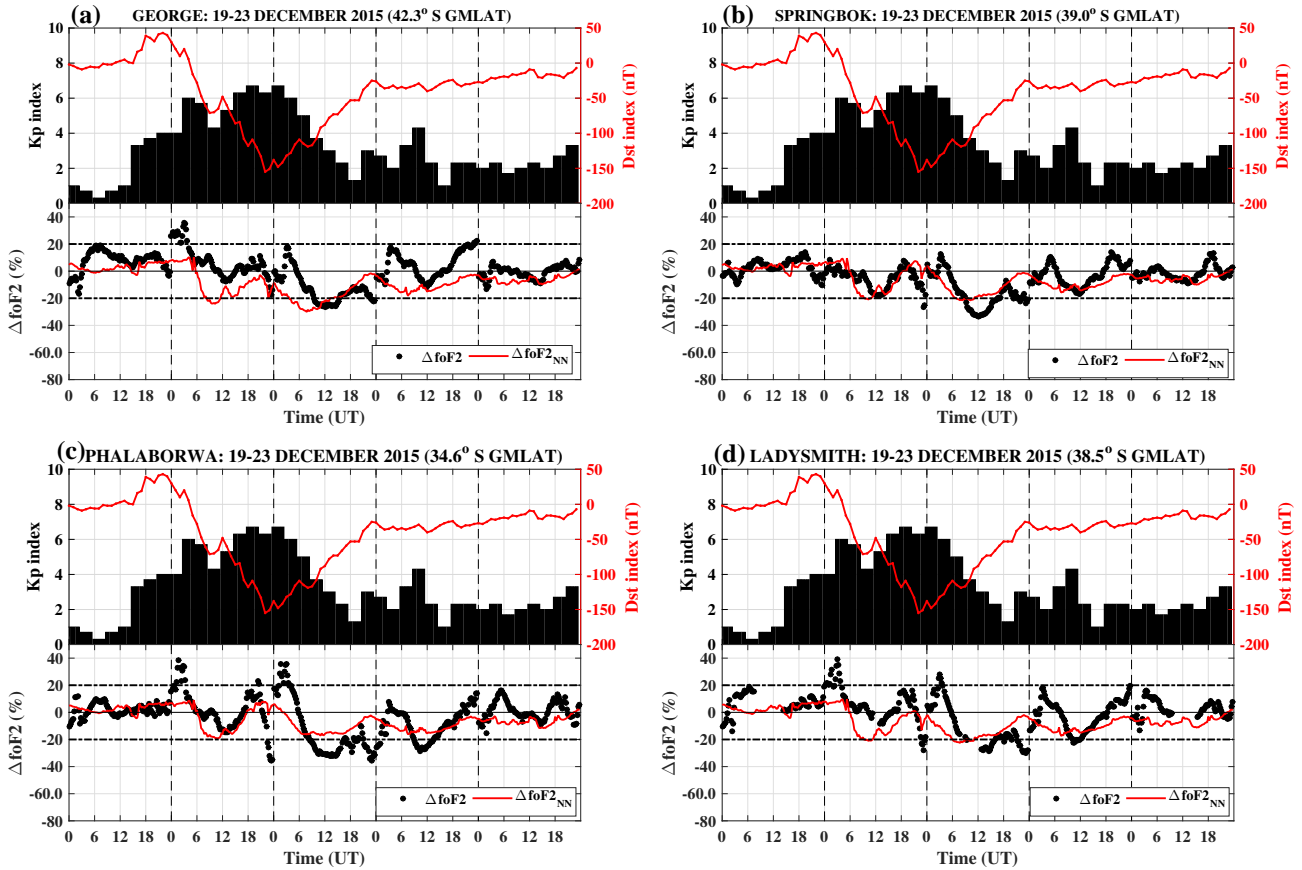
Figure 6.9: Similar to Figure 6.8 for the storm period of 19-23 December 2015.

6.4   Analysis of the model's performance

The accuracy of the NN regional model is evaluated based on root mean square error (RMSE) and correlation coefficient (R). The two statistical measures are commonly used for model assessment (e.g. Zhang *et al.*, 2011; Habarulema and McKinnell, 2012; Uwamahoro *et al.*, 2018b, and reference therein). The computation was done between actual and modeled $\Delta foF2$ over the four ionosonde stations during storm period 5-8 November 2001, 19-24 November 2003, 7-12 November 2004, and 19-23 December 2015. Figure 6.10 (a) shows the RMSE values over Grahamstown, Hermanus, Louisvale, and Madimbo represented in blue, orange, purple, and green bars respectively for the presented storm periods. Similarly, Figure 6.10 (b) indicates the correlation coefficient values. The statistical analysis over Hermanus is done for only December 2015 storm since the ionosonde station became operational in 2009. Considering the Grahamstown station in Figure 6.10 (a), the RMSE values ranges between ∼13-16%. The storm period 19-24 November 2003 has the lowest RMSE value of 13%. The Louisvale station shows the smallest value of 11% during the November 2001 storm period. Similar analysis could not be performed for Hermanus station since the available data covered only one storm period. The Madimbo station shows higher RMSE values during the three storm periods compared to other stations. These large RMSE values could be due to the fact that the ionospheric response at
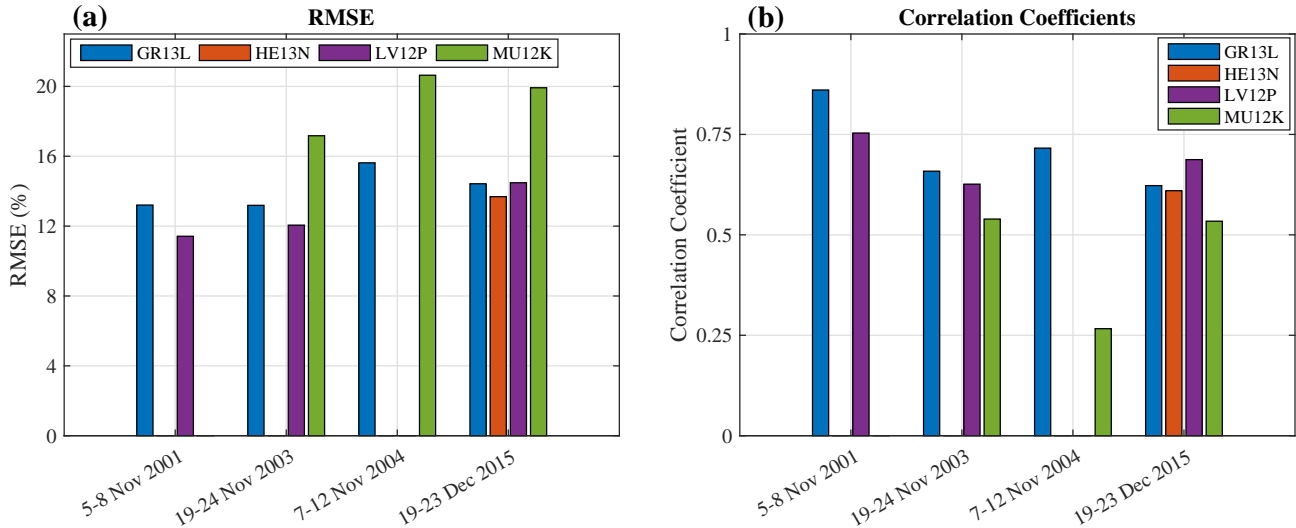
Figure 6.10: The RMSE and correlation coefficient values between actual and NN modeled $\Delta foF2$ over four locations (GR13L, HE13N, LV12P, and MU12K in blue, orange, purple, and green respectively) during the storm periods 5-8 November 2001, 19-24 November 2003, 7-12 November 2004, and 19-23 December 2015.

this station is not always the same as the other stations. The Madimbo station is located more towards the low latitude and some responses may be influenced by the equatorial ionization anomaly (EIA). Thus, it is known that during geomagnetic storms, the expansion of the EIA is one of the causes of positive ionospheric storms at mid-latitude regions (e.g. Prölss, 1993a). A storm of 6-11 September 2017 showed similar features for Madimbo with higher increase in $foF2$ compared to the other three ionosonde stations over South Africa (Habarulema *et al.*, 2020). Another possible factor may be due to the amount of data used in modeling over this location, as presented in Figure 6.1. A significant data gap exists during the medium to high solar activity period of solar cycle 24 for Madimbo station from mid 2012 to end of 2015. It is known that empirical modeling doesn't reproduce most features when there is little data over a particular location (e.g McKinnell and Poole, 2004a; Bilitza and Reinisch, 2008; Uwamahoro *et al.*, 2018b). On average, the RMSE values are 12%, 14%, 18%, and 16% for 2001, 2003, 2004, and 2015 storm periods respectively. The results are comparable to those presented in Tshisaphungo *et al.* (2018) for a single station model over Grahamstown station. The RMSE values obtained for 2001 and 2015 storm periods are respectively 11.33% and 15.77%. However the 2004 storm period has lower RMSE value of 15.30% as compared to 18% for the regional model. Based on the lowest RMSE value in general, the NN model performs reasonably well during the storm period 5-8 November 2001 compared to the other storm periods presented. The correlation coefficient values were also computed for the same storm periods over the four stations, see Figure 6.10 (b). The correlation coefficient over Grahamstown ranges between 0.62 - 0.86 where the highest value is obtained during the November 2001 storm. Most of the correlation coefficient values for all storms considered are greater than 0.5 except for the 2004

storm over Madimbo station which recorded the value of 0.27. Similar to the RMSE analysis, the Madimbo station appears to have the lower values of correlation coefficient in comparison with the other stations. Hence, poor performance of the NN model is noticed over this particular station.

The statistical analysis of the NN model is also validated over the GPS locations during the storm periods 7-12 November 2004 and 19-23 December 2015. Table 6.2 represents the RMSE and R values computed between actual and NN modeled $\Delta foF2$ over the GPS locations. The

Station		RMSE		R	
Name	Code	2004	2015	2004	2015
George	GEOA	15.94	13.77	0.55	0.53
Springbok	SBOK	17.87	8.70	0.35	0.57
Phalaborwa	PBWA	24.77	12.37	0.43	0.54
Ladysmith	LSMH	19.47	13.45	0.46	0.47

Table 6.2: The RMSE and correlation coefficient (R) values between actual and NN modeled $\Delta foF2$ over the four GPS locations during the storm periods 7-12 November 2004 and 19-23 December 2015.

RMSE values during the November 2004 storm ranges from $\sim$ 16-25% with lowest value obtained over the George station. The December 2015 storm has lower values of RMSE which ranges from $\sim$ 9-14% as compared to the November 2004 storm. On average, the RMSE value for the December 2015 storm is 12% compared to 20% for the November 2004 storm period. Comparing to the performance results over the ionosonde stations, 2004 storm has higher average RMSE value. During 2015 storm period, the average RMSE value over GPS stations is lower compared to results over the ionosonde stations. The Springbok station has the lowest RMSE value of 9% during December 2015 storm, which indicates that the model performs reasonably well with reference to other stations. The R values for both 2004 and 2015 storm periods are also presented in Table 6.2 where on average correlation coefficients of 0.45 and 0.53 is respectively achieved. The highest R values of 0.55 and 0.57 are obtained during November 2004 over George and December 2015 over Springbok respectively. The overall R values over GPS locations are slightly lower that over the ionosonde stations. This may be because the NN model development is based on $foF2$ measurements only over the ionosonde locations. Another possible reason for slightly lower R values over the GPS locations as compared to ionosonde locations, may be that the GPS derived $foF2$ is based on TEC data. Although a strong correlation exists between $foF2$ and TEC (Kouris *et al.*, 2004; Ssessanga *et al.*, 2014; Otugo *et al.*, 2019; Pignalberi *et al.*, 2019), there are some limitations to consider which may result in inaccuracies of the model's performance. One of the limitations is the large differences observed during night time (Ssessanga *et al.*, 2014; Pignalberi *et al.*, 2019), which is also presented in Figure 5.3 of Chapter 5 under section 5.2.1. The possible cause of night time

differences between $foF2$ and TEC may be the plasmasphere contribution to TEC data (e.g. Klimenko *et al.*, 2017; Li *et al.*, 2018). The study by Klimenko *et al.* (2017) suggests that, the regions above the F2 layer peak height provide the largest plasmaspheric contribution to TEC which has been observed to be more pronounced during night-time. In addition, the ionosphere and the plasmasphere undergo very rapid changes during dawn/dusk as a result of solar terminator (e.g. Pignalberi *et al.*, 2019), which is another possible reason for $foF2$ and TEC night time deviations. The inclusion of GPS locations in the model development may increase the performance as well as improve the spatial resolution of the model.

6.5 Summary and conclusion

The regional modeling of the ionospheric storm-time $foF2$ response based on artificial neural networks (ANNs) over the South African mid-latitude region is described. The data coverage used in the model development over the four ionosonde stations is Grahamstown (1996 - 2016), Hermanus (2009 - 2016), Louisvale (2000 - 2016), and Madimbo (2000 - 2016). The selection criteria for the storm-time $foF2$ data was based on Dst $\leqslant$ -50 nT and Kp $\geqslant$ 4. The NN regional modeling results were compared with the actual $\Delta foF2$ over the ionosonde and GPS locations for selected storm periods. The presented results revealed that, overall, the NN model is capable of capturing most of the negative storm responses and fails to do so for most positive storm responses which are known to have more unpredictable features (Tsagouri *et al.*, 2000). It was also shown that the NN model performs more adequately over the ionosonde locations as opposed to the GPS locations. The presented model forms a basis of a regional ionospheric storm-time index which will provide a prompt evaluation of a posistive or nagative ionospheric storm effects over a particular region. The observational input parameters into the model will allow for a near real-time monitoring of the ionospheric responses to geomagnetic storms. This eventually makes such an index suitable for the space weather operational environment and important service to HF communication users.

Chapter 7

Summary, Conclusions, and Future work

This study focuses on the modeling of the ionospheric $foF2$ response to geomagnetic storm activity over the South African region. This is denoted by $\Delta foF2$ which is the deviation of daily $foF2$ from the respective monthly median values. A database of $\Delta foF2$ measurements during geomagnetic storm occurrences (Dst $\leqslant$ -50 nT & Kp $\geqslant$ 4) has been created for model development. Thus, this study was based only on storm-time $foF2$ data for both the development and validation of the model. The data used to develop and validate storm-time model was obtained from a network of ionosondes and GPS receiver stations over the South African region. Artificial neural networks (ANNs) were used to execute the main objective of this study, while other modeling techniques such as linear regression were also explored. General observations and findings are summarized in the next section.

7.1 Summary and conclusion

The ionosphere is known to play an important role in radio wave propagation among other functions. Because of its role as an ionized layer and its variability especially during geomagnetic storms, ionospheric studies and its applications remain a key area of research (e.g. Danilov, 2001, 2013; Cander, 2015; Habarulema *et al.*, 2017; Heelis and Maute, 2020). Since the ultimate goal of this study is to develop a regional ionospheric storm-time index, the understanding of different mechanisms that drive the ionospheric responses during geomagnetic storm is crucial. Although extensive effort has been undertaken (e.g. Cander and Mihajlovic, 1998; McKinnell and Poole, 2004a,b; Habarulema *et al.*, 2009, 2011; Okoh *et al.*, 2010; Uwamahoro and Habarulema, 2015; Uwamahoro *et al.*, 2018b), ionospheric modeling remains a challenge due to the complex processes within the ionosphere especially during storm conditions (Cander, 2015). The dynamics and challenges of storm-time ionospheric responses are the key factors of this research focus. Although modeling efforts have been previously done over the South

African region (McKinnell and Poole, 2004a,b; Habarulema *et al.*, 2009, 2011; Okoh *et al.*, 2010; Ssessanga *et al.*, 2014; Uwamahoro and Habarulema, 2015), the current work is an attempt towards the development of a regional ionospheric storm-time index based on $foF2$ data, which complements and supplements existing models for the region. It is important to develop a model that can capture ionospheric storm effects during geomagnetic storms, with the main aim of developing a regional ionospheric storm-time index. This index will be key in an operational space weather environment, providing a quick evaluation and measure of the complex ionospheric conditions (Stankov *et al.*, 2002; Jakowski *et al.*, 2006, 2012). To be able to achieve the main objective of this research, different approaches such as single station modeling, estimating $foF2$ data from GPS TEC and then expanding the study to cover the regional aspect have been explored.

A single station model of ionospheric critical frequency of the F2 layer ($foF2$) response to geomagnetic storms was done over Grahamstown station. This study was done to evaluate how well the modeling techniques perform over a particular station before expanding to cover the region. Of the four South African ionosonde stations, Grahamstown has the longest data set and therefore was considered for this analysis. The neural network (NN) and linear regression (LR) techniques were applied in developing a single station model during only geomagnetic storm conditions for the period 1996-2014. Due to different processes affecting the ionospheric responses during a storm, three geomagnetic indices were considered: (i) the symmetric disturbance field in the horizontal (H) component of the Earth's magnetic field ($SYM - H$), (ii) the Auroral Electrojet (AE) index, and (iii) the local geomagnetic A index. The $SYM - H$ index was found to have the largest contribution of 41% and 54% based on NN and LR techniques respectively (Tshisaphungo *et al.*, 2018). The NN and LR models were validated for the storm periods which occurred within and outside the period of the models' development (interpolation and extrapolation storms respectively). The correlation coefficient for both models when validating interpolation storms was 0.8 on average. A correlation coefficient value of 0.6 for NN model as compared to 0.5 for LR model was obtained for extrapolation storms. It is important to recall that during this investigation, the use of annual and semi-annual components was adopted from the work of Zhang *et al.* (2011) which resulted in an improved performance of LR model. It has been shown that NN and LR models are capable of capturing most of the ionospheric responses during geomagnetic storms presented, however, both models were unable to capture short term features mostly observed as positive enhancements which are known to be unpredictable (Tsagouri *et al.*, 2000). Although there are shortcomings associated with NN and LR modeling the results give adequate agreement with observational data in identifying the resulting ionospheric response as a result of storms. Before this study was expanded to include data from the other three ionosonde stations, an estimation of $foF2$ from GPS TEC was explored with the idea of increasing the spatial data coverage of ionosonde data. The idea

came about because it is well known that GPS TEC and $foF2$ data are highly correlated (e.g. Kouris *et al.*, 2004; Ssessanga *et al.*, 2014; Pignalberi *et al.*, 2019).

The relationship between $foF2$ and GPS TEC was obtained based on only storm-time dataset from 2003-2016 using polynomial functions. The mathematical expressions were derived over each ionosonde location and used to estimate $foF2$ from GPS TEC. The computation was performed over and within the IPP coverage area of each ionosonde location. Since the main objective is to be able to model the negative and positive storm effects based on $\Delta foF2$ parameter, the use of monthly median $foF2$ data over GPS locations was carefully considered. The use of ionosonde monthly median $foF2$ over GPS locations resulted in large errors between the actual and modeled $\Delta foF2$. Hence, separate mathematical expressions to obtain monthly median $foF2$ from GPS TEC were developed at ionosonde-GPS co-locations. The results of the actual and modeled $\Delta foF2$ were compared for selected storm periods: 4-8 August 2011, 6-14 March 2012, 6-10 May 2016, and 6-11 September 2017 at co-located stations and within the IPP coverage area of each ionosonde location. The average RMSE and R values of 12.06 % and 0.67 respectively for all stations were obtained which is comparable to other studies (e.g. Ssessanga *et al.*, 2014; Pignalberi *et al.*, 2019). Because there are other GPS locations which are outside the IPP coverage area, an evaluation using an independent dataset from COSMIC was used to validate the modeled $foF2$ with actual measurements. The validation was done during the storm period of 4-8 August 2011 over five GPS locations. The results showed high correlation coefficient values of more than 0.9 at all locations. The RMSE values range between 0.8 and 1 MHz which is consistent with other studies over the same mid-latitude region (e.g. Habarulema *et al.*, 2014). These results give some level of confidence that the modeled $foF2$ from GPS TEC data may be applied in the development of a regional ionospheric storm-time index with higher spatial coverage of $foF2$ data.

To pursue the objective of this thesis, the single station modeling was expanded to include other ionosonde stations to develop a regional model that can capture $\Delta foF2$ deviation. The data coverage for this model development is Grahamstown (1996 - 2016), Hermanus (2009 - 2016), Louisvale (2000 - 2016), and Madimbo (2000 - 2016). The regional model development was also based on NN technique. The NN regional modeling results were compared with the actual $\Delta foF2$ over the ionosonde and GPS locations for selected storm periods. The presented results revealed that, in general, NN model is capable of capturing most of the negative storm responses and fails to do so for most positive storm responses. It was also shown that the NN model performs more adequately over the ionosonde locations as opposed to the GPS locations. Therefore, the work in this thesis provides a foundational regional ionospheric storm-time index model upon which future versions can be built. The model will be a valuable tool within the operational space weather environment.

7.2　Future work

Although extensive efforts have been made towards improvement of ionospheric modeling (Fuller-Rowell *et al.*, 2000a; Mukhtarov *et al.*, 2013a, and references therein), several challenges related to storm-time ionospheric modeling have been reported. For example, the inaccuracies of empirical models to capture positive or negative ionospheric responses during storm conditions has been reported (e.g. Fuller-Rowell *et al.*, 2000a; Habarulema *et al.*, 2010). Another element includes the availability of reliable data for a specific region which can determine the accuracy of the model (Zhang *et al.*, 2011; Habarulema *et al.*, 2011; Uwamahoro and Habarulema, 2015; Uwamahoro *et al.*, 2018b). One of the considerations to enhance this study is to increase the spatial data coverage for model development which may improve its performance. Two options have been explored in this study, namely the use of GPS TEC data to estimate $foF2$ and radio occultation (RO) data. Studies exist that compares RO data with ionosonde, GNSS and other data sources over different regions (e.g. Chu *et al.*, 2010; Liu *et al.*, 2011; Habarulema *et al.*, 2014; Habarulema and Carelse, 2016). The use of RO data to complement the ionosonde data can be an important factor to take into consideration for future investigation for model improvement. For example, the study by Habarulema and Carelse (2016) provides us with confidence in using RO data as an independent validation dataset in the absence of ionosonde data. Since GPS derived TEC has been shown to be highly correlated to ionosonde $foF2$ measurements (e.g. Kouris *et al.*, 2004; Ssessanga *et al.*, 2014; Pignalberi *et al.*, 2019), this data source will also be a valuable addition to increase the spatial resolution, for an improved regional model development.

Other studies have shown that the $foF2$ response to geomagnetic storms experiences some time delay (Muhtarov and Kutiev, 1998; Kutiev and Muhratov, 2001; Kutiev and Muhtarov, 2003; Liu *et al.*, 2010, and references therein). Statistical analysis documented in Kutiev and Muhratov (2001) shows that there is a delay of ionospheric response to geomagnetic storm. The time delay may be due to different factors including magnetic latitude and local time (Liu *et al.*, 2010) which depends on the sudden storm commencement. The time delay of the ionospheric response to geomagnetic storm which is dependent on the onset time of the storm will be investigated in future. This may be carried out by categorizing the storms according to storm onset time.

In addition, the physical mechanisms causing the ionospheric storm effects during geomagnetic storm conditions at different latitude regions are some of the major challenges in modeling. Such mechanisms include neutral composition changes (Prölss *et al.*, 1991; Prölss, 1995; Fuller-Rowell *et al.*, 1994), prompt penetration electric field (PPEF) (Tsurutani *et al.*, 2004), and more. The representation of some of these mechanisms within the model development is important to

ensure that most features are captured within the model. One of the processes that originate from the equator is the expansion of the equatorial ionization anomaly (EIA) and is known to be a contributing factor for positive ionospheric storm effects in mid-latitude regions (e.g. Balan *et al.*, 2010; Ngwira *et al.*, 2012; Katamzi and Habarulema, 2014; Matamba *et al.*, 2016). Generally, the results presented in this research revealed that most positive ionospheric storm effects were not successfully captured by the model. Investigating an appropriate parameter that can be included in the model development to represent the effect of EIA may improve the model in capturing the positive storm responses.

References

Aa E., Huang W., Liu S., Ridley A., Zou S., Shi L., Chen Y., Shen H., Yuan T., Li J. *et al.*, "Midlatitude plasma bubbles over China and adjacent areas during a magnetic storm on 8 September 2017", *Space Weather*, **16**(3), pp. 321–331, doi:10.1002/2017SW001776, 2018.

Adewale A., Oyeyemi E., Adeloye A., Ngwira C. and Athieno R., "Responses of equatorial F region to different geomagnetic storms observed by GPS in the African sector", *Journal of Geophysical Research: Space Physics*, **116**(A12), 2011.

Adewale A., Oyeyemi E., Cilliers P., McKinnell L. and Adeloye A., "Low solar activity variability and IRI 2007 predictability of equatorial Africa GPS TEC", *Advances in Space Research*, **49**(2), pp. 316–326, 2012.

Ahoua S.M., Habarulema J.B., Obrou O.K., Cilliers P.J. and Zaka Z.K., "Evaluation of the NeQuick model performance under different geomagnetic conditions over South Africa during the ascending phase of the solar cycle (2009–2012)", *Annales Geophysicae*, volume 36, pp. 1161–1170, Copernicus GmbH, 2018.

Akasofu S.I., "Relationships between the AE and Dst indices during geomagnetic storms", *Journal of Geophysical Research: Space Physics*, **86**(A6), pp. 4820–4822, 1981.

Akasofu S.I., Chapman S. and Venkatesan D., "The main phase of great magnetic storms", *Journal of Geophysical Research*, **68**(11), pp. 3345–3350, 1963.

Amabayo E.B., McKinnell L.A. and Cilliers P.J., "Ionospheric response over South Africa to the geomagnetic storm of 11–13 April 2001", *Journal of Atmospheric and Solar-Terrestrial Physics*, **84**, pp. 62–74, 2012.

Amarante G.M., Santamaría M.C., Alazo K. and Radicella S., "Validation of the STORM model used in IRI with ionosonde data", *Advances in Space Research*, **39**(5), pp. 681–686, 2007.

Appleton E.V., "Wireless studies of the ionosphere", *Institution of Electrical Engineers-Proceedings of the Wireless Section of the Institution*, **7**(21), pp. 257–265, 1932.

Appleton E.V. and Barnett M., "On wireless interference phenomena between ground waves and waves deviated by the upper atmosphere", *Proceedings of the Royal Society of London. Series A, Containing Papers of a Mathematical and Physical Character*, **113**(764), pp. 450–458, 1926.

Araujo-Pradere E., Fuller-Rowell T. and Codrescu M., "STORM: An empirical storm-time ionospheric correction model 1. model description", *Radio Science*, **37**(5), 2002.

Araujo-Pradere n.E. and Fuller-Rowell T., "STORM: An empirical storm-time ionospheric correction model 2. Validation", *Radio Science*, **37**(5), pp. 4–1, 2002.

Astafyeva E., Zakharenkova I. and Förster M., "Ionospheric response to the 2015 St. Patrick's Day storm: A global multi-instrumental overview", *Journal of Geophysical Research: Space Physics*, **120**(10), pp. 9023–9037, 2015.

Ataç T., Özgüç A. and Pektaş R., "The variability of foF2 in different phases of solar cycle 23", *Journal of Atmospheric and Solar-Terrestrial Physics*, **71**(5), pp. 583–588, 2009.

Bagiya M.S., Iyer K., Joshi H., Thampi S.V., Tsugawa T., Ravindran S., Sridharan R. and Pathan B., "Low-latitude ionospheric-thermospheric response to storm time electrodynamical coupling between high and low latitudes", *Journal of Geophysical Research: Space Physics*, **116**(A1), 2011.

Balan N., Bailey G., Nair R.B. and Titheridge J., "Nighttime enhancements in ionospheric electron content in the northern and southern hemispheres", *Journal of atmospheric and terrestrial physics*, **56**(1), pp. 67–79, 1994.

Balan N., Shiokawa K., Otsuka Y., Kikuchi T., Vijaya Lekshmi D., Kawamura S., Yamamoto M. and Bailey G., "A physical mechanism of positive ionospheric storms at low latitudes and midlatitudes", *Journal of Geophysical Research: Space Physics*, **115**(A2), 2010.

Banerjee A., Bej A. and Chatterjee T., "On the existence of a long range correlation in the geomagnetic disturbance storm time (Dst) index", *Astrophysics and Space Science*, **337**(1), pp. 23–32, 2012.

Bartels J., "The standardized index, Ks, and the planetary index, Kp", *IATME Bull*, **97**(12b), p. 0001, 1949.

Bartels J., "The geomagnetic measures for the time-variations of solar corpuscular radiation, described for use in correlation studies in other geophysical fields", *Annals of the International Geophysical Year*, **4**, pp. 227–236, 1957a.

Bartels J., "The technique of scaling indices K and Q of geomagnetic activity", *Annals of the International Geophysical Year*, **4**, pp. 215–226, 1957b.

Bartels J., Heck N. and Johnston H., "The three-hour-range index measuring geomagnetic activity", *Terrestrial Magnetism and Atmospheric Electricity*, **44**(4), pp. 411–454, 1939.

Basu S., Buchau J., Rich F., Weber E., Field E., Heckscher J., Kossey P., Lewis E., Dandekar B., McNamara L. *et al.*, "Ionospheric radio wave propagation", *Handbook of Geophysics and the Space Environment*, pp. 10–1, 1985.

Belehaki A., Jakowski N. and Reinisch B., "Plasmaspheric electron content derived from GPS TEC and digisonde ionograms", *Advances in Space Research*, **33**(6), pp. 833–837, 2004.

Belehaki A., Moraitis G. and Tsagouri I., "On the derivation of an hourly local index to define the normal ionosphere", *Annals of Geophysics*, **43**(1), 2000.

Bergeot N., Tsagouri I., Bruyninx C., Legrand J., Chevalier J.M., Defraigne P., Baire Q. and Pottiaux E., "The influence of space weather on ionospheric total electron content during the 23rd solar cycle", *Journal of Space Weather and Space Climate*, **3**(A25), 2013.

Bhamer, "Earth's atmosphere and ionosphere", *https://en.wikipedia.org/wiki/Ionosphere*, **Retrieved on 20 August 2019**, 2007.

Bilitza D., "Evaluation of the IRI-2007 model options for the topside electron density", *Advances in Space Research*, **44**(6), pp. 701–706, 2009.

Bilitza D., Altadill D., Zhang Y., Mertens C., Truhlik V., Richards P., McKinnell L.A. and Reinisch B., "The International Reference Ionosphere 2012 - a model of international collaboration", *Journal of Space Weather and Space Climate*, **4**, p. A07, 2014.

Bilitza D., McKinnell L.A., Reinisch B. and Fuller-Rowell T., "The international reference ionosphere today and in the future", *Journal of Geodesy*, **85**(12), pp. 909–920, 2011.

Bilitza D., Rawer K., Bossy L., Kutiev I., Oyama K.I., Leitinger R. and Kazimirovsky E., "International reference ionosphere 1990", *Report: NSSDC/WDC-A-RS 90-22*, 1990.

Bilitza D. and Reinisch B.W., "International reference ionosphere 2007: Improvements and new parameters", *Advances in Space Research*, **42**(4), pp. 599–609, 2008.

Bilitza D., Reinisch B.W., Radicella S.M., Pulinets S., Gulyaeva T. and Triskova L., "Improvements of the International Reference Ionosphere model for the topside electron density profile", *Radio Science*, **41**(5), 2006.

Blagoveshchensky D. and Sergeeva M., "Impact of geomagnetic storm of September 7–8, 2017 on ionosphere and HF propagation: A multi-instrument study", *Advances in Space Research*, **63**(1), pp. 239–256, 2019.

Blagoveshchensky D.V., Maltseva O.A. and Sergeeva M.A., "Impact of magnetic storms on the global TEC distribution", *Annales Geophysicae*, **36**(4), pp. 1057–1071, 2018.

Blanch E., Altadill D., Boška J., Burešová D. and Hernández-Pajares M., "November 2003 event: effects on the Earth's ionosphere observed from ground-based ionosonde and GPS data", *Annales Geophysicae*, **23**(9), pp. 3027–3034, 2005.

Borovsky J.E. and Denton M.H., "Differences between CME-driven storms and CIR-driven storms", *Journal of Geophysical Research: Space Physics*, **111**(A7), 2006.

Borries C., Berdermann J., Jakowski N. and Wilken V., "Ionospheric stormsA challenge for empirical forecast of the total electron content", *Journal of Geophysical Research: Space Physics*, **120**(4), pp. 3175–3186, 2015.

Breit G. and Tuve M.A., "A test of the existence of the conducting layer", *Physical Review*, **28**(3), p. 554, 1926.

Buonsanto M.J., "Ionospheric stormsA review", *Space Science Reviews*, **88**(3-4), pp. 563–601, 1999.

Burešová D. and Laštovička J., "Pre-storm enhancements of foF2 above Europe", *Advances in Space Research*, **39**(8), pp. 1298–1303, 2007.

Burešová D. and Laštovička J., "Pre-storm electron density enhancements at middle latitudes", *Journal of Atmospheric and Solar-Terrestrial Physics*, **70**(15), pp. 1848–1855, 2008.

Burns A., Killeen T., Deng W., Carignan G. and Roble R., "Geomagnetic storm effects in the low-to middle-latitude upper thermosphere", *Journal of Geophysical Research: Space Physics*, **100**(A8), pp. 14673–14691, 1995.

Burrell A.G., Bonito N.A. and Carrano C.S., "Total electron content processing from GPS observations to facilitate ionospheric modeling", *GPS solutions*, **13**(2), pp. 83–95, 2009.

Cander L.R., "Artificial neural network applications in ionospheric studies", *Annals of Geophysics*, **41**(5-6), 1998.

Cander L.R., "Forecasting foF2 and MUF (3000) F2 ionospheric characteristics–A challenging space weather frontier", *Advances in Space Research*, **56**(9), pp. 1973–1981, 2015.

Cander L.R., "Ionosphere Space Weather and Radio Propagation", *Ionospheric Space Weather*, pp. 197–243, Springer, 2019.

Cander L.R. and Mihajlovic S., "Forecasting ionospheric structure during the great geomagnetic storms", *Journal of Geophysical Research: Space Physics*, **103**(A1), pp. 391–398, 1998.

Carrano C. and Groves K., "Ionospheric data processing and analysis", *Workshop on Satellite Navigation Science and Technology for Africa, The Abdus Salam ICTP, Trieste, Italy*, 2009.

Chashei I., Tyul'bashev S., Shishov V. and Subaev I., "Interplanetary and ionosphere scintillation produced by ICME 20 December 2015", *Space Weather*, **14**(9), pp. 682–688, 2016.

Chatterjee S. and Hadi A.S., *Regression Analysis by Example, Fourth Edition*, John Wiley & Sons, 2006.

Chekole D.A., Giday N.M. and Nigussie M., "Performance of NeQuick-2, IRI-Plas 2017 and GIM models over Ethiopia during varying solar activity periods", *Journal of Atmospheric and Solar-Terrestrial Physics*, **195**, p. 105117, 2019.

Chen H., Liu L., Wan W., Ning B. and Lei J., "A comparative study of the bottomside profile parameters over Wuhan with IRI-2001 for 1999–2004", *Earth, Planets and Space*, **58**(5), pp. 601–605, 2006.

Chen Y., Liu L. and Wan W., "Does the F10. 7 index correctly describe solar EUV flux during the deep solar minimum of 2007–2009?", *Journal of Geophysical Research: Space Physics*, **116**(A4), 2011.

Cherniak I. and Zakharenkova I., "Large-scale traveling ionospheric disturbances origin and propagation: Case study of the December 2015 geomagnetic storm", *Space Weather*, **16**(9), pp. 1377–1395, 2018.

Chu Y.H., Su C.L. and Ko H.T., "A global survey of COSMIC ionospheric peak electron density and its height: A comparison with ground-based ionosonde measurements", *Advances in Space Research*, **46**(4), pp. 431–439, 2010.

Coïsson P., Radicella S., Leitinger R. and Nava B., "Topside electron density in IRI and NeQuick: Features and limitations", *Advances in Space Research*, **37**(5), pp. 937–942, 2006.

Cook R.D. and Weisberg S., *Residuals and Influence in Regression*, New York: Chapman and Hall, 1982.

Dabas R. and Kersley L., "Study of mid-latitude nighttime enhancement in F-region electron density using tomographic images over the UK", *Annales Geophysicae*, **21**, pp. 2323–2328, 2003.

Danilov A., "F2-region response to geomagnetic disturbances", *Journal of Atmospheric and Solar-Terrestrial Physics*, **63**(5), pp. 441–449, 2001.

Danilov A., "Ionospheric F-region response to geomagnetic disturbances", *Advances in Space Research*, **52**(3), pp. 343–366, 2013.

Davies K., *Ionospheric radio*, 31, Peter Peregrinus Ltd., London, United Kingdom, 1990.

Davis T.N. and Sugiura M., "Auroral electrojet activity index AE and its universal time variations", *Journal of Geophysical Research*, **71**(3), pp. 785–801, 1966.

Denton M., Borovsky J.E., Skoug R., Thomsen M., Lavraud B., Henderson M., McPherron R., Zhang J.C. and Liemohn M., "Geomagnetic storms driven by ICME-and CIR-dominated solar wind", *Journal of Geophysical Research: Space Physics*, **111**(A7), 2006.

Dessler A., Hanson W. and Parker E., "Formation of the geomagnetic storm main-phase ring current", *Journal of Geophysical Research*, **66**(11), pp. 3631–3637, 1961.

Echer E., Tsurutani B. and Guarnieri F., "Interplanetary origins of November 2004 superstorms", *Journal of Atmospheric and Solar-Terrestrial Physics*, **72**(4), pp. 280–284, doi: 10.1016/j.jastp.2009.02.009, 2010.

Elman J.L., "Finding structure in time", *Cognitive science*, **14**(2), pp. 179–211, 1990.

Ercha A., Zhang D., Ridley A.J., Xiao Z. and Hao Y., "A global model: Empirical orthogonal function analysis of total electron content 1999–2009 data", *Journal of Geophysical Research: Space Physics*, **117**(A3), 2012.

Fausett L., *Fundamentals of neural networks: architectures, algorithms, and applications*, 006.3, Prentice-Hall,, 1994.

Fejer B.G., Jensen J., Kikuchi T., Abdu M. and Chau J., "Equatorial ionospheric electric fields during the November 2004 magnetic storm", *Journal of Geophysical Research: Space Physics*, **112**(A10), 2007.

Fuller-Rowell T., Araujo-Pradere E. and Codrescu M., "An empirical ionospheric storm-time correction model", *Advances in Space Research*, **25**(1), pp. 139–146, 2000a.

Fuller-Rowell T., Codrescu M., Araujo-Pradere E. and Kutiev I., "Progress in developing a storm-time ionospheric correction model", *Advances in Space Research*, **22**(6), pp. 821–827, 1998.

Fuller-Rowell T., Codrescu M., Moffett R. and Quegan S., "Response of the thermosphere and ionosphere to geomagnetic storms", *Journal of Geophysical Research: Space Physics*, **99**(A3), pp. 3893–3914, 1994.

Fuller-Rowell T., Codrescu M. and Wilkinson P., "Quantitative modeling of the ionospheric response to geomagnetic activity", volume 18, pp. 766–781, Springer, 2000b.

Galkin I.A. and Reinisch B.W., "The new ARTIST 5 for all digisondes", *Ionosonde Network Advisory Group Bulletin*, **69**(8), pp. 1–8, 2008.

Gao Q., Liu L.B., Zhao B.Q., Wan W.X., Zhang M.L. and Ning B.Q., "Statistical Study of the Storm Effects in Middle and Low Latitude Ionosphere in the East-Asian Sector", *Chinese Journal of Geophysics*, **51**(3), pp. 435–443, 2008.

Gonzalez W., Joselyn J., Kamide Y., Kroehl H., Rostoker G., Tsurutani B. and Vasyliunas V., "What is a geomagnetic storm?", *Journal of Geophysical Research: Space Physics*, **99**(A4), pp. 5771–5792, 1994.

Gonzalez W.D., Tsurutani B.T. and De Gonzalez A.L.C., "Interplanetary origin of geomagnetic storms", *Space Science Reviews*, **88**(3-4), pp. 529–562, 1999.

Gopalswamy N., "The CME link to geomagnetic storms", *Proceedings of the International Astronomical Union*, **5**(S264), pp. 326–335, 2009.

Gopalswamy N., Barbieri L., Cliver E., Lu G., Plunkett S. and Skoug R., "Introduction to violent Sun-Earth connection events of October–November 2003", *Journal of Geophysical Research: Space Physics*, **110**(A9), 2005a.

Gopalswamy N., Yashiro S., Michalek G., Xie H., Lepping R. and Howard R., "Solar source of the largest geomagnetic storm of cycle 23", *Geophysical Research Letters*, **32**(12), 2005b.

Greer K., Immel T. and Ridley A., "On the variation in the ionospheric response to geomagnetic storms with time of onset", *Journal of Geophysical Research: Space Physics*, **122**(4), pp. 4512–4525, 2017.

Gulyaeva T. and Stanislawska I., "Derivation of a planetary ionospheric storm index", *Annales Geophysicae*, **26**(9), pp. 2645–2648, 2008.

Habarulema J. and McKinnell L.A., "Investigating the performance of neural network back-propagation algorithms for TEC estimations using South African GPS data", *Annales Geophysicae*, volume 30, pp. 857–866, Copernicus GmbH, 2012.

Habarulema J.B., *A contribution to TEC modelling over Southern Africa using GPS data*, Ph.D. thesis, Rhodes University, 2010.

Habarulema J.B. and Carelse S.A., "Long-term analysis between radio occultation and ionosonde peak electron density and height during geomagnetic storms", *Geophysical Research Letters*, **43**(9), pp. 4106–4111, doi:10.1002/2016GL068944, 2016.

Habarulema J.B., Katamzi Z.T., Sibanda P. and Matamba T.M., "Assessing ionospheric response during some strong storms in solar cycle 24 using various data sources", *Journal of Geophysical Research: Space Physics*, **122**(1), pp. 1064–1082, doi:10.1002/2016JA023066, 2017.

Habarulema J.B., Katamzi Z.T. and Yizengaw E., "A simultaneous study of ionospheric parameters derived from FORMOSAT-3/COSMIC, GRACE, and CHAMP missions over middle, low, and equatorial latitudes: Comparison with ionosonde data", *Journal of Geophysical Research: Space Physics*, **119**(9), pp. 7732–7744, 2014.

Habarulema J.B., Katamzi-Joseph Z.T., Burešová D., Nndanganeni R., Matamba T.M., Tshisaphungo M., Buchert S., Kosch M., Lotz S., Cilliers P. and Mahrous A., "Ionospheric response at conjugate locations during the 7-8 September 2017 geomagnetic storm over the Europe-African longitude sector", *Journal of Geophysical Research: Space Physics*, **122**, 2020.

Habarulema J.B., McKinnell L.A., Burešová D., Zhang Y., Seemala G., Ngwira C., Chum J. and Opperman B., "A comparative study of TEC response for the African equatorial and mid-latitudes during storm conditions", *Journal of Atmospheric and Solar-Terrestrial Physics*, **102**, pp. 105–114, 2013.

Habarulema J.B., McKinnell L.A., Cilliers P.J. and Opperman B.D., "Application of neural networks to South African GPS TEC modelling", *Advances in Space Research*, **43**(11), pp. 1711–1720, 2009.

Habarulema J.B., McKinnell L.A. and Opperman B.D., "TEC measurements and modelling over Southern Africa during magnetic storms; a comparative analysis", *Journal of Atmospheric and Solar-Terrestrial Physics*, **72**(5), pp. 509–520, 2010.

Habarulema J.B., McKinnell L.A. and Opperman B.D., "Regional GPS TEC modeling; Attempted spatial and temporal extrapolation of TEC using neural networks", *Journal of Geophysical Research: Space Physics*, **116**(A4), 2011.

Habarulema J.B. and Ssessanga N., "Adapting a climatology model to improve estimation of ionosphere parameters and subsequent validation with radio occultation and ionosonde data", *Space Weather*, **15**(1), pp. 84–98, 2017.

Hagan M.T., Demuth H.B., Beale M.H. and De Jesús O., *Neural network design*, volume 20, Pws Pub. Boston, 1996.

Hajj G., Lee L., Pi X., Romans L., Schreiner W., Straus P. and Wang C., "COSMIC GPS ionospheric sensing and space weather", *Terrestrial, Atmospheric and Oceanic Sciences*, **11**(1), pp. 235–273, 2000.

Hajj G.A., Kursinski E., Romans L., Bertiger W. and Leroy S., "A technical description of atmospheric sounding by GPS occultation", *Journal of Atmospheric and Solar-Terrestrial Physics*, **64**(4), pp. 451–469, 2002.

Hargreaves J.K., "The upper atmosphere and solar-terrestrial relations-An introduction to the aerospace environment", *New York, Van Nostrand Reinhold Co., 1979. 312 p.*, 1979.

Hargreaves J.K., *The Solar-Terrestrial Environment*, Cambridge University Press, 1992.

Haykin S., *Neural Networks: A Comprehensive Foundation*, Prentice Hall PTR, 1994.

Heber B., Sanderson T. and Zhang M., "Corotating interaction regions", *Advances in Space Research*, **23**(3), pp. 567–579, 1999.

Heelis R. and Maute A., "Challenges to Understanding the Earth's Ionosphere and Thermosphere", *Journal of Geophysical Research: Space Physics*, **125**(7), p. e2019JA027497, 2020.

Ho C., Wilson B., Mannucci A., Lindqwister U. and Yuan D., "A comparative study of ionospheric total electron content measurements using global ionospheric maps of GPS, TOPEX radar, and the Bent model", *Radio Science*, **32**(4), pp. 1499–1512, 1997.

Hochegger G., Nava B., Radicella S. and Leitinger R., "A family of ionospheric models for different uses", *Physics and Chemistry of the Earth, Part C: Solar, Terrestrial & Planetary Science*, **25**(4), pp. 307–310, 2000.

Hofmann-Wellenhof B., Lichtenegger H. and Collins J., *Global Positioning System: Theory and Practice*, Springer-Verlag Wien New York, 1992.

Hofmann-Wellenhof B., Lichtenegger H. and Wasle E., *GNSS–global navigation satellite systems: GPS, GLONASS, Galileo, and more*, Springer Science & Business Media, 2007.

Horvath I. and Lovell B.C., "Formation and evolution of the ionospheric plasma density shoulder and its relationship to the superfountain effects investigated during the 6 November 2001 great storm", *Journal of Geophysical Research: Space Physics*, **113**(A12), 2008.

Huang Y., Huang C.Y., Su Y.J., Deng Y. and Fang X., "Ionization due to electron and proton precipitation during the August 2011 storm", *Journal of Geophysical Research: Space Physics*, **119**(4), pp. 3106–3116, 2014.

Hunsucker R.D., *Radio techniques for probing the terrestrial ionosphere*, Physics and Chemistry in Space Vol. 22 Planetology,Springer-Verlag Berlin Heidelberg, 1991.

Hunsucker R.D. and Hargreaves J.K., *The high-latitude ionosphere and its effects on radio propagation*, Cambridge University Press, 2007.

Huttunen K.E.J., Koskinen H.E. and Schwenn R., "Variability of magnetospheric storms driven by different solar wind perturbations", *Journal of Geophysical Research: Space Physics*, **107**(A7), pp. SMP–20, 2002.

Imtiaz N., Younas W. and Khan M., "Response of the low-to mid-latitude ionosphere to the geomagnetic storm of September 2017", *Annales Geophysicae*, **38**(2), pp. 359–372, doi:10.5194/angeo-38-359-2020, 2020.

Irving R.S., *Integers, Polynomials, and Rings: A Course in Algebra*, Springer Science & Business Media, 2003.

Jakowski N., Borries C. and Wilken V., "Introducing a disturbance ionosphere index", *Radio Science*, **47**(4), 2012.

Jakowski N., Stankov S. and Klaehn D., "Operational space weather service for GNSS precise positioning", *Annales Geophysicae*, **23**(9), pp. 3071–3079, 2005.

Jakowski N., Stankov S., Schlueter S. and Klaehn D., "On developing a new ionospheric perturbation index for space weather operations", *Advances in Space Research*, **38**(11), pp. 2596–2600, 2006.

Joselyn J. and Tsurutani B., "Geomagnetic sudden impulses and storm sudden commencements: A note on terminology", *Eos, Transactions American Geophysical Union*, **71**(47), pp. 1808–1809, 1990.

Kamide Y. and Akasofu S.I., "Notes on the auroral electrojet indices", *Reviews of Geophysics*, **21**(7), pp. 1647–1656, 1983.

Kamide Y., Baumjohann W., Daglis I., Gonzalez W., Grande M., Joselyn J., McPherron R., Phillips J., Reeves E., Rostoker G. *et al.*, "Current understanding of magnetic storms: Storm-substorm relationships", *Journal of Geophysical Research: Space Physics*, **103**(A8), pp. 17705–17728, 1998a.

Kamide Y., Yokoyama N., Gonzalez W., Tsurutani B., Daglis I., Brekke A. and Masuda S., "Two-step development of geomagnetic storms", *Journal of Geophysical Research: Space Physics*, **103**(A4), pp. 6917–6921, 1998b.

Kaplan E. and Hegarty C., *Understanding GPS: principles and applications*, Artech house, 2005.

Katamzi Z.T. and Habarulema J.B., "Traveling ionospheric disturbances observed at South African midlatitudes during the 29–31 October 2003 geomagnetically disturbed period", *Advances in Space Research*, **53**(1), pp. 48–62, 2014.

Kelley M.C., *The Earth's Ionosphere: Plasma Physics and Electrodynamics*, volume 96, Academic press, 2009.

Kikuchi T., Hashimoto K.K. and Nozaki K., "Storm phase dependence of penetration of magnetospheric electric fields to mid and low latitudes", *Midlatitude Ionospheric Dynamics and Disturbances*, pp. 145–155, 2008.

Klimenko M., Klimenko V., Zakharenkova I. and Cherniak I.V., "The global morphology of the plasmaspheric electron content during Northern winter 2009 based on GPS/COSMIC observation and GSM TIP model results", *Advances in Space Research*, **55**(8), pp. 2077–2085, 2015.

Klimenko M.V., Klimenko V.V., Zakharenkova I.E., Ratovsky K.G., Korenkova N.A., Yasyukevich Y.V., Mylnikova A.A. and Cherniak I.V., "Similarity and differences in morphology and mechanisms of the foF2 and TEC disturbances during the geomagnetic storms on 26-30 September 2011.", *Annales Geophysicae (09927689)*, **35**(4), 2017.

Klobuchar J.A., Doherty P.H. and EL-ARINI M.B., "Potential ionospheric limitations to GPS wide-area augmentation system (WAAS)", *Navigation*, **42**(2), pp. 353–370, 1995.

Kouris S.S., Xenos T.D., Polimeris K.V. and Stergiou D., "TEC and foF2 variations: preliminary results", *Annals of Geophysics*, 2004.

Krankowski A., Shagimuratov I. and Baran L., "Mapping of foF2 over Europe based on GPS-derived TEC data", *Advances in Space Research*, **39**(5), pp. 651–660, 2007.

Krankowski A., Shagimuratov I., Baran L., Yakimova G. and Radievsky A., "Storm-time changes in ionospheric TEC during the disturbances on the November 5-7, 2001 storm", *Papers presented at European Geosciences Union (EGU) 1st General Assembly, Nice, 26-30 April 2004 Guest Editors: Dr. Bruno Zolesi and Dr. Ljiliana Cander*, **30**, p. 10, 2004.

Krankowski A., Zakharenkova I., Krypiak-Gregorczyk A., Shagimuratov I.I. and Wielgosz P., "Ionospheric electron density observed by FORMOSAT-3/COSMIC over the European region and validated by ionosonde data", *Journal of Geodesy*, **85**(12), pp. 949–964, 2011.

Kursinski E.R., Hajj G.A., Leroy S.S. and Herman B., "The GPS radio occultation technique", *Terrestrial Atmospheric Oceanic Sciences*, **11**(1), pp. 53–114, 2000.

Kutiev I. and Muhratov P., "Modeling of midlatitude F region response to geomagnetic activity", *Journal of Geophysical Research*, **106**(A8), pp. 15501–15510, 2001.

Kutiev I. and Muhtarov P., "Empirical modeling of global ionospheric foF2 response to geomagnetic activity", *Journal of Geophysical Research: Space Physics*, **108**(A1), 2003.

Laštovička J., Mikhailov A., Ulich T., Bremer J., Elias A., Ortiz de Adler N., Jara V., Abarca del Rio R., Foppiano A., Ovalle E. and Danilov A., "Long-term trends in foF2: A comparison of

various methods", *Journal of Atmospheric and Solar-Terrestrial Physics*, **68**(17), pp. 1854–1870, 2006.

LDI, "Background to Ionospheric Sounding", *http://www.digisonde.com/instrument-description.html*, **Obtained on 31 January 2020**, 2015.

Lei J., Syndergaard S., Burns A.G., Solomon S.C., Wang W., Zeng Z., Roble R.G., Wu Q., Kuo Y.H., Holt J.M. *et al.*, "Comparison of COSMIC ionospheric measurements with ground-based observations and model predictions: Preliminary results", *Journal of Geophysical Research: Space Physics*, **112**(A7), 2007.

Leung K., Suen S. and Mok I.A., *Polynomials and Equations: A Chinese Merchant Elite in Colonial Hong Kong (with a new preface)*, volume 1, Hong Kong University Press, 1992.

Li H., Wang C. and Kan J., "Contribution of the partial ring current to the SYMH index during magnetic storms", *Journal of Geophysical Research: Space Physics*, **116**(A11), 2011.

Li Q., Hao Y., Zhang D. and Xiao Z., "Nighttime enhancements in the midlatitude ionosphere and their relation to the plasmasphere", *Journal of Geophysical Research: Space Physics*, **123**(9), pp. 7686–7696, 2018.

Liu J., Zhao B. and Liu L., "Time delay and duration of ionospheric total electron content responses to geomagnetic disturbances", *Annales Geophysicae*, **28**(3), pp. 795–805, 2010.

Liu L. and Chen Y., "Statistical analysis of solar activity variations of total electron content derived at Jet Propulsion Laboratory from GPS observations", *Journal of Geophysical Research*, **114**(A10), 2009.

Liu L., Le H., Chen Y., He M., Wan W. and Yue X., "Features of the middle-and low-latitude ionosphere during solar minimum as revealed from COSMIC radio occultation measurements", *Journal of Geophysical Research: Space Physics*, **116**(A9), 2011.

Liu L., Wan W. and Ning B., "Statistical modeling of ionospheric foF2 over Wuhan", *Radio Science*, **39**(2), 2004.

Liu L., Wan W., Ning B., Pirog O. and Kurkin V., "Solar activity variations of the ionospheric peak electron density", *Journal of Geophysical Research: Space Physics*, **111**(A8), 2006.

Loewe C. and Prölss G., "Classification and mean behavior of magnetic storms", *Journal of Geophysical Research: Space Physics*, **102**(A7), pp. 14209–14213, 1997.

Luan X., Wang W., Burns A., Solomon S.C. and Lei J., "Midlatitude nighttime enhancement in F region electron density from global COSMIC measurements under solar minimum winter condition", *Journal of Geophysical Research: Space Physics*, **113**(A9), 2008.

Mannucci A., Tsurutani B., Iijima B., Komjathy A., Saito A., Gonzalez W., Guarnieri F., Kozyra J. and Skoug R., "Dayside global ionospheric response to the major interplanetary events of October 29–30, 2003 Halloween Storms", *Geophysical Research Letters*, **32**(12), 2005.

Mansilla G.A., "Behavior of the total electron content over the Arctic and Antarctic sectors during several intense geomagnetic storms", *Geodesy and Geodynamics*, **10**(1), pp. 26–36, 2019.

Maruyama T., Ma G. and Nakamura M., "Signature of TEC storm on 6 November 2001 derived from dense GPS receiver network and ionosonde chain over Japan", *Journal of Geophysical Research: Space Physics*, **109**(A10), 2004.

Maruyama T. and Nakamura M., "Conditions for intense ionospheric storms expanding to lower midlatitudes", *Journal of Geophysical Research: Space Physics*, **112**(A5), 2007.

Matamba T.M., *Long-term analysis of ionospheric response during geomagnetic storms in mid, low and equatorial latitudes*, Ph.D. thesis, Rhodes University, Grahamstown, South Africa, 2017.

Matamba T.M. and Habarulema J.B., "Ionospheric responses to CME-and CIR-driven geomagnetic storms along 30° E–40° E over the African sector from 2001 to 2015", *Space Weather*, **16**(5), pp. 538–556, 2018.

Matamba T.M., Habarulema J.B. and Burešová D., "Midlatitude ionospheric changes to four great geomagnetic storms of solar cycle 23 in Southern and Northern Hemispheres", *Space Weather*, **14**, pp. 1155–1171, 2016.

Matamba T.M., Habarulema J.B. and McKinnell L.A., "Statistical analysis of the ionospheric response during geomagnetic storm conditions over South Africa using ionosonde and GPS data", *Space Weather*, **13**(9), pp. 536–547, 2015.

Matsushita S., "A study of the morphology of ionospheric storms", *Journal of Geophysical Research*, **64**(3), pp. 305–321, 1959.

Mayaud P.N., "Derivation, meaning, and use of geomagnetic indices", *Washington DC American Geophysical Union Geophysical Monograph Series*, **22**, 1980.

McKinnell L.A. and Poole A.W., "Neural network-based ionospheric modelling over the South African region", *South African Journal of Science*, **100**(11), pp. 519–523, 2004a.

McKinnell L.A. and Poole A.W., "Predicting the ionospheric F layer using neural networks", *Journal of Geophysical Research: Space Physics*, **109**(A8), 2004b.

McNamara L.F., *The ionosphere: communications, surveillance, and direction finding*, Krieger publishing company, 1991.

McNamara L.F., "Quality figures and error bars for autoscaled Digisonde vertical incidence ionograms", *Radio science*, **41**(04), pp. 1–16, 2006.

Medsker L. and Jain L.C., *Recurrent neural networks: design and applications*, CRC press, 1999.

Mendillo M., Papagiannis M. and Klobuchar J., "Ionospheric storms at midlatitudes", *Radio Science*, **5**(6), pp. 895–898, 1970.

Mengistu E., Damtie B., Moldwin M. and Nigussie M., "Comparison of GPS-TEC measurements with NeQuick2 and IRI model predictions in the low latitude East African region during varying solar activity period (1998 and 2008–2015)", *Advances in Space Research*, **61**(6), pp. 1456–1475, 2018.

Misra P. and Enge P., *Global positioning system: signals, measurements and performance*, Ganga-Jamuna Press, 2006.

Mitchell T.J. and Beauchamp J.J., "Bayesian variable selection in linear regression", *Journal of the american statistical association*, **83**(404), pp. 1023–1032, 1988.

Moldwin M., *An introduction to space weather*, Cambridge University Press, 2008.

Morozova A.L., Barlyaeva T.V. and Barata T., "Variations of TEC over Iberian Peninsula in 2015: geomagnetic storms, solar flares, solar eclipse", *arXiv preprint arXiv:1912.00959*, 2019.

Mosna Z., Kouba D., Knizova P.K., Buresova D., Chum J., Sindelarova T., Urbar J., Boska J. and Saxonbergova-Jankovicova D., "Ionospheric storm of September 2017 observed at ionospheric station Pruhonice, the Czech Republic", *Advances in Space Research*, **65**(1), pp. 115–128, doi:10.1016/j.asr.2019.09.024, 2020.

Muhtarov P. and Kutiev I., "Empirical modelling of ionospheric storms at midlatitudes", *Advances in Space Research*, **22**(6), pp. 829–832, 1998.

Mukhtarov P., Andonov B. and Pancheva D., "Global empirical model of TEC response to geomagnetic activity", *Journal of Geophysical Research: Space Physics*, **118**(10), pp. 6666–6685, 2013a.

Mukhtarov P., Pancheva D., Andonov B. and Pashova L., "Global TEC maps based on GNSS data: 1. Empirical background TEC model", *Journal of Geophysical Research: Space Physics*, **118**(7), pp. 4594–4608, 2013b.

Nava B., Coisson P. and Radicella S., "A new version of the NeQuick ionosphere electron density model", *Journal of Atmospheric and Solar-Terrestrial Physics*, **70**(15), pp. 1856–1862, 2008.

Nava B., Radicella S. and Azpilicueta F., "Data ingestion into NeQuick 2", *Radio Science*, **46**(06), pp. 1–8, 2011.

Nava B., Rodríguez-Zuluaga J., Alazo-Cuartas K., Kashcheyev A., Migoya-Orué Y., Radicella S., Amory-Mazaudier C. and Fleury R., "Middle-and low-latitude ionosphere response to 2015 St. Patrick's Day geomagnetic storm", *Journal of Geophysical Research: Space Physics*, **121**(4), pp. 3421–3438, 2016.

Ngwira C.M., McKinnell L.A., Cilliers P.J. and Yizengaw E., "An investigation of ionospheric disturbances over South Africa during the magnetic storm on 15 May 2005", *Advances in Space Research*, **49**(2), pp. 327–335, 2012.

Nigussie M., Radicella S., Damtie B., Nava B., Yizengaw E. and Groves K., "Validation of the NeQuick 2 and IRI-2007 models in East-African equatorial region", *Journal of Atmospheric and Solar-Terrestrial Physics*, **102**, pp. 26–33, 2013.

Nishioka M., Tsugawa T., Jin H. and Ishii M., "A new ionospheric storm scale based on TEC and foF2 statistics", *Space Weather*, **15**(1), pp. 228–239, 2017.

Nosé M., Iyemori T., Odagi Y., Takeda M., Toh H., Koyama Y. and Takeuchi N., "High-Time Resolution Geomagnetic Indices", *Data Analysis Center for Geomagnetism and Space Magnetism, Graduate School of Science, Kyoto University*, 2012.

Okoh D., Onwuneme S., Seemala G., Jin S., Rabiu B., Nava B. and Uwamahoro J., "Assessment of the NeQuick-2 and IRI-Plas 2017 models using global and long-term GNSS measurements", *Journal of Atmospheric and Solar-Terrestrial Physics*, **170**, pp. 1–10, 2018.

Okoh D., Seemala G., Rabiu B., Habarulema J.B., Jin S., Shiokawa K., Otsuka Y., Aggarwal M., Uwamahoro J., Mungufeni P. *et al.*, "A neural network-based ionospheric model over Africa from Constellation Observing System for Meteorology, Ionosphere, and Climate and Ground Global Positioning System observations", *Journal of Geophysical Research: Space Physics*, **124**(12), pp. 10512–10532, 2019.

Okoh D.I., McKinnell L. and Cilliers P., "Developing an ionospheric map for South Africa", *Annales Geophysicae*, volume 28, pp. 1431–1439, Copernicus GmbH, 2010.

Ortikov M.Y., Shemelov V., Shishigin I.V. and Troitsky B., "Ionospheric index of solar activity based on the data of measurements of the spacecraft signals characteristics", *Journal of Atmospheric and Solar-Terrestrial Physics*, **65**(16-18), pp. 1425–1430, 2003.

Otugo V., Okoh D., Okujagu C., Onwuneme S., Rabiu B., Uwamahoro J., Habarulema J.B., Tshisaphungo M. and Ssessanga N., "Estimation of ionospheric critical plasma frequencies from GNSS-TEC measurements using artificial neural networks", *Space Weather*, **17**(8), pp. 1329–1340, 2019.

Oyeyemi E.O., McKinnell L.A. and Poole A., "Near-real time foF2 predictions using neural networks", *Journal of Atmospheric and Solar-Terrestrial Physics*, **68**(16), pp. 1807–1818, 2006.

Parkinson B.W., Enge P., Axelrad P. and Spilker Jr J.J., *Global positioning system: Theory and applications, Volume II*, American Institute of Aeronautics and Astronautics, 1996.

Piddington J., "Theories of the geomagnetic storm main phase", *Planetary and Space Science*, **11**(11), pp. 1277–1288, 1963.

Pietrella M. and Perrone L., "A local ionospheric model for forecasting the critical frequency of the F2 layer during disturbed geomagnetic and ionospheric conditions", **26**(2), pp. 323–334, 2008.

Pignalberi A., Habarulema J.B., Pezzopane M. and Rizzi R., "On the development of a method for updating an empirical climatological ionospheric model by means of assimilated vTEC measurements from a GNSS receiver network", *Space Weather*, **17**(7), pp. 1131–1164, 2019.

Pignalberi A., Pezzopane M., Zuccheretti E. *et al.*, "Sporadic E layer at mid-latitudes: average properties and influence of atmospheric tides", *Annales Geophysicae*, **32**, pp. 1427–1440, 2014.

Poole A.W. and McKinnell L.A., "On the predictability of foF2 using neural networks", *Radio Science*, **35**(1), pp. 225–234, 2000.

Prölss G., "Magnetic storm associated perturbations of the upper atmosphere: Recent results obtained by satellite-borne gas analyzers", *Reviews of Geophysics*, **18**(1), pp. 183–202, 1980.

Prölss G., "Common origin of positive ionospheric storms at middle latitudes and the geomagnetic activity effect at low latitudes", *Journal of Geophysical Research: Space Physics*, **98**(A4), pp. 5981–5991, 1993a.

Prölss G., "On explaining the local time variation of ionospheric storm effects", *Annales Geophysicae*, **11**, pp. 1–9, 1993b.

Prölss G., "Ionospheric F-region storms", *Handbook of atmospheric electrodynamics*, **2**, pp. 195–248, 1995.

Prölss G., Brace L., Mayr H., Carignan G., Killeen T. and Klobuchar J., "Ionospheric storm effects at subauroral latitudes: A case study", *Journal of Geophysical Research: Space Physics*, **96**(A2), pp. 1275–1288, 1991.

Prölss G.W., "Magnetic storm associated perturbations of the upper atmosphere", *Magnetic storms*, **98**, pp. 227–241, 1997.

Prölss G.W., "Ionospheric storms at mid-latitude: A short review", *Washington DC American Geophysical Union Geophysical Monograph Series*, **181**, pp. 9–24, 2008.

Pulkkinen T., "Space weather: terrestrial perspective", *Living Reviews in Solar Physics*, **4**(1), p. 1, 2007.

Radicella S. and Leitinger R., "The evolution of the DGR approach to model electron density profiles", *Advances in Space Research*, **27**(1), pp. 35–40, 2001.

Radicella S.M., "The NeQuick model genesis, uses and evolution", *Annals of Geophysics*, **52**(3-4), pp. 417–422, 2009.

Rawer K., Bilitza D. and Ramakrishnan S., "Goals and status of the International Reference Ionosphere", *Reviews of Geophysics*, **16**(2), pp. 177–181, 1978.

Rawlings J.O., Pantula S.G. and Dickey D.A., *Applied regression analysis: a research tool, Second Edition*, Springer Science & Business Media, 1988.

Reinisch B.W., Galkin I.A., Khmyrov G.M., Kozlov A.V., Lisysyan I.A., Bibl K., Cheney G., Kitrosser D., Stelmash S., Roche K. *et al.*, "Advancing digisonde technology: the DPS-4D", **974**(1), pp. 127–143, 2008.

Reinisch B.W., Gamache R.R., Tang J.S. and Kitrosser D.F., *Automatic real time ionogram scaler with true height analysis-ARTIST*, Technical report, University of Massachusetts Lowell Center for Atmospheric Research, 1983.

Reinisch B.W. and Huang X., "Automatic calculation of electron density profiles from digital ionograms: 3. Processing of bottomside ionograms", *Radio Science*, **18**(3), pp. 477–492, 1983.

Richards P., Torr D., Reinisch B., Gamache R. and Wilkinson P., "F 2 peak electron density at Millstone Hill and Hobart: Comparison of theory and measurement at solar maximum", *Journal of Geophysical Research: Space Physics*, **99**(A8), pp. 15005–15016, 1994.

Richardson I., Webb D., Zhang J., Berdichevsky D., Biesecker D., Kasper J., Kataoka R., Steinberg J., Thompson B., Wu C.C. *et al.*, "Major geomagnetic storms (Dst- 100 nT) generated by corotating interaction regions", *Journal of Geophysical Research: Space Physics*, **111**(A7), 2006.

Richardson I.G., "Solar wind stream interaction regions throughout the heliosphere", *Living Reviews in Solar Physics*, **15**(1), p. 1, 2018.

Richmond A.D., "Ionospheric electrodynamics", *Handbook of Atmospheric Electrodynamics (1995)*, pp. 249–290, CRC Press, 2017.

Rishbeth H., "The equatorial F-layer: progress and puzzles", *Annales Geophysicae*, **18**, pp. 730–739, 2000.

Rishbeth H. and Garriott O.K., "Introduction to ionospheric physics", *IEEE Transactions on Image Processing*, 1969.

Rishbeth H. and Mendillo M., "Patterns of F2-layer variability", *Journal of Atmospheric and Solar-Terrestrial Physics*, **63**(15), pp. 1661–1680, 2001.

Rocken C., Ying-Hwa K., Schreiner W.S., Hunt D., Sokolovskiy S. and McCormick C., "COSMIC system description", *Terrestrial Atmospheric and Oceanic Sciences*, **11**(1), pp. 21–52, 2000.

Rodkin D., Goryaev F., Pagano P., Gibb G., Slemzin V., Shugay Y., Veselovsky I. and Mackay D., "Origin and ion charge state evolution of solar wind transients during 4–7 August 2011", *Solar Physics*, **292**(7), p. 90, 2017.

Rostoker G., "Geomagnetic indices", *Reviews of Geophysics*, **10**(4), pp. 935–950, 1972.

Saba M.F., Gonzalez W. and Clua de Gonzalez A., "Relationships between the AE, ap and Dst indices near solar minimum (1974) and at solar maximum (1979)", *Annales Geophysicae*, volume 15, pp. 1265–1270, Springer, 1997.

Sahai Y., Fagundes P., Becker-Guedes F., Bolzan M., Abalde J., Pillat V., De Jesus R., Lima W., Crowley G., Shiokawa K. *et al.*, "Effects of the major geomagnetic storms of October 2003 on the equatorial and low-latitude F region in two longitudinal sectors", *Journal of Geophysical Research: Space Physics*, **110**(A12), 2005.

Schreiner W., Rocken C., Sokolovskiy S., Syndergaard S. and Hunt D., "Estimates of the precision of GPS radio occultations from the COSMIC/FORMOSAT-3 mission", *Geophysical Research Letters*, **34**(4), 2007.

Schreiner W.S., Sokolovskiy S.V., Rocken C. and Hunt D.C., "Analysis and validation of GPS/MET radio occultation data in the ionosphere", *Radio Science*, **34**(4), pp. 949–966, 1999.

Schrijver C.J., Kauristie K., Aylward A.D., Denardini C.M., Gibson S.E., Glover A., Gopalswamy N., Grande M., Hapgood M., Heynderickx D. *et al.*, "Understanding space weather

to shield society: A global road map for 2015–2025 commissioned by COSPAR and ILWS", *Advances in Space Research*, **55**(12), pp. 2745–2807, 2015.

Schwenn R., "Space weather: The solar perspective", *Living Reviews in Solar Physics*, **3**(1), p. 2, 2006.

Seber G.A. and Lee A.J., *Linear Regression Analysis, Second Edition*, volume 329, John Wiley & Sons, 2003.

Seemala G. and Valladares C., "Statistics of total electron content depletions observed over the South American continent for the year 2008", *Radio Science*, **46**(5), 2011.

Shen X., "Linear regression with current status data", *Journal of the American Statistical Association*, **95**(451), pp. 842–852, 2000.

Skoug R., Gosling J., Steinberg J., McComas D., Smith C., Ness N., Hu Q. and Burlaga L., "Extremely high speed solar wind: 29–30 October 2003", *Journal of Geophysical Research: Space Physics*, **109**(A9), 2004.

Sojka J., David M., Schunk R. and Heelis R., "A modeling study of the longitudinal dependence of storm time midlatitude dayside total electron content enhancements", *Journal of Geophysical Research: Space Physics*, **117**(A2), 2012.

Ssessanga N., Mckinnell L.A. and Habarulema J.B., "Estimation of foF2 from GPS TEC over the South African region", *Journal of Atmospheric and Solar-Terrestrial Physics*, **112**, pp. 20–30, 2014.

Stamper R., Belehaki A., Buresová D., Cander L.R., Kutiev I., Pietrella M., Stanislawska I., Stankov S., Tsagouri I., Tulunay Y.K. and Zolesi B., "Nowcasting, forecasting and warning for ionospheric propagation: tools and methods", *Annals of Geophysics*, 2004.

Stankov S., Jakowski N., Wehrenpfenning A. and Warnant R., "Index of local response to geomagnetic activity for use in the short-term ionospheric forecast", *Proceedings of the COST271 2002 workshop*, 2002.

Sugiura M., "Hourly values of equatorial Dst for the IGY", *Annals of the International Geophysical Year*, **35**, 1963.

Sugiura M. and Kamei T., "Equatorial Dst index 1957–1986, IAGA Bull., 40", *by A. Berthelier and M. Menville (Int. Serv. Geomagn. Indices Publ. Off., Saint Maur, 1991)*, 1991.

Tapping K., "The 10.7 cm solar radio flux (F10. 7)", *Space Weather*, **11**(7), pp. 394–406, 2013.

Tariku Y.A., "Validation of the IRI 2016, IRI-Plas 2017 and NeQuick 2 models over the West Pacific regions using the SSN and F10. 7 solar indices as proxy", *Journal of Atmospheric and Solar-Terrestrial Physics*, 2019.

Tassev Y., Velinov P.I., Tomova D. and Mateev L., "Analysis of extreme solar activity in early September 2017: G4–Severe geomagnetic storm (07–08.09) and GLE72 (10.09) in solar minimum", *Compt. rend. Acad. bulg. Sci*, **70**(10), pp. 1437–1444, 2017.

Tooley M. and Wyatt D., *Aircraft Communications and Navigation Systems*, Routledge, 2017.

Tsagouri I., Belehaki A., Moraitis G. and Mavromichalaki H., "Positive and negative ionospheric disturbances at middle latitudes during geomagnetic storms", *Geophysical Research Letters*, **27**(21), pp. 3579–3582, 2000.

Tshisaphungo M., Habarulema J.B. and McKinnell L.A., "Modeling ionospheric foF2 response during geomagnetic storms using neural network and linear regression techniques", *Advances in Space Research*, **61**(12), pp. 2891–2903, doi:10.1016/j.asr.2018.03.025, 2018.

Tsurutani B., Judge D., Guarnieri F., Gangopadhyay P., Jones A., Nuttall J., Zambon G., Didkovsky L., Mannucci A., Iijima B., Meier R., Immel T., Woods T., Prasad S., Floyd L., Huba J., Solomon S. and Straus P., "The October 28, 2003 extreme EUV solar flare and resultant extreme ionospheric effects: Comparison to other Halloween events and the Bastille Day event", *Geophysical Research Letters*, **32**(3), 2005.

Tsurutani B., Mannucci A., Iijima B., Abdu M.A., Sobral J.H.A., Gonzalez W., Guarnieri F., Tsuda T., Saito A., Yumoto K., Fejer B., Fuller-Rowell T.J., Kozyra J., Foster J.C., Coster A. and Vasyliunas V.M., "Global dayside ionospheric uplift and enhancement associated with interplanetary electric fields", *Journal of Geophysical Research: Space Physics*, **109**(A8), 2004.

Tsurutani B., Mannucci A., Iijima B., Guarnieri F., Gonzalez W., Judge D., Gangopadhyay P. and Pap J., "The extreme Halloween 2003 solar flares (and Bastille Day, 2000 Flare), ICMEs, and resultant extreme ionospheric effects: A review", *Advances in Space Research*, **37**(8), pp. 1583–1588, 2006.

Tsurutani B., Verkhoglyadova O., Mannucci A., Saito A., Araki T., Yumoto K., Tsuda T., Abdu M., Sobral J., Gonzalez W.D. *et al.*, "Prompt penetration electric fields (PPEFs) and their ionospheric effects during the great magnetic storm of 30–31 October 2003", *Journal of Geophysical Research: Space Physics*, **113**(A5), 2008a.

Tsurutani B.T., Echer E., Guarnieri F.L. and Kozyra J., "CAWSES November 7–8, 2004, superstorm: Complex solar and interplanetary features in the post-solar maximum phase", *Geophysical Research Letters*, **35**(6), 2008b.

Tsurutani B.T., Gonzalez W.D., Gonzalez A.L., Tang F., Arballo J.K. and Okada M., "Interplanetary origin of geomagnetic activity in the declining phase of the solar cycle", *Journal of Geophysical Research: Space Physics*, **100**(A11), pp. 21717–21733, 1995.

Turner J., "The Development of Ionospheric Index T", *Prepared by Ionospheric Predictions Service (IPS) Division, Australia*, (June), 1968.

Usoskin I.G., "A history of solar activity over millennia", *Living Reviews in Solar Physics*, **14**(3), 2017.

Uwamahoro J.C., Giday N.M., Habarulema J.B., Katamzi-Joseph Z.T. and Seemala G.K., "Reconstruction of storm-time total electron content using ionospheric tomography and artificial neural networks: A comparative study over the African region", *Radio Science*, **53**(11), pp. 1328–1345, 2018a.

Uwamahoro J.C. and Habarulema J.B., "Modelling total electron content during geomagnetic storm conditions using empirical orthogonal functions and neural networks", *Journal of Geophysical Research: Space Physics*, **120**(12), 2015.

Uwamahoro J.C., Habarulema J.B. and Okouma P.M., "Storm Time Total Electron Content Modeling Over African Low-Latitude and Midlatitude Regions", *Journal of Geophysical Research: Space Physics*, **123**(9), pp. 7889–7905, doi:10.1029/2018JA025455, 2018b.

Valladares C., Eccles J., Basu S., Schunk R., Sheehan R., Pradipta R. and Ruohoniemi J., "The magnetic storms of 3–4 August 2010 and 5–6 August 2011: 1. Ground-and space-based observations", *Journal of Geophysical Research: Space Physics*, **122**(3), pp. 3487–3499, doi: 10.1002/2016JA023359, 2017.

Verhulst T., Altadill D., Mielich J., Reinisch B., Galkin I., Mouzakis A., Belehaki A., Burešová D., Stankov S., Blanch E. *et al.*, "Vertical and oblique HF sounding with a network of synchronised ionosondes", *Advances in Space Research*, **60**(8), pp. 1644–1656, 2017.

Vijaya Lekshmi D., Balan N., Tulasi Ram S. and Liu J., "Statistics of geomagnetic storms and ionospheric storms at low and mid latitudes in two solar cycles", *Journal of Geophysical Research: Space Physics*, **116**(A11), 2011.

Wang R., Zhou C., Deng Z., Ni B. and Zhao Z., "Predicting f o F 2 in the China region using the neural networks improved by the genetic algorithm", *Journal of Atmospheric and Solar-Terrestrial Physics*, **92**, pp. 7–17, 2013.

Wanliss J.A. and Showalter K.M., "High-resolution global storm index: Dst versus SYM-H", *Journal of Geophysical Research: Space Physics*, **111**(A2), 2006.

White R.S., *Space physics*, Gordon and Breach, 1970.

Wu C.C., Liou K., Lepping R.P., Hutting L., Plunkett S., Howard R.A. and Socker D., "The first super geomagnetic storm of solar cycle 24:The St. Patricks day event (17 March 2015)", *Earth, Planets and Space*, **68**(1), p. 151, 2016.

Xystouris G., Sigala E. and Mavromichalaki H., "A complete catalogue of high-speed solar wind streams during solar cycle 23", *Solar Physics*, **289**(3), pp. 995–1012, 2014.

Yan X. and Su X., *Linear Regression Analysis: Theory and Computing*, World Scientific, 2009.

Yasyukevich Y., Astafyeva E., Padokhin A., Ivanova V., Syrovatskii S. and Podlesnyi A., "The 6 September 2017 X-class solar flares and their impacts on the ionosphere, GNSS, and HF radio wave propagation", *Space Weather*, **16**(8), pp. 1013–1027, 2018.

Yiğit E., Frey H.U., Moldwin M.B., Immel T.J. and Ridley A.J., "Hemispheric differences in the response of the upper atmosphere to the August 2011 geomagnetic storm: A simulation study", *Journal of Atmospheric and Solar-Terrestrial Physics*, **141**, pp. 13–26, 2016.

Yizengaw E., Moldwin M., Galvan D., Iijima B., Komjathy A. and Mannucci A., "Global plasmaspheric TEC and its relative contribution to GPS TEC", *Journal of Atmospheric and Solar-Terrestrial Physics*, **70**(11-12), pp. 1541–1548, 2008.

Yizengaw E., Moldwin M., Komjathy A. and Mannucci A., "Unusual topside ionospheric density response to the November 2003 superstorm", *Journal of Geophysical Research: Space Physics*, **111**(A2), 2006.

Yu H. and Wilamowski B.M., "Levenberg-marquardt training", *Industrial electronics handbook*, **5**(12), p. 1, 2011.

Yue X., Wan W., Liu L., Ning B. and Zhao B., "Applying artificial neural network to derive long-term foF2 trends in the Asia/Pacific sector from ionosonde observations", *Journal of Geophysical Research: Space Physics*, **111**(A10), 2006.

Zell A., Mache N., Huebner R., Mamier G., Vogt M., Schmalzl M. and Herrmann K.U., "SNNS (stuttgart neural network simulator)", *Neural network simulation environments*, pp. 165–186, Springer, 1994.

Zhang D.H., Xiao Z., Hao Y.Q., Ridley A. and Moldwin M., "Modeling ionospheric foF2 by using empirical orthogonal function analysis", *Annales Geophysicae*, **29**(8), p. 1501, 2011.

Zhang J., Richardson I., Webb D., Gopalswamy N., Huttunen E., Kasper J., Nitta N., Poomvises W., Thompson B., Wu C.C. and Yashiro S., "Solar and interplanetary sources of major geomagnetic storms (Dst ≤ -100 nT) during 1996–2005", *Journal of Geophysical Research: Space Physics*, **112**(A10), 2007.

Zolesi B., Belehaki A., Tsagouri I. and Cander L.R., "Real-time updating of the simplified ionospheric regional model for operational applications", *Radio Science*, **39**(2), 2004.

Zolesi B. and Cander L.R., *Ionospheric prediction and forecasting*, Springer, 2014.

Zolesi B., Cander L.R. and De Franceschi G., "Simplified ionospheric regional model for telecommunication applications", *Radio Science*, **28**(4), pp. 603–612, 1993.

Zolesi B., Cander L.R. and De Franceschi G., "On the potential applicability of the simplified ionospheric regional model to different midlatitude areas", *Radio Science*, **31**(3), pp. 547–552, 1996.